Transient Dynamics in Electromagnetically Induced Transparency

by

Jamal Mohammad Khani

A Thesis Submitted in Partial Fulfillment of the
Requirements for the Degree of

MASTER OF SCIENCE

in the Department of Physics and Astronomy

Transient Dynamics in Electromagnetically Induced Transparency

by

Jamal Mohammad Khani

Supervisory Committee

Dr. Andrew MacRae, Co-Supervisor
(Department of Physics)

Dr. Arthur Blackburn, Co-Supervisor
(Department of Physics)

ABSTRACT

Electromagnetically Induced Transparency (EIT) has proven to be an invaluable resource for numerous applications in quantum technology, specifically in quantum memories, quantum repeaters, and quantum sensors. EIT also has significant applications in fundamental physics and nonlinear optics. Given that EIT is a foundational component of future quantum technology, a comprehensive understanding of its parameters is essential for the development of future devices.

This thesis focuses on the transient dynamics of EIT, specifically examining oscillations in the absorption of the Probe Field (PF) as a means to determine the decoherence of the ground states. Transient EIT has been explored in previous theoretical and experimental studies across various systems, including Cold Atoms (CAs) and hot vapor media. Here, transient EIT is studied theoretically, numerically, and experimentally. Parameter exploration has been conducted to understand the effects of different parameters on the transient behavior of EIT and to identify which decoherence mechanisms have the most significant impact on the quality of EIT. Experimentally, we explored a hot atomic vapour of, naturally abundant Rubidium (Rb) atoms. Additionally, progress towards constructing a CAs system, using a Magneto-Optical Trap (MOT) from scratch was made, opening the door to future studies of this system.

Contents

List of Tables

List of Figures

LIST OF ACRONYMS

AC	Alternating Current
ACSS	AC-Stark Shift
AE	Atomic Ensemble
ALI	Atom-Light Interaction
AOM	Acousto-Optic Modulator
APD	Avalanche Photodiode
BO	Bakeout
BS	Beam Splitter
BW	Bandwidth
CA	Cold Atom
CF	Control Field
CO	Collapse Operators
CPT	Coherent Population Trapping
CPU	Central Processing Unit
CQED	Cavity Quantum Electrodynamics
DAVLL	Dichroic Atomic Vapour Laser Lock
DB	Doppler Broadening
DE	Differential Equation
DM	Density Matrix
EIT	Electromagnetically Induced Transparency
EMF	Electromagnetic Field
EOM	Electro-Optic Modulator
ES	Eigenstate
EV	Eigenvalue
EF	Electric Field
FWHM	Full-Width at Half-Maximum
FWM	Four-Wave Mixing
FB	Feedback
FF	Feedforward
FT	Feedthrough
FSR	Free Spectral Range
GSD	Ground-State Decoherence

GS	Ground State
GPU	Graphics Processing Unit
H	Hamiltonian
HF	Hyperfine
IR	Infrared
IPython	Interactive Python
LPF	Low-Pass Filter
MF	Magnetic Field
MBD	Maxwell-Boltzmann Distribution
MES	Master Equation Solver
MHFR	Mode-Hop Free Range
MOT	Magneto-Optical Trap
NumPy	Numerical Python
NRD	Nonradiative Decay
OD	Optical Depth
OP	Optical Power
OPLL	Optical Phase Locked Loop
op-amp	Operational Amplifier
PF	Probe Field
PID	Proportional-Integral-Derivative
PLA	Polylactic Acid
PBS	Polarizing Beam Splitter
QuTiP	Quantum Toolbox in Python
QKD	Quantum Key Distribution
QM	Quantum Memory
QO	Quantum Optics
QS	Quantum System
RBF	Rabi Frequency
Rb	Rubidium
RF	Radio Frequency
RWA	Rotating Wave Approximation
SciPy	Scientific Python
SNSPD	Superconducting Nanowire Single-Photon Detector
SP	Single-Photon
SS	Steady-State

SSS	Steady-State Solver
TPU	Tensor Processing Unit
UHV	Ultra-High Vacuum
VC	Vapor Cell
VS	Vacuum System
WP	Weak Probe
ZS	Zeeman Splitting
μ**M**	μ-Metal

LIST OF SYMBOLS

a_0	Bohr radius
B	Magnetic field strength
c	Speed of light
χ	Susceptibility
Δ	One-photon detuning
δ	Two-photon detuning
ΔE	Energy splitting
E	Electric field strength
e	Elementary charge
f	Absorption oscillator strength
F	Total angular momentum quantum number (coupling of J and I)
g_F	Landé g-factor for the total angular momentum
Γ	Decay Rate/Natural Line Width (FWHM)
γ	Ground-state decoherence rate
h	Planck's constant
$\hbar$	Reduced Planck's constant
$\hbar\omega_0$	Transition energy
I	Nuclear spin quantum number
J	Total angular momentum quantum number
k	Wave vector
k_B	Boltzmann's constant
Λ	Lambda system (three-level atomic configuration)
λ	Wavelength in vacuum
l	Orbital angular momentum quantum number, defines the shape of the orbital
m_e	Electron mass
m_F	Magnetic quantum number for the total angular momentum
m_l	Magnetic quantum number, describes the orientation of the orbital
m_s	Spin magnetic quantum number, orientation of the electron spin
μ_0	Permeability of vacuum
μ_B	Bohr magneton
n	Principal quantum number, defines the energy level of an electron

Ω_b	Probe Rabi frequency
Ω_c	Pump Rabi frequency
P	P shell (orbital with $l = 1$)
S	S shell (orbital with $l = 0$)
s	Spin quantum number, intrinsic angular momentum of an electron
σ^+	Left circular polarization
σ^-	Right circular polarization
T_D	Doppler temperature
u	Atomic mass unit
ω_0	Frequency of the transition
ρ_{ij}	Density matrix elements

ACKNOWLEDGEMENTS

Over the past two years of study, I have become more knowledgeable thanks to a great environment in Quantum BC and participation in various workshops, competitions, and seminars related to quantum computing, earning several awards along the way. This journey has fortified my mindset. I learned the only place success comes before work is in the dictionary. I have learned to be comfortable being uncomfortable, especially when your support system is not physically present. With my family 0.0697 ± 0.0001AU ($\sim 10^7$m) away, I faced the challenges of worrying about their safety amidst riots in my home country. Additionally, I dealt with the diagnosis and subsequent passing of my best friend from sickle cell disease and the loss of my grandmother, unable to attend their funerals or return to my country. The only way I could endure these hardships and continue to work effectively was through strict self-discipline. Despite being the sole graduate student in the lab, I maintained a routine of waking up almost every day at 5AM for a run, working out afterwards, working in the lab from 8AM to 10PM, then sleeping and repeating.

This wouldn't have been done without the lessons from my legends, Kobe Bryant and David Goggins. They taught me ***"if you want something badly enough, you will find a way; if not, there is always an excuse out there."***

I would like to thank my supervisor, Andrew. When I first came to the lab at UVic, I knew nothing about experimental work as my background was mainly theoretical. Despite this, Andrew taught me everything I know about experimental physics and quantum optics. Thanks for giving me a shot, Andrew. I hope I'm no longer a "liability" (I caused a lot of trouble when I decided to sleep in my office). I hope you're not filled with regret and despair for your decision!

I must also acknowledge that everything I know in the field of quantum computing, I learned while I was an NSERC CREATE Quantum BC scholar. Thanks to Lukas Chrostowski, and Jeff Young for teaching me quantum photonics. Thanks to Rogério de Sousa, Shabir Barzanjeh, Reza Molavi, Corey Rae McRae, Yves Bérubé-Lauzière, and Mathieu Juan for teaching me how superconducting quantum devices work. Thanks to Daniel Oblak for giving me the opportunity to work as an intern at Quantum Technology Inc. (QTi). I would also like to thank the many people at Quantum BC (UBC, UVic, and SFU) with whom I had fruitful discussions, and who helped solidify my knowledge (there are too many to list here). Additionally, I extend my gratitude to the researchers at the QCloud Lab at UofC.

DEDICATION

To those who spend countless hours in the lab,
doing nothing but science!

PAPER UNDER SUBMISSION

We are submitting the following paper to *Optics Express*:
Jamal Mohammad Khani, Andrew MacRae, Kenny Gregory, Connor Kupchak, and Eden Figueroa. "Transient Electromagnetically Induced Transparency in Realistic Settings."

Chapter 1

Introduction

The ability to control individual quantum degrees of freedom and their interactions facilitates quantum coherent computation. This capability enables the execution of specific computational tasks and quantum simulations that exceed the capabilities of modern supercomputers [1, 2]. Since the initial ideas [3] of leveraging quantum mechanical properties for computation, various promising platforms have emerged, including superconducting qubits [4, 5], photonic integrated circuits [6, 7], and atomic systems [8]. Among these platforms, photons play a pivotal role in the future of science and technology as information carriers in Measurement Device Independent Quantum Key Distribution (QKD) [9] and highly sensitive quantum metrology [10]. Photons are pristine and decoherence-free Quantum Systems (QSs), allowing single-qubit operations to be performed with extremely high fidelity [11]. However, this advantage comes with the challenge of achieving photon-photon interactions necessary for deterministic two-qubit gates. Nevertheless, by using photons, five out of the seven DiVincenzo criteria for constructing a quantum computer are satisfied [12].

An intriguing question often arises: what exactly is a Single-Photon (SP)? Is it just a particle, or is it a wave? To answer this question, countless arguments have been made, and heated debates have taken place throughout the past century in the history of science. It turns out that a photon is an elementary excitation of a normal mode of the Electromagnetic Field (EMF). Hence, a SP is the quantum state of a radiation mode that contains a single excitation.

The interactions between quantum particles of light and atoms are of significant interest [13]. One such interaction effect is Electromagnetically Induced Transparency (EIT) [14]. To tackle the challenge of manipulating information carried by light using other light, nonlinear interactions are crucial. EIT has been proposed to achieve giant

optical nonlinearities [15]. Recent applications of EIT include field-deployable quantum memories for quantum networking [16] and EIT-based quantum sensing that operates at or beyond the standard quantum limit [17]. Furthermore, EIT facilitates the ultra-slow propagation of light pulses with minimal loss [18], which has potential applications as a tunable delay line for logic operation gates on photonic chips, as seen in micro-strip resonators [19]. As EIT becomes a vital component of quantum technology, it is crucial to investigate parameters that significantly impact its performance, such as transparency depth and full-width at half-maximum (FWHM). Among these, the decoherence of the Ground State (GS) holds particular importance, as previous theoretical works [20] have linked the transient effect of EIT to GS Decoherence (GSD), with some experimental studies [21, 22, 23] observing this phenomenon. Achieving high-throughput in EIT applications, such as optical Quantum Memory (QM), magnetometry, and optical signal processing, requires an in-depth understanding of transient behavior. While transient EIT has been extensively studied for three-level atomic systems [20], laboratory setups involving Rb atoms are far more complex, featuring over 16 levels and typically experiencing Doppler Broadening (DB). This necessitates a comprehensive exploration of EIT behavior under realistic laboratory conditions.

Significant Contributions of this Work

To address these needs, we conducted extensive numerical simulations of an EIT system, examining the impact of DB, deviations from an ideal Lambda system (such as multiple excited states), ground-state dephasing, and population exchange on transient EIT response. This provides new information on practical implementation as no work has explored transient EIT included all of these mechanisms to date. We also set up an experiment to measure transient EIT and obtained preliminary data, aiming to bridge theoretical predictions with observed laboratory effects. To enhance control over atomic states, we constructed a MOT, enabling more refined studies in a cold Atomic Ensemble (AE).

A significant portion of this research involved physically building the experimental setup from scratch, including the design and construction of necessary electronics, fabrication of mechanical elements, and establishing an Ultra-High Vacuum (UHV) environment. Additionally, we employed Wolfram Mathematica to theoretically investigate a method for quantifying the GSD in an AE through the absorption or

transmission behavior of the PF, offering new insights into EIT's potential for advanced quantum technologies.

Chapter 2 presents the theoretical background necessary for the rest of the thesis. The formalism of EIT is introduced, followed by a description linking the transient effect of EIT to the decoherence of the GS. The atomic system used for EIT is described, with an emphasis on the relevant features of its interaction with external EMFs. A brief theory for understanding atom trapping using a MOT is also provided.

In Chapter 3, simulations of EIT and its transient effects are presented. The influence of various parameters on the manifestation of transient oscillations is displayed, discussed, and related to the experimental situation. Furthermore, we theoretically investigate a method for quantifying the GSD in an AE through the ab- sorption or transmission behavior of the PF.

Chapter 4 delves into the technical aspects of the experimental work, detailing the techniques used to manipulate light in the desired manner to observe and measure the effects, facilitating comparison with the simulations.

The experimental results of the thesis are presented in Chapter 5. The observation of overdamped transient oscillations of EIT in hot Rb vapor is reported, and the effects of different experimental parameters on this transient effect are discussed.

Finally, Chapter 6 discusses the construction of a MOT from scratch for conducting the transient EIT experiment.

Chapter 2

Theoretical background

In this chapter, I briefly describe the background theory necessary for the rest of the thesis. For a more in-depth review and full description of EIT, refer to [24, 25, 14]. To derive the Atom-Light Interaction (ALI) for the EIT effect here, a semiclassical approach is employed, where the field is treated classically while the atoms are treated as quantum objects. For a fully quantum derivation of EIT, refer to [26].

EIT, as its name suggests, is a phenomenon where the ALI induces a transparency window in an ensemble of atoms. More specifically, transparency is induced for a specific frequency due to quantum interference between excitation pathways. In EIT, the atomic medium's optical response is modified by coherence induced via an applied light field. Various atomic structures can exhibit EIT, namely Lambda (Λ), Ladder, and V. In the following sections, we primarily focus on the Λ scheme, as shown in Figure 2.1.

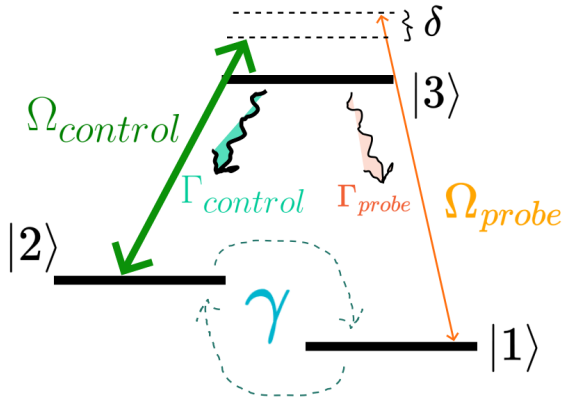

Figure 2.1: EIT in the Λ-scheme. The transitions $|2\rangle \rightarrow |3\rangle$ and $|1\rangle \rightarrow |3\rangle$ are allowed, whereas $|1\rangle \longleftrightarrow |2\rangle$ is dipole forbidden.

2.1 Dark state in the Λ scheme

A three-level Λ atomic system consists of three Eigenstates (ESs) $|1\rangle$, $|2\rangle$, and $|3\rangle$, with corresponding Eigenvalue (EV) energies $E_n = \hbar\omega_n$ (for $n = 1, 2, 3$). States $|1\rangle$ and $|2\rangle$ are the ground and metastable states, respectively, and $|3\rangle$ is the excited state, as shown in Figure 2.1. These states form a complete basis set. Any state of the atom $|\psi\rangle$ can be written as a superposition of these bare states. For a three-level atom, this can be expressed as

$$|\psi\rangle = c_1|1\rangle + c_2|2\rangle + c_3|3\rangle \tag{2.1}$$

where the coefficients c_i represent the probability amplitude of being in state $|i\rangle$.

The atomic Hamiltonian (H) in the basis of bare states can be written as

$$H_0 = \begin{pmatrix} \hbar\omega_1 & 0 & 0 \\ 0 & \hbar\omega_2 & 0 \\ 0 & 0 & \hbar\omega_3 \end{pmatrix}. \tag{2.2}$$

The EVs of this H give the energies of the three levels. In the presence of an EMF, the total H of the system is composed of two parts:

$$H(t) = H_0 + H_I(t) \tag{2.3}$$

where $H_I(t)$ is the interaction H and accounts for the coupling of levels by the laser field with frequency ω. The interaction H takes the form $-\mathbf{d}.\mathbf{E}$, where the electric dipole operator is $\mathbf{d} = -e\mathbf{D}$ and $\mathbf{E}$ is the Electric Field (EF). Since the EMF is treated classically, it can be modeled as a simple oscillating field $\mathbf{E} = E_0\hat{\mathbf{e}}\cos(kr - \omega t)$, where the polarization vector is denoted as $\hat{\mathbf{e}}$ with amplitude E_0. Given that the applied wavelength considered here (around 795 nm) is much larger than the scale of the atomic wavefunction, the spatial dependence of the field can be neglected under the dipole approximation, meaning the field is treated as uniform across the extent of the atom.

The interaction of the field with the atom occurs via the dipole operator:

$$\hat{\mathbf{D}} = \sum_{i,j} \mathbf{D}_{ij}|i\rangle\langle j|. \tag{2.4}$$

The bare state atomic H is denoted by $|i\rangle$ and $|j\rangle$. The matrix element $\mathbf{D}_{ij} = \langle i|D|j\rangle$ is defined in [27]. In the interaction H, it is assumed that the optical field couples the atomic levels, and the strength of the coupling is defined by the Rabi frequency (RBF), which is proportional to the intensity of E_0 and the polarization through $\hat{\mathbf{e}}$:

$$\Omega_{ij} = \frac{eE_0}{\hbar}\langle i|\mathbf{D}.\hat{\mathbf{e}}|j\rangle. \tag{2.5}$$

With the RBF defined, the interaction H can be written as

$$H_I(t) = -\frac{\hbar}{2}[\Omega_1 e^{-i\omega_1 t}|3\rangle\langle 1| + \Omega_2 e^{-i\omega_2 t}|3\rangle\langle 2|] + h.c. \tag{2.6}$$

The minus sign in $e^{-i\omega_i t}$ represents the absorption of a photon in the transition from the lower state to the excited state $|1\rangle \rightarrow |3\rangle$, while the plus sign corresponds to the lowering operation.

In the Rotating Wave Approximation (RWA), and without considering decoherence and spontaneous emissions, the total H in the co-rotating frame can be written as

$$H(t) = -\frac{\hbar}{2}\begin{pmatrix} 0 & 0 & \Omega_{31}^* \\ 0 & 2\delta & \Omega_{32}^* \\ \Omega_{31} & \Omega_{32} & 2\Delta \end{pmatrix} \tag{2.7}$$

where δ is the two-photon detuning $\Delta_2 - \Delta_1$, and Δ_i is the detuning from state $|i\rangle$. For the special case where the two lasers are on resonance, one of the ESs of the H is of interest, known as the dark state:

$$|\text{Dark}\rangle = \frac{\Omega_2|1\rangle - \Omega_1|2\rangle}{\Omega_n} \tag{2.8}$$

where $\Omega_n = \sqrt{|\Omega_1^2| + |\Omega_2^2|}$. Here, Ω_2 is the field strength of the pump, and Ω_1 is the field strength of the PF.

The reason this state is called a dark state is intuitive: there is no excited state component, as it is a coherent superposition of the GSs. An atom prepared in this state can remain in it indefinitely and exhibit no absorption (i.e., it does not interact with the incident light field), assuming that the decoherence of the GS is negligible. We will address decoherence effects more rigorously in the next section.

If a strong Control Field (CF) $\Omega_2 \gg \Omega_1$ is used, the majority of the atomic population will reside in state $|2\rangle$, and the PF Ω_1 will not experience absorption,

rendering the atomic medium transparent to that optical frequency. This phenomenon occurs due to quantum destructive interference of the excitation pathways.

In the previous equation, we considered the case where the two-photon detuning δ is zero. If we assume a small, non-zero δ, the dark state under the weak optical field assumption evolves in time as

$$|\text{Dark}(t)\rangle = \frac{\Omega_2|1\rangle - e^{i\delta t}\Omega_1|2\rangle}{\Omega_n} \tag{2.9}$$

where the phase of state $|2\rangle$ evolves slowly. If the two-photon detuning is small, the accumulated phase is negligible, but as the detuning increases, the effect of phase evolution becomes more pronounced. Since various decoherence effects impact the atoms, the dark state has a finite lifetime.

In the next section, we will study different decoherence effects in detail.

2.2 Dynamics of EIT

Here, the decoherence processes for optical transitions and the atomic coherence associated with the dark state are considered. These need to be more accurately described to properly model EIT in the laboratory and experimental physics. To solve for the coherent dynamics of the dark state (or any state vector in general), one can solve the Schrödinger equation:

$$i\hbar\frac{\partial}{\partial t}|Dark\rangle = H|Dark\rangle \tag{2.10}$$

where the solutions are oscillatory, describing the population oscillation between atomic states, known as Rabi oscillation. However, considering the state vector alone is not sufficient when dealing with real atomic systems due to incoherent processes, primarily decay between levels.

To account for these effects, the density operator is defined as:

$$\hat{\rho} = |Dark\rangle\langle Dark|. \tag{2.11}$$

In matrix form, it can be written as:

$$\hat{\rho} = \begin{pmatrix} |c_1|^2 & c_1 c_2^* & c_1 c_3^* \\ c_2 c_1^* & |c_2|^2 & c_2 c_3^* \\ c_3 c_1^* & c_3 c_2^* & |c_3|^2 \end{pmatrix}. \tag{2.12}$$

The population of the bare states $|1\rangle$, $|2\rangle$, and $|3\rangle$ can be found from the diagonal elements of the Density Matrix (DM), while the off-diagonal elements describe the coherence between states. By adopting the DM formalism, we can extract more information from the AE compared to using only the state vector. For instance, mixed states, which are statistical mixtures of quantum states, can be described using the DM, something not possible with a single state vector. One way to distinguish a mixed state from a pure state (a linear superposition of bare states) is by taking the trace of the square of the DM ($\mathrm{Tr}[\rho^2]$). If the trace equals 1, the state is pure; otherwise, it is a mixed state.

Analogous to the time-dependent Schrödinger equation for the state vector, the coherent time evolution of the DM can be solved using the Liouville-von Neumann equation:

$$\dot{\hat{\rho}} = -\frac{i}{\hbar}[\hat{H}, \hat{\rho}]. \tag{2.13}$$

In order to account for dissipative effects, the Maxwell-Bloch equation should be considered [28]:

$$\dot{\hat{\rho}} = -\frac{i}{\hbar}[\hat{H}, \hat{\rho}] + \hat{\mathcal{L}}(\hat{\rho}). \tag{2.14}$$

As described before, the coherent evolution of the atomic system under the driving field is captured by the first term of Eq. 2.14, while the second term, which contains the Lindblad superoperator $\hat{\mathcal{L}}$, encompasses all the decoherence effects, namely, decay and dephasing in the system. More specifically, the dissipative processes (or the decoherence effects) can be split into two parts:

$$\hat{\mathcal{L}} = \hat{\mathcal{L}}_{\mathrm{dephasing}} + \hat{\mathcal{L}}_{\mathrm{decay}}, \tag{2.15}$$

where the first part describes dephasing due to the finite linewidth of the driving fields, and the second part describes spontaneous decay within the atom. Throughout this thesis, we ignore the effects of decoherence due to dephasing and consider only spontaneous decay. However, one could include dephasing effects in the density

operator as:

$$\hat{\mathcal{L}}_{\text{dephasing}} = -(\gamma_{i,i+1} + \ldots + \gamma_{j-1,j})\rho_{ij}, \tag{2.16}$$

where $\gamma_{n,n+1}$ represents the linewidth of the field coupling the nth and $(n+1)$th levels. The dephasing operator accounts for the fact that a true single-frequency source does not exist but has a finite linewidth, which only affects the off-diagonal elements of the DM (coherences). Throughout this thesis, we assume that the atomic system is closed, meaning that the atomic population remains within the atomic level system and is not lost to an external reservoir. For our Λ scheme, the decay operator can be written as:

$$\hat{\mathcal{L}}_{decay} = \begin{pmatrix} \Gamma_1\rho_{11} & -\frac{\gamma}{2}\rho_{12} & -\frac{\Gamma_1}{2}\rho_{13} \\ -\frac{\gamma}{2}\rho_{21} & \Gamma_2\rho_{22} & -\frac{\Gamma_2}{2}\rho_{23} \\ -\frac{\Gamma_1}{2}\rho_{31} & -\frac{\Gamma_2}{2}\rho_{32} & -(\Gamma_1\rho_{11} + \Gamma_2\rho_{22}) \end{pmatrix} \tag{2.17}$$

where the GSD is denoted as γ, and it is assumed that there is no decay from the lowest level. The off-diagonal elements of the decay operator describe the changes in the population of the states, and are always negative since decay causes a loss of coherence. The effect of decay on Rabi oscillations results in damping, meaning the system eventually reaches a Steady-State (SS) or equilibrium. The timescale for the system to settle into equilibrium is short when a Continuous Wave laser is used, compared to the measurement timescale.

Using equations 2.7 and 2.17, we can solve equation 2.14 and write the off-diagonal elements of the optical Bloch equation as:

$$\begin{aligned} \dot{\rho}_{31} &= \frac{i}{2}[\Omega_{31}^*\rho_{11} - \Omega_{31}^*\rho_{33} + \Omega_{32}^*\rho_{21} + 2\Delta\rho_{31}] - \frac{\Gamma_1}{2}\rho_{31} \\ \dot{\rho}_{21} &= \frac{i}{2}[\Omega_{32}\rho_{31} - \Omega_{31}^*\rho_{23} + 2\delta\rho_{12}] - \frac{\gamma}{2}\rho_{21} \\ \dot{\rho}_{32} &= \frac{i}{2}[\Omega_{31}^*\rho_{12} + \Omega_{32}^*\rho_{22} - \Omega_{32}^*\rho_{33} + 2\Delta\rho_{32} - 2\delta\rho_{32}] - \frac{\Gamma_2}{2}\rho_{32}. \end{aligned} \tag{2.18}$$

One of the measurable quantities from the DM is the electric susceptibility, $\chi(\Delta)$, which represents the response of the medium to an applied field and encapsulates both the absorptive and dispersive properties of the medium. In the SS solution, where $\partial\hat{\rho}/\partial t = 0$, the expression for susceptibility is given as:

$$\chi(\Delta) = \frac{nD_{ij}^2}{\epsilon_0\hbar\Omega_{ji}}\rho_{ij}, \tag{2.19}$$

where n is the number density, which can also be used to compute the optical thickness or optical depth (OD). For numerical solutions, after solving the master equation, one can extract the probe coherence and, by taking the imaginary part and multiplying it by the necessary prefactors, determine the susceptibility. For an analytical solution, after defining the initial conditions, one must solve the coupled Differential Equations (DEs) in 2.18, which leads to the following form (see Appendix A for more details):

$$\chi(\Delta) = \frac{nD_{ij}^2}{\epsilon_0 \hbar} \frac{i\gamma/2 + \delta}{1/2|\Omega_{32}|^2 + 2(i\Delta - \Gamma/2)(i\delta - \gamma/2)}. \tag{2.20}$$

Looking at the denominator of the above equation, we see that the susceptibility depends on the optical power (OP) P_{op} and beam width ω_0, through the square modulus of the Rabi angular frequency, $\Omega = \frac{D}{\hbar\omega_0}\sqrt{\frac{2P_{op}}{\varepsilon c \pi}}$. The magnitude of $\chi(\Delta)$ depends on the strength of the particular transition. Thus, the simulation results could be off by a few factors of magnitude if realistic transition strengths are not considered. When calculating the OD for simulation purposes [29], one must consider the dipole strength for each transition, which can be obtained from [30]. Additionally, it is important to account for the isotope abundance ratio of Rb atoms. In equation 2.19, ρ_{ij} describes the coherence between the ith and jth levels.

The relationship between susceptibility and the DM is based on the atomic polarization equation:

$$\mathbf{P} = n\mathrm{Tr}(\rho\hat{\mathbf{D}}) = n\rho_{ij}D^* e^{-i\omega t} + \text{c.c.} \tag{2.21}$$

Treating the polarization of a dilute gas as a linear dielectric and based on the fact that $\mathbf{E} \cdot D = \hbar\Omega_b$, one can write:

$$\mathbf{P} = \epsilon_0\chi(\Delta)\mathbf{E} = \epsilon_0\chi(\Delta)\frac{\hbar\Omega_p}{D} + \text{c.c.} \tag{2.22}$$

Equating equations 2.21 and 2.22 reveals that $\chi(\Delta)$ is a complex quantity. The real part of $\chi(\Delta)$ is proportional to the dispersion (phase shift and propagation velocity) of the medium, while the imaginary part is proportional to the absorption/gain coefficient α. These real and imaginary parts are interconnected, and one can derive one from the other using Kramers-Kronig relations [31, 32]. This relation demonstrates the evidence of causality and the fact that absorption at one frequency is accompanied by a phase shift at other frequencies [33].

In this thesis, the primary interest lies in the absorption of the probe laser after

passing through the Vapor Cell (VC). The probe absorption is proportional to the off-diagonal element of the DM (or the probe coherence), $\alpha \propto -\mathrm{Im}[\rho_{31}]$, with a constant of proportionality $k_b N D^2/(\hbar\epsilon_0)$, where $k_b = 2\pi/\lambda_b$ is the wave-number of the PF.

According to Beer-Lambert law, the transmission of a monochromatic beam through an atomic medium of length L is defined as:

$$T = \frac{I(l)}{I_0} = e^{-\alpha(T,\omega,\hat{\epsilon})l}, \tag{2.23}$$

where $I(l)$ is the intensity of light after passing through the cell, and I_0 is the intensity of light before entering the cell. In equation 2.23, $\alpha(T, \omega, \hat{\epsilon})$ accounts for the macroscopic absorption coefficient of the medium, which depends on the frequency of the beam, the temperature of the cell, and the polarization of the beam. This coefficient can be derived from the microscopic atomic absorption cross-section and the number density n [34] as:

$$\alpha(T, \omega, \hat{\epsilon}) = n(T)\sigma_{\mathrm{cross}}(\omega, \hat{\epsilon}), \tag{2.24}$$

where $\sigma_{\mathrm{cross}}(\omega, \hat{\epsilon})$ is the on-resonance scattering cross-section, and can be calculated as:

$$\sigma_{\mathrm{cross}}(\omega, \hat{\epsilon}) = \frac{\hbar\omega\Gamma/(2I_{\mathrm{sat}}(\hat{\epsilon}))}{1 + 4(\Delta/\Gamma)^2 + (I_0/I_{\mathrm{sat}}(\hat{\epsilon}))}, \tag{2.25}$$

where $I_{\mathrm{sat}}(\hat{\epsilon})$ is the saturation intensity, which can be expressed as:

$$I_{\mathrm{sat}}(\hat{\epsilon}) = \frac{c\epsilon_0\Gamma^2\hbar^2}{4|\hat{\epsilon}\cdot d|^2}. \tag{2.26}$$

Substituting equation 2.26 into equation 2.25, we obtain an expression that allows the calculation of the ratio of intensity to the saturation intensity.

Figure 2.2 shows the $\mathrm{Re}[\chi(\Delta)]$ and $\mathrm{Im}[\chi(\Delta)]$, corresponding to the dispersion and absorption/gain profiles of the three-level Λ AE. It is worth noting that the FWHM of the EIT signal is controllable via the strength of the CF [35], which has applications in manipulating the EIT bandwidth (BW) in QM. However, when the RBF of the CF (essentially high OP) is significantly higher than the decay rate, Autler-Townes splitting centered at the two-photon detuning occurs, which is not ideal. Another important figure of merit is the EIT depth, which decreases in the presence of decoherence, reducing the transparency dip. A common approach to remedy this is to use a stronger CF to compensate for dephasing effects, though this

leads to power broadening.

It can be shown that the power-broadened EIT linewidth can be written as [24]:

$$\mathrm{FWHM}_{\mathrm{EIT}} = \gamma + \frac{|\Omega_c|^2}{\Gamma_2}, \tag{2.27}$$

where γ represents the GSD, and Ω_c is the RBF of the CF. The limiting factor of the EIT linewidth is the decoherence of the GS [24]. From equation 2.27, it can be seen that one way to measure the GSD is to gradually decrease the pump power ($\Omega_c \to 0$) and extrapolate to find γ.

$$\frac{I_0}{I_{sat}(\hat{\epsilon})} = 2\left(\frac{\Omega}{\Gamma}\right)^2. \tag{2.28}$$

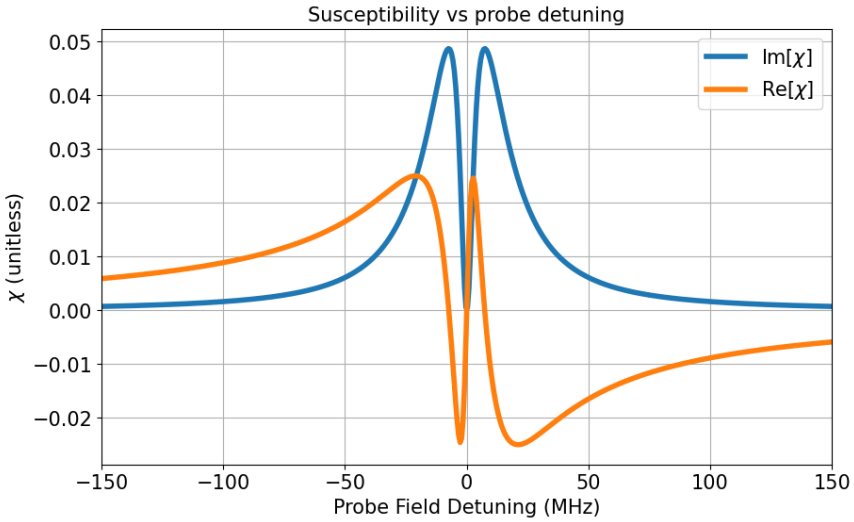

Figure 2.2: Susceptibility of Λ-type atomic system.

Although the separation in the Hyperfine (HF) levels of the GS is on the order of gigahertz, one can neglect the interaction of the fields with the other HF levels. However, this is not the case for the HF excited states, where the atomic level separation is on the order of a few hundred megahertz, and the Doppler effect dominates, causing transitions to become unresolved. Therefore, for more accurate modeling, it is advisable to include the extra HF manifolds in the calculations.

2.3 EIT in atomic vapor

So far, EIT has been considered in stationary atoms, but in reality, atoms are moving and possess kinetic energy due to the temperature of the medium. This non-stationary situation leads to spectral broadening in the frequency domain or decoherence in the time domain. The movement of atoms introduces various effects such as DB, collisional broadening, and time-of-flight broadening. The Rb-Rb collisional self-broadening coefficient for the ^{87}Rb D_1 line is on the order of 10^{-7} Hz cm^3 [36], implying that for self-broadening to be comparable to the natural linewidth, the temperature must be approximately 120°C.

At the temperatures used in our experiment, DB has a more significant effect on the system, and therefore, we study it in more detail. Here, we consider DB due to the velocity of atoms within the ensemble along the axis of the optical beam (transverse atomic motion is neglected for DB, but we account for it in beam-transit effects). Atoms moving toward or away from the direction of laser propagation experience red and blue detuning, respectively. This means that atoms perceive different frequencies of light depending on their direction of motion.

Thus, the system's H must be modified so that the effective detuning accounts for this movement:

$$\Delta = \Delta_i \pm \vec{k_i} \cdot \vec{v_j}, \tag{2.29}$$

where $\vec{k_i}$ is the wavevector of the optical light (probe or pump), and $\vec{v_j}$ is the atomic velocity. Optical fields may co-propagate or counter-propagate relative to each other, leading to different signs for the vector. In our setup, Rb atoms move according to the Maxwell-Boltzmann velocity distribution in the VC at room temperature ($\sim$ 300K). The Doppler-broadened lines have linewidths of several hundred MHz, which is larger than the excited state HF splitting. This means that even if we detune the probe light by several hundred MHz from the resonance frequency for an atom at rest, there are still atoms within the VC moving at the right velocity relative to the light wavevector such that they see the light as being exactly on resonance in their center-of-mass frame. These atoms absorb light from the incident beam, thereby attenuating the light beam as it passes through the VC.

The relative propagation direction of the beams also affects the absorption. Counter-propagating beams are one technique we used to obtain saturation absorption spectroscopy. For the EIT experiment, however, we assume that the fields are co-propagating. Since the atoms are distributed across different velocity sub-classes

based on their temperature, the probability distribution of the moving atoms can be calculated using the Maxwell-Boltzmann Distribution (MBD), which is a Gaussian distribution centered at zero:

$$\mathrm{MBD}(v_j) = \frac{1}{\sqrt{2\pi}\sigma} e^{-v_j^2/(2\sigma^2)}. \tag{2.30}$$

The standard deviation σ for the MBD is given by $\sigma = \sqrt{\frac{k_B T}{m}}$, where k_B is the Boltzmann constant, T is the temperature of the VC in Kelvin, and m is the mass of an atom, which in our case is ^{87}Rb. In our experiment, the VC is heated to 80°C, so it is helpful to build an intuition for the velocity distribution of atoms at this temperature. Figure 2.3 shows the MBD for ^{87}Rb at 80°C.

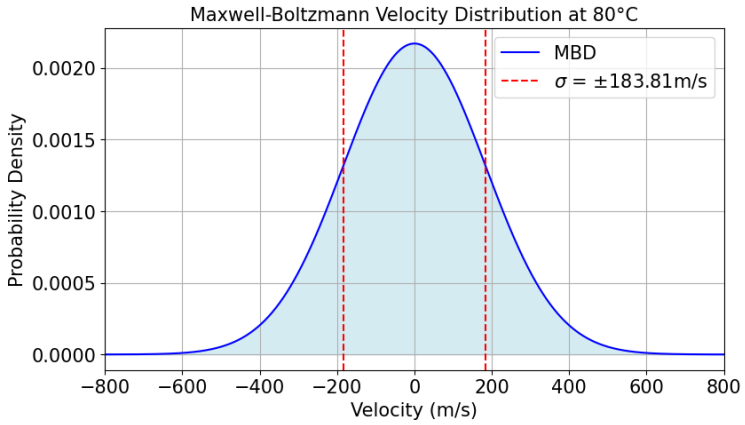

Figure 2.3: MBD for ^{87}Rb AE at 80°C with $\sigma = \pm 183.81$ m/s.

As seen in the figure, the standard deviation is ±183.81 m/s, which is important when simulating EIT in a Doppler-broadened medium. Understanding the velocity sub-class where the majority of atoms reside helps balance the trade-off between simulation accuracy and run time. To illustrate the Doppler effect in the EIT spectrum, we can plot the effect of different velocity shifts that the AE can experience, as shown in Figure 2.4.

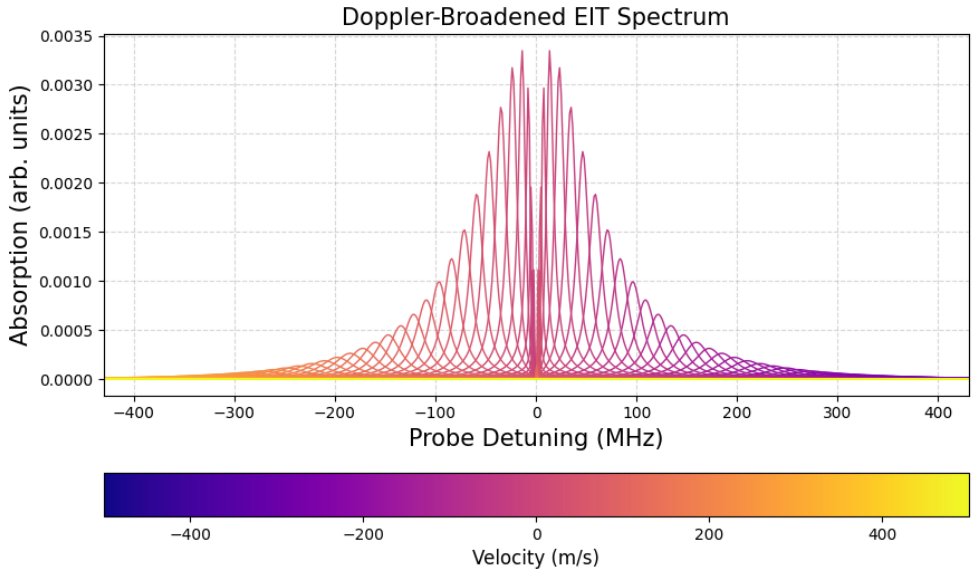

Figure 2.4: Doppler effect on EIT spectrum.

The Doppler shift results in inhomogeneous spectral broadening when averaging over the different velocities in the ensemble. The lineshape of a Doppler-broadened atomic system follows a Voigt profile, which is a convolution of Gaussian and Lorentzian profiles. Atomic motion influences the shape of the EIT lineshape through both one-photon and two-photon processes. The one-photon effect, which involves spectral broadening and decoherence of the $|3\rangle - |1\rangle$ transition (related to the optical coherence ρ_{31}), always occurs in vapor media. While it does not directly impact the EIT linewidth, it reduces the absorption cross-section of the medium, leading to a decreased OD.

The two-photon effect concerns the overall transition from state $|3\rangle$ to state $|2\rangle$ (associated with the spin coherence ρ_{32}). This process broadens the EIT linewidth and diminishes the contrast of the EIT susceptibility (both real and imaginary components) [37]. With this, Eq. 2.19 can be modified as:

$$\bar{\chi}(\Delta') = \int_{-\infty}^{\infty}\int_{-\infty}^{\infty} \chi(\Delta_p - k_p v_p, \Delta_c - k_c v_c) f(v_p) f(v_c)\, dv_p\, dv_c,$$

where $f(v_p)$ and $f(v_c)$ are the MBD functions for the velocities along the probe and coupling beams, respectively. The FWHM of the homogeneous broadening is Γ, and the $1/e$ half-width of the inhomogeneous broadening is σ. In a Doppler-broadened system, atoms with different velocities experience varying one-photon detunings, but

there exists a narrow frequency region where none of the atomic velocity groups absorb light.

It turns out that the EIT linewidth in a thermal ensemble can be written as [24]:

$$\mathrm{FWHM}_{\mathrm{EIT}} = \gamma + \frac{|\Omega_c|^2}{\Gamma_2 + W_d} \tag{2.31}$$

where W_d is the one-photon Doppler width. Regarding the EIT linewidth in the presence of atomic motion in a thermal VC, the movement can be either ballistic or diffusive. In the latter case, atomic motion occurs in the presence of inert buffer gas, where frequent collisions between optically active atoms (Rb atoms) and buffer gas atoms effectively suppress ballistic motion, leading to a substantial reduction in broadening and decoherence.

If the duration of the ALI is relatively short (on the order of nanoseconds), atoms do not move significantly compared to the beam size, and the time-of-flight effect can be neglected. On the other hand, if the experiment uses continuous light, this effect must be considered for accurate modeling (though some papers neglect it). The time-of-flight effect accounts for the transverse motion of atoms, which contributes to broadening, and can be calculated as:

$$\tau = \sqrt{3}\sigma\omega_0 \tag{2.32}$$

When considering the decoherence of the GS, $1/\tau$ should be subtracted from the experimentally measured decoherence [38]. In real scenarios, multiple atomic levels are involved. For sufficiently high light intensity, atomic population can be transferred to multiple excited states, which then decay into other states not involved in the Λ-scheme. This process is called optical pumping [39]. Consequently, if a strong beam is used in the experiment, all atomic levels in the system must be considered to model or simulate the effects accurately. On the other hand, if the experiment is conducted in the weak regime, modeling the interaction by considering only the atomic levels in the Λ-type configuration would yield a close agreement with the experiments.

2.4 Physical properties of Rb-87

The physical system we work with experimentally is a dilute gas of naturally abundant atomic Rb, though we couple the optical light to ^{87}Rb in our Λ scheme.

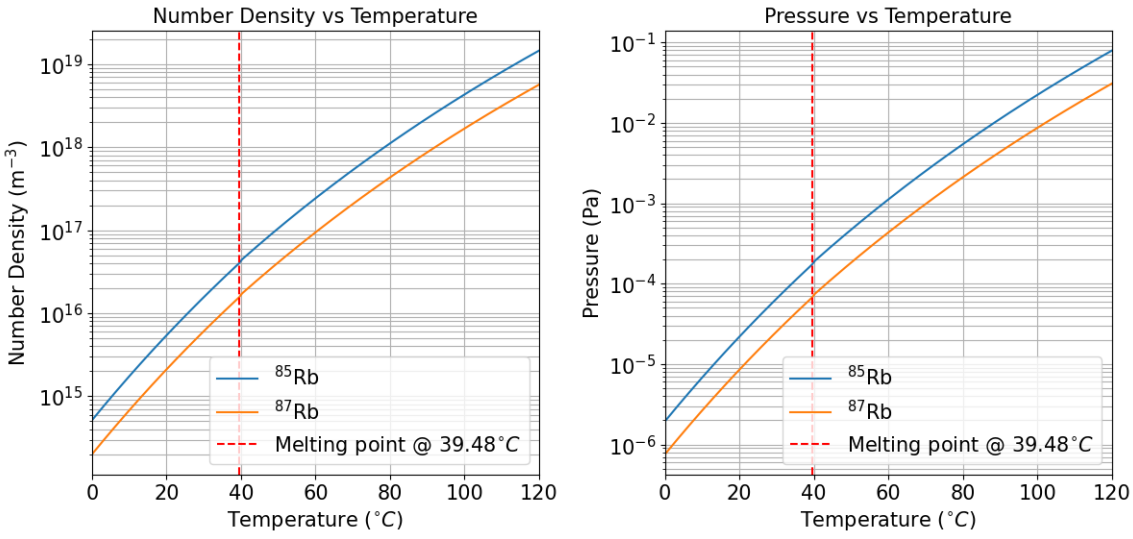

(a) (b)

Figure 2.5: Number density vs. temperature and pressure vs. temperature in a thermal VC for both ^{85}Rb and ^{87}Rb.

Natural Rb comprises 72% of ^{85}Rb, the stable isotope, and the remaining is ^{87}Rb, which is slightly radioactive. When examining the spectrum manifold while scanning the laser, it is easy to distinguish these isotopes by looking at the absorption profile since the isotope with a higher presence in the VC absorbs more light. Controlling the OD of the AE inside the VC is crucial in our experiment. Referring to equation 2.23, one way to control this parameter is by altering the number density of atoms. According to the ideal gas law, $PV = nRT$, the number density n can be controlled by increasing the pressure or temperature in the system. Using the Clausius-Clapeyron relation, which describes the temperature dependence of vapor pressure, the vapor pressure of Rb atoms can be modeled as follows [40, 30]:

$$\begin{aligned} \log_{10} P_v &= 7.738 - \frac{4215}{T} \text{ (solid phase)} \\ \log_{10} P_v &= 7.193 - \frac{4040}{T} \text{ (liquid phase),} \end{aligned} \tag{2.33}$$

where P_v is the vapor pressure in Torr, and T is in Kelvin. The relationship between number density and pressure/temperature for a naturally abundant Rb VC is shown in Fig. 2.5. In older versions of the Steck data, the number densities of ^{85}Rb and ^{87}Rb differed because they were modeled with different equations. However, in the new version, both isotopes are modeled using the same equation and have the same number

density. In Figure 2.5, I plot the number densities of ^{85}Rb and ^{87}Rb in a VC with natural isotopic abundance, taking into account the ratio of the species present in the cell. Rb is one of the alkali metals, characterized by a single valence electron orbiting a filled shell, which makes it relatively easy to work with due to its hydrogen-like atomic structure [41]. Atomic transitions in Rb occur in the near-infrared (near-IR) region, which is advantageous because many off-the-shelf diode lasers are available in this wavelength range. There are two popular transitions in Rb atoms, known as the D_1 and D_2 lines. In this work, we use the D_1 transition line due to the better results obtained with this transition compared to the D_2 line. Specifically, a laser tuned to this transition couples the $5^2S_{1/2}$ state to the $5^2P_{1/2}$ state.

External EMFs can further split the atomic levels, a phenomenon known as Zeeman Splitting (ZS) and AC-Stark Shift (ACSS). These energy shifts (splittings) can occur with time-varying or static EMFs. In the following, we will explore the atomic structure and energy splitting in more detail.

2.4.1 Energy levels and atomic structure

The schematic for the D_1 and D_2 lines of ^{87}Rb can be seen in figure 2.6.

The transition used in this work for ^{87}Rb, $5^2S_{1/2} \rightarrow 5^2P_{1/2}$, is part of a fine-structure doublet that also exhibits additional HF structure. All atoms possessing a single valence electron (i.e., in the outermost shell) exhibit this type of doublet structure in their energy levels. The spacing between the two components of the fine-structure doublet is small, with a 6 THz separation between the D_1 and D_2 lines of ^{87}Rb. This splitting is referred to as the "fine-structure," caused by the coupling of the quantum numbers **L** (orbital angular momentum) and **S** (spin angular momentum) [42]. Quantum number **L** describes the orbital angular momentum, while **S** represents the spin angular momentum of the atomic levels. The sum of these two quantum numbers, known as the total electron angular momentum, is conserved under the **L.S** coupling H. The number of lines in the fine structure is determined by the EVs of the total electron angular momentum:

$$|L - S| \leqslant J \leqslant |L + S|. \tag{2.34}$$

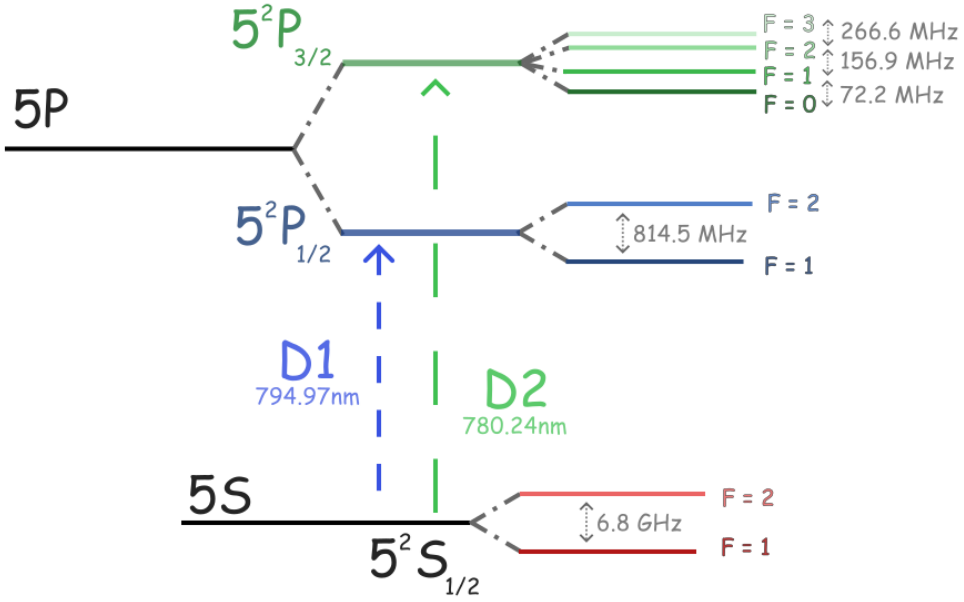

Figure 2.6: Energy levels for ^{87}Rb.

The magnitude of **J** is given by $\sqrt{J(J+1)}\hbar$. For the GS (S-shell), $L = 0$, and the spin angular momentum is $S = 1/2$, resulting in only one possible value for **J**, $J = 1/2$. For the first excited state (P-shell), $L = 1$ and $S = 1/2$, yielding $J = 1/2$ or $J = 3/2$. Based on the value of J, the transition from the S-shell to the P-shell ($L = 0 \rightarrow L = 1$), referred to as the D-line transition, is split into a fine structure doublet: the D_1 ($5^2S_{1/2} \rightarrow 5^2P_{1/2}$) line and the D_2 ($5^2S_{1/2} \rightarrow 5^2P_{3/2}$) line.

The coupling of total electron angular momentum (**J**) with nuclear angular momentum (**I**) results in another splitting, known as the HF structure, which is much smaller in spacing compared to the fine structure. The sum of these quantum numbers gives the total atomic angular momentum **F**, where $\mathbf{F} = \mathbf{J} + \mathbf{I}$. The magnitude of **F** is similarly constrained by:

$$|J - I| \leqslant F \leqslant |J + I|. \tag{2.35}$$

According to the value of **F**, energy levels can shift. In the GS of ^{87}Rb, $J = 1/2$ and $I = 5/2$, so **F** can take two possible values (2 or 3). For the excited state in the P-shell, $5^2P_{1/2}$, which corresponds to the D_1 line, **F** can also be either 2 or 3. However, for the D_2 line, the possible values for **F** are doubled. This difference in the number of possible states may be one reason why the EIT feature is observed with greater depth and narrower linewidth in the D_1 transition compared to the D_2

transition.

It has been theoretically studied that a significant reduction in EIT transmission occurs when there are four closely spaced excited states [43], which aligns with experimental observations in alkali atoms [44, 45, 46, 47]. The reduction in transparency for EIT is attributed to the presence of closely spaced excited states, resulting in a shift of the two-photon resonance due to an imbalance in the dipole moments of the transitions coupled by the CF. This effect is eliminated in systems where the dipole moments are balanced [48]. The energy shifts in the HF structure are also worth noting, as the pump and PFs used in this thesis are tuned to be 6.834 GHz apart, which corresponds to the HF structure energy splitting. Using first-order perturbation theory with the hydrogenic H and neglecting quadrupole and octupole moments, the energy splitting can be described by [49]

$$\Delta_{hf} = -\frac{\mu_{5^2} L_i}{2}[I(I+1) + J(J+1) - F(F+1)] \tag{2.36}$$

where $\mu_{5^2} L_i$ is the magnetic dipole constant for state $|i\rangle$. Plugging in the values for each allowable $\mathbf{F}$, this energy splitting formula reveals that for the S-shell of the D_1 line, the separation is 6.834682610904290(90) GHz.

2.4.2 Interaction with external fields

The interaction of external fields has a significant impact on the quality of EIT, particularly in modifying the atomic structure. These fields can be magnetic, electric, or a combination of both, and they can either be static or time-dependent. For our case, we are primarily interested in the effects of a static Magnetic Field (MF), which causes additional splitting in energy levels, known as ZS.

Zeeman Splitting

An external static MF can break the degeneracy of the quantum number $\mathbf{F}$ into energy sub-levels, creating 2F+1 sub-levels. The H describing the interaction with this external MF is

$$H_B = \frac{\mu_B \mathbf{B}}{2}(g_s \mathbf{S} + g_L \mathbf{L} + g_I \mathbf{I}), \tag{2.37}$$

where μ_B is the Bohr magneton, and g_s, g_L, and g_I are the g-factors corresponding to the spin, orbital, and nuclear angular momenta, respectively. Compared to fine-structure splitting, the energy shift due to the MF is relatively small, making $\mathbf{J}$ (the

total electron angular momentum) a good quantum number. The interaction H, with the MF quantized along the z-axis, is given by

$$H_B = \frac{\mu_B B_z}{\hbar}(g_J J_z + g_I I_z), \tag{2.38}$$

where g_J is the Landé g-factor.

To calculate the energy splitting, the total H is the sum of the HF and Zeeman Hs. By diagonalizing this sum, we can find the EVs corresponding to the energy levels. Neglecting the nuclear spin offset, the H can be written as

$$H_{hfB} = \mu_{5^2} L_i \mathbf{I} \cdot \mathbf{J} + \frac{\mu_B B}{\hbar} g_J J_z, \tag{2.39}$$

where the first term describes the HF splitting and the second term accounts for the ZS. In the first term, the product of the total nuclear angular momentum ($\mathbf{I}$) and total electron angular momentum ($\mathbf{J}$) is a tensor product. The second term should also be treated as a tensor, meaning that J_z can be perceived as $\mathbf{I} \otimes J_z$, where $\mathbf{I}$ is a 4D identity matrix in the basis of $\mathbf{I}$ and J_z. In the basis of J_z, m_J, I_z, and m_I, and using Pauli spin matrices for J and their spin 3/2 analog for I, the EVs of H_{hfB} can be obtained as

$$\begin{aligned} E_{1,2} &= \frac{3\alpha}{4} \pm \frac{\beta}{2}, \\ E_{3,4} &= -\frac{1}{4}(\alpha \pm \sqrt{4(2\alpha)^2 + \beta^2}), \\ E_{5,6} &= -\frac{1}{4}(\alpha \pm \sqrt{4(2\alpha)^2 - 2\beta\alpha + \beta^2}), \\ E_{7,8} &= E_{5,6}, \end{aligned} \tag{2.40}$$

where $\alpha = \mu_{5^2} L_i \hbar$ and $\beta = \mu_B g_J$.

For large MFs where $\alpha/\beta \ll B$, the energy EVs can be approximated as

$$E_{sB} \sim \frac{\mu_B B}{2}(m_J g_J), \tag{2.41}$$

where the HF lines split into two separate lines corresponding to $m_J = \pm 1/2$.

On the other hand, for weak MFs, $B \ll \alpha/\beta$, the two HF lines split into eight lines, and the shift is linear in B. The EVs for this regime are

$$E_{\text{weak}} = \begin{cases} E_{F=1} - \mu_B g_F m_F B & \text{for } F = 1, m_F \in \{-1, 0, 1\}, \\ E_{F=2} + \mu_B g_F m_F B & \text{for } F = 2, m_F \in \{-2, -1, 0, 1, 2\}, \end{cases} \tag{2.42}$$

where $E_{F=2} = \frac{3\alpha}{4}$ and $E_{F=1} = -\frac{5\alpha}{4}$. This same result can also be derived using first-order perturbation theory [30].

AC-Stark Shift

Analogous to the effect of a MF, an EF can split spectral lines when it interacts with the atomic structure. The Stark shift can be static or time-dependent. In this work, we are primarily concerned with the Alternating Current (AC) or time-dependent EF. The explanation of the ACSS is more straightforward in the context of a two-level system (though such a system doesn't exist in reality, it can often be approximated under specific experimental conditions [50]).

Considering the time-independent coupled atom-light H, we have:

$$H = \frac{\hbar}{2} \begin{pmatrix} 0 & \Omega \\ \Omega & -2\Delta \end{pmatrix}. \tag{2.43}$$

The EVs of this H are:

$$E_{\pm} = -\frac{\hbar}{2}(\Delta \pm \sqrt{\Delta^2 + \Omega^2}). \tag{2.44}$$

In the absence of the EF (i.e., $\Omega = 0$), the ESs of the H are simply the bare states of the system (i.e., $|1\rangle$ and $|2\rangle$) with eigenenergies of $\hbar\omega$ and 0, assuming the lower state has zero energy. However, when light interacts with the atomic levels, the bare states are no longer ESs. For a near-resonant field, the ESs become dressed states, which are linear superpositions of the bare states.

$$|\pm\rangle = \frac{1}{\sqrt{2}}(|1\rangle \pm |2\rangle) \tag{2.45}$$

In this equation, the states $|\pm\rangle$ are the dressed states, which are linear superpositions of the bare states $|1\rangle$ and $|2\rangle$. As the RBF Ω increases, the energy levels of these dressed states shift further apart. This effect is known as the ACSS (or light shift). The ACSS is essential for achieving giant Kerr nonlinearities, which are crucial for applications such as two-qubit Control-Phase gates in EIT systems [51].

Chapter 3

Simulation of EIT and Transient EIT

In this chapter, we first outline the basic assumptions made for the simulation and then present the results of simulating EIT and its transient dynamics in a Λ-scheme using the Quantum Toolbox in Python (QuTiP) [52]. This package allows us to simulate the susceptibility by solving the SS DM and obtaining the expectation values of the dipole transitions. Additionally, for studying the transient effects—specifically the behavior when the CF is abruptly turned off—we employ the Master Equation Solver (MES), which provides time-dependent solutions for the system's H.

To ensure the validity of our simulations, we compare the results obtained from both the SS Solver (SSS) and the MES. This comparison serves as a consistency check, confirming that our observations are in agreement across methods. It is important to note that in the SS solution, the initial condition of the atomic state does not affect the final outcome. However, in the time-dependent MES, the initial state plays a crucial role, particularly when the CF is first turned on. Therefore, special attention must be given to ensure that the solutions are physically meaningful and consistent.

In general, the master equation must be solved to accurately model transient EIT. While the DM approach provides SS solutions, it averages out key dynamic information that we may be interested in—such as transient effects and spontaneous emission events. In particular, the DM does not reveal quantum jumps, as it focuses on SS behavior rather than capturing the full time evolution of the system.

3.1 Open Quantum System

In Quantum Optics (QO), the investigation of QSs often involves situations where the system is coupled to an external reservoir, making it an open system, as opposed to a closed system that can be described solely by the state vector $|\psi\rangle$. In most open QSs, it is difficult, if not impossible, to derive an analytical expression that describes the dynamics of the system. In such cases, we rely on numerical techniques, and QuTiP is one of the toolboxes that provides numerical methods to gain intuition about the system.

In the case of ALIs, absorption and emission of light couple the atom to the environment, meaning that the energy of the system is no longer conserved. When a system interacts with external field modes, information is lost to the environment [53]. However, we are mainly interested in the state the atom ends up in, not the specifics of which mode the atom interacts with. [Although studying those detailed dynamics is an entire field in itself, tackled beautifully by cavity quantum electrodynamics (CQED)!] To describe the probabilistic outcomes of the ensemble, we use the DM formalism, which represents the different probabilities (P_i) for various states of the system:

$$\hat{\rho} = \sum_i P_i |\psi_i\rangle\langle\psi_i|. \tag{3.1}$$

As a recap of what we covered in the previous chapter, the diagonal elements of the DM provide the population of the states, whereas the off-diagonal elements give information about the coherence between states. Using equation 3.1 allows us to describe systems in mixed states and to treat open systems with dissipation, as shown in equation 2.14. Since we are primarily interested in the dynamics of the system and not what happens to the reservoir after interaction, we can take the partial trace over the reservoir from the total DM to remove the reservoir's information:

$$\hat{\rho}(t) = \mathrm{Tr}_{\mathrm{R}}(\rho_T(t)). \tag{3.2}$$

With this reduced DM, we can then apply equation 2.13.

For the following simulations, we solve equation 2.14, but it is important to note the assumptions made in its derivation. Generally speaking, every atomic system contains a few degrees of freedom, which in the Λ-scheme are the 3 atomic levels. The reservoir contains all of the field modes surrounding the atom. Consequently, the effect of the system on the reservoir is negligible, while the reservoir has a huge

impact on the system [52]. This is known as the Markov approximation, where the reservoir has a short memory and the relaxation time of the reservoir is very short compared to the system $\tau_{env} \ll \tau_{sys}$. With this assumption, the dissipative process becomes irreversible, and there is no way to restore the information that leaks out into the reservoir. Another consequence is that the past memory does not affect the system's evolution.

Another approximation is the separation of the system and the reservoir at $t = 0$. Furthermore, we can extend this approximation by saying that if the interaction is weak and the reservoir is much larger than the system, the system and reservoir remain separable throughout the evolution:

$$\rho_T(0) \approx \rho(0) \otimes \rho_{env}(0). \tag{3.3}$$

Lastly, for solving the master equation, QuTiP neglects all fast rotating terms in the interaction picture.

3.2 Numerical results

We start by defining the H of the Λ system using equation 2.7. For the 4-level and 6-level systems, we use the method derived in B to write down the H for systems with more than 3 levels. Furthermore, we consider decoherence effects based on equation 2.17 and add them to the master equation or SSS in QuTiP. Taking the expectation value of the off-diagonal elements of the DM gives us the coherence of the state, which, by multiplying with the other constant parameters, allows us to calculate χ as in equation 2.19. By scanning the detuning of the PF and considering zero detuning for the CF, we plot the dispersion and absorption of the medium versus the PF detuning normalized to the natural linewidth in Fig. 2.2 for CAs. The calculation of the decay rate Γ for a transition from $J \longrightarrow J'$, using [30], is given by

$$\Gamma = \frac{e^2\omega_0^2}{2\pi\epsilon_0 m_e c^3}\frac{2J+1}{2J'+1}f, \tag{3.4}$$

where e is the electron charge, ω_0 is the transition frequency, m_e is the electron mass, and f is the absorption oscillator strength. Calculating for ^{87}Rb D1 transition where $J = 1/2$ to $J' = 1/2$, gives $\Gamma_b \approx \Gamma_c = 5.75 \times 2\pi$MHz [30]. The other parameters for some of the simulations are considered to be $\Omega_b = 1.63\ \Gamma_c$, $10^{-4}\Gamma_c$ and $\Omega_c = 2.82\ \Gamma_c$,

Γ_c. We specify which value we used for the simulation in the caption of each plot. Since we used both the MES and the SSS, we compared the results as a sanity check. It is worth noting that the MES is using a Scientific Python (SciPy) package called "scipy zvode adams" as the solving method for the numerical integration on the ordinary DEs that define the system. For more information on the solver, you can refer to F.4.

The MES takes the H and Collapse Operators (CO) to evolve over time. If the CO are not provided, the QS evolves with the unitary evolution of the H. The output of the MES is either a statevector at an arbitrary time in the time list fed to the solver or the expectation values of the fed operators. For our purposes, we are interested in the statevector of the system after the CF is turned on/off and the system evolves for a few microseconds to capture all of the oscillations until the system settles. Note that for the MES, one has to evolve the atomic system for a long time to ensure that it converges. It can be seen that both results are consistent in Fig. 3.1.

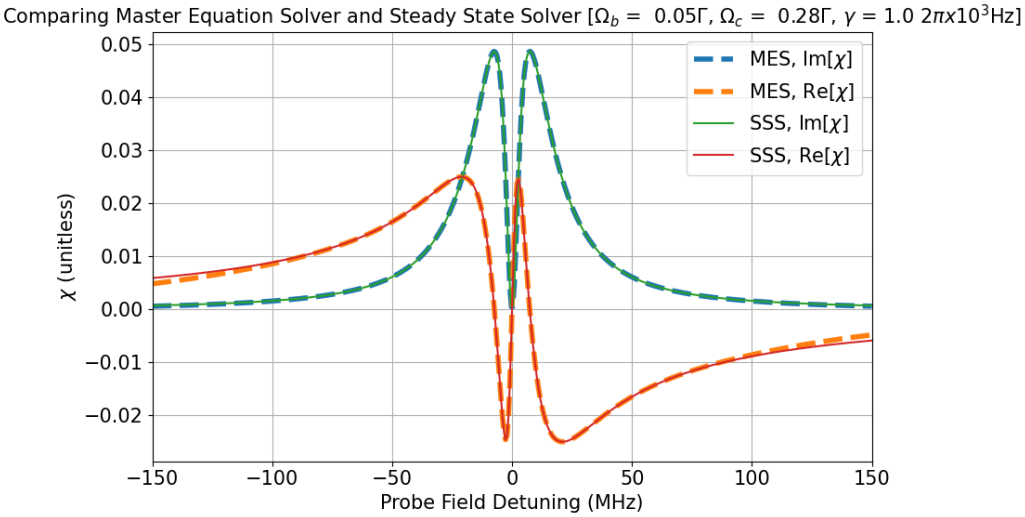

Figure 3.1: Comparing the answers of MES and SSS in QuTiP to make sure both converge.

In order to make sure that our numerical results are in agreement with the analytical expressions that we derived, we compared them in the Weak Probe (WP) field regime. It can be seen in figure 3.2 that they overlap significantly. A little bit of discrepancy is expected since, in deriving the analytical expression, we made a few assumptions to simplify the calculations.

In a hot VC, as opposed to CAs, one must consider the integral effect of the

velocity distribution of atoms moving in the AE. When considering DB effects, one should average over all the one-photon detunings that exist in the atomic system due to the velocity distribution given by the MBD.

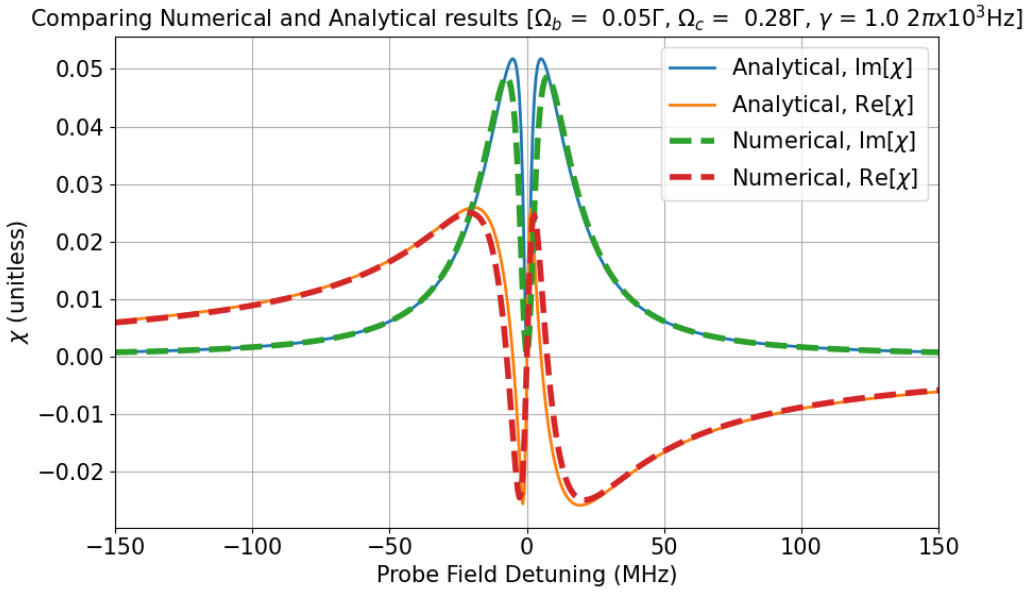

Figure 3.2: Numerical and analytical solution comparison.

Figure 3.3 shows the difference between Doppler-broadened and non-Doppler absorption profiles.

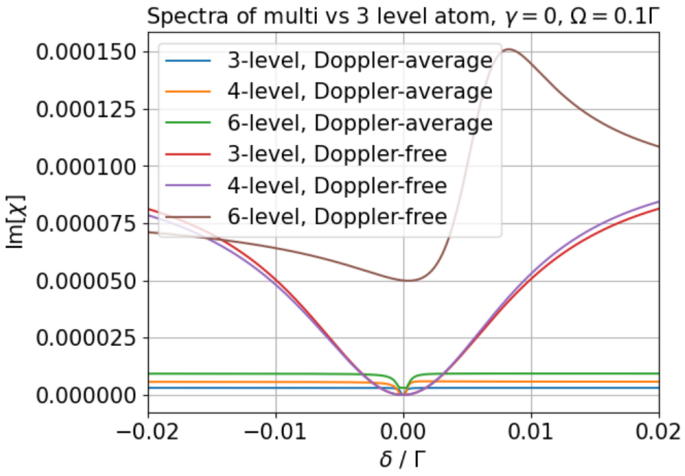

Figure 3.3: Comparison of absorption profiles of EIT with and without DB for different atomic levels.

To further confirm that the numerical solution is consistent with what we know

analytically, we compared the results of both methods. It is known that in analytical simulations we assume the PF is weak. Therefore, the numerical solution is more accurate when that assumption is not satisfied.

As seen in Fig. 3.2, there is a slight discrepancy between the two solutions, which arises from the assumptions made in the analytical equation.

Figures 3.4 and 3.5 show the spectra of non-Doppler and Doppler-averaged EIT for three different atomic systems, respectively.

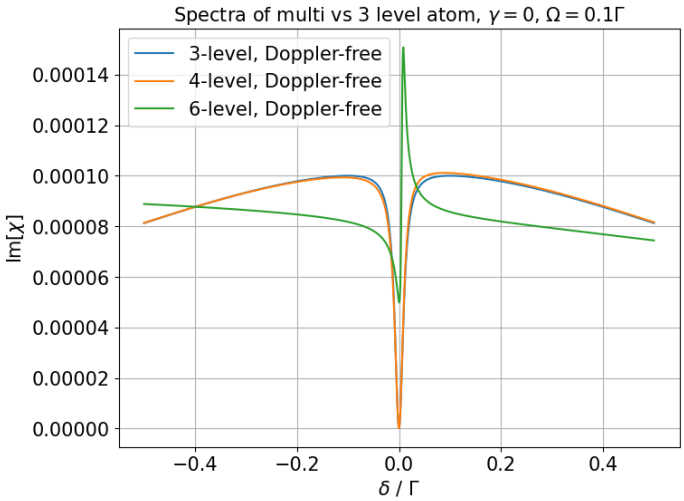

Figure 3.4: Spectra of EIT in the CA for different atomic levels.

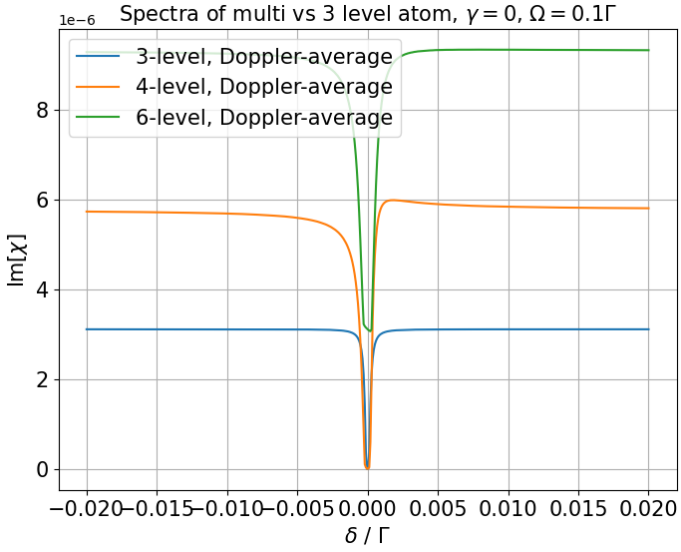

Figure 3.5: Spectra of EIT in the hot AE for different atomic levels.

The reason why the Doppler profile appears much more absorbed is due to the OD, which depends on the number density and hence the temperature of the cell.

In Fig. 3.6, the absorption profile of 3-level EIT shows the Voigt profile shape, which is expected.

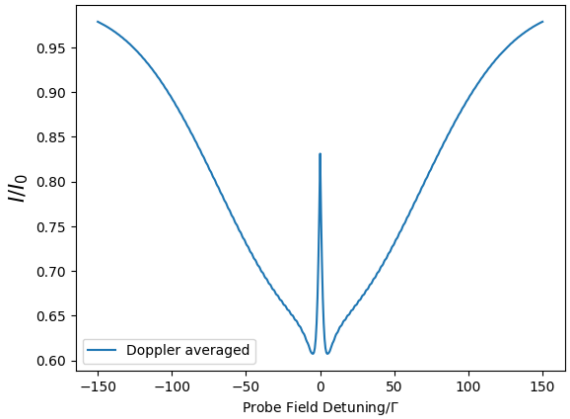

Figure 3.6: EIT profile at 80°C with DB.

Generally, in numerical simulations, it is recommended to have ways to sanity-check the results to ensure there are no numerical errors. To achieve this, we simulated the scenario where there is only one-photon detuning (pump is turned off by multiplying it by zero). In this case, we expect to see a Gaussian absorption profile without any transparency, as shown in Fig. 3.7.

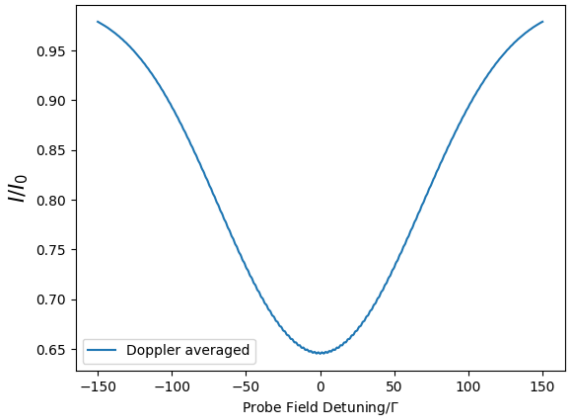

Figure 3.7: One-photon detuning absorption profile at 80°C.

The EIT linewidth is dependent on the GSD, as indicated in Eq. 2.27. To illustrate this, we simulated a Doppler-broadened medium where the value of γ is varied. Figure

3.8 shows the effect of GSD on the EIT spectra in a 3-level system. It is evident that a narrower FWHM can be achieved by lowering the value of γ. This is crucial for applications such as quantum sensing, where a narrower EIT feature provides greater precision in measuring changes in the parameter of interest, often a MF.

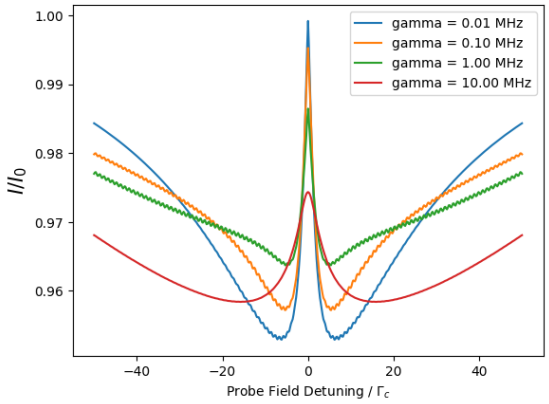

Figure 3.8: Effect of different decoherence values γ on EIT. This shows that the FWHM of the EIT is limited by the value of γ.

3.2.1 Transient EIT

To observe the transient dynamics of the EIT, we first let the simulation run for a while to reach analytical stability. Then, we turn on the CF while the probe is always on, and after a while, we turn the pump off again once the dark state is established in the system. The goal is to quantify the time it takes for EIT to establish and to observe the transient oscillations. Furthermore, we aim to relate the decay rate of the transient oscillations to the value of the GSD. In Fig. 3.9, two transient oscillations of EIT are observed: one occurring right after turning on the CF, which is highly dependent on the initial condition of the atomic system, and the second when the system reaches the SS and we turn off the CF non-adiabatically. For the initial condition, we consider that atoms are in a superposition of the GSs of the Λ scheme, $|\psi(0)\rangle = (|1\rangle + |2\rangle)/\sqrt{2}$.

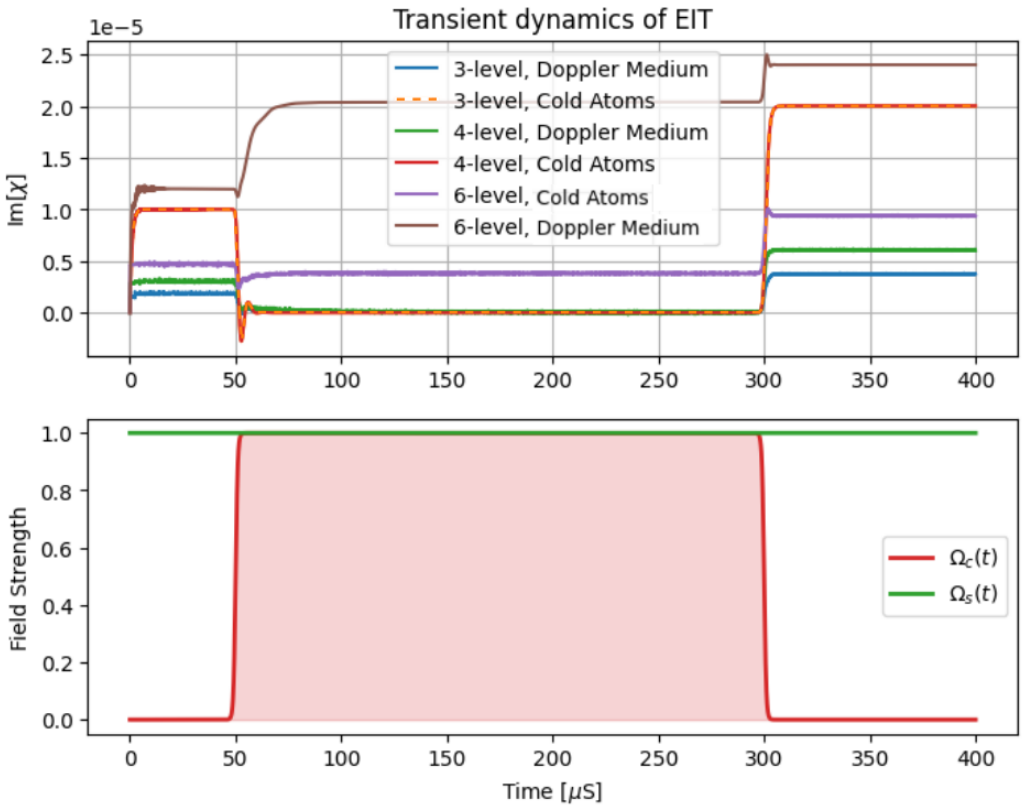

Figure 3.9: Transient dynamics of EIT with a sigmoid function for turning the CF on and off. The graph shows the overlap of a 4-level system in cold atom conditions and a 3-level system in cold atom conditions.

Looking at Fig. 3.9 reveals that there is a transient gain upon turning on the CF for an ideal cold atomic three-level Λ system. It also suggests that it takes 10μs for EIT to establish after the initial oscillations. Moreover, it should be noted that there is no transient gain when we consider the Doppler effect, which explains why such behavior is not observed in hot atomic vapor. In a sense, DB would wash out the oscillations and gain to the point that we just see the smooth damped oscillation of the PF. Furthermore, Fig. 3.9 explains why EIT in the D_2 line has a lower quality than in the D_1 line, since the transient EIT tends to settle into more absorption compared to the 3-level or 4-level system. It also reveals that the transient dynamics of turning on the CF continue long after it is turned on for the D_1 transition (lasting up to 30μs, until it fully settles). Figures 3.10 and 3.11 show close-up views of the turning-on and turning-off processes of the pump for ease of inspection.

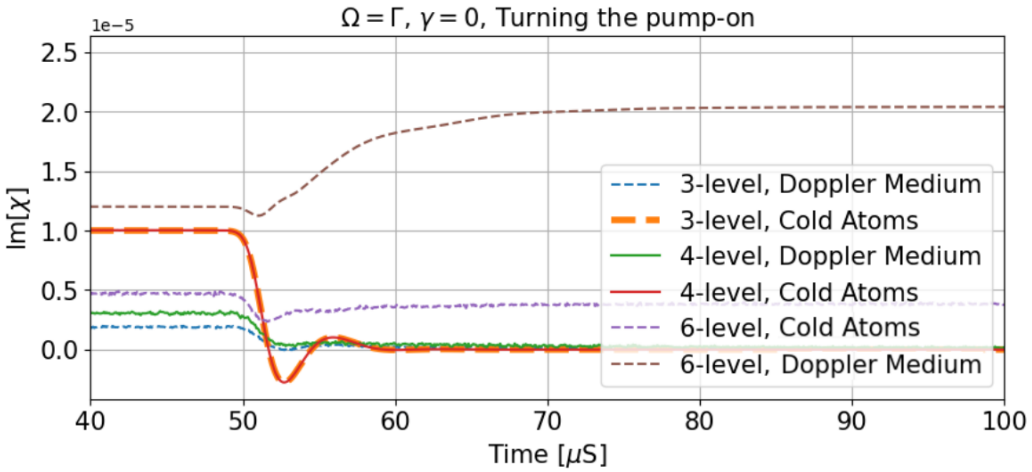

Figure 3.10: Close-up of Transient dynamics of EIT when turning on the CF.

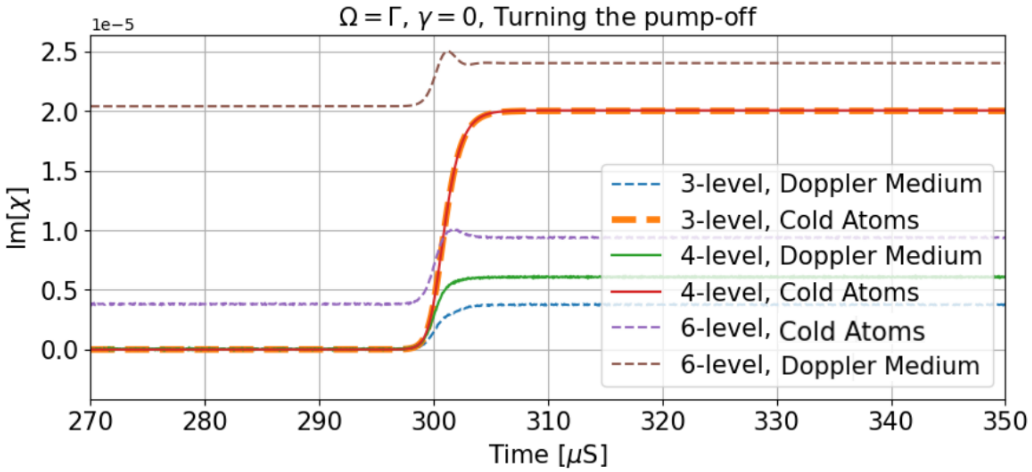

Figure 3.11: Close-up of Transient dynamics of EIT when turning off the CF.

Since, in the real world, there is no abrupt change in the optical field, there is always a response time for the system or device [in our case, the Acousto-Optic Modulator (AOM)] that we are working with, and we have to take that time into account. Otherwise, the simulation result is not realistic. To account for this, we consider a Sigmoid function for turning off the CF, with a slope that represents the rise-time of the AOM. We use the Sigmoid function with the slope of $\pm\Gamma_c$ to turn on/off the CF for all of the simulations, as shown in Fig. 3.12. This slope is chosen based on the curve fitting done on the experimental transient EIT data.

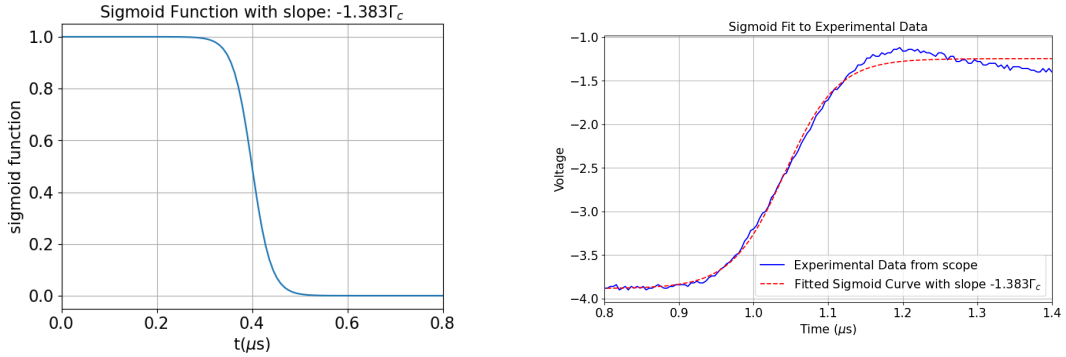

(a) (b)

Figure 3.12: Sigmoid function fitted to experimental data when turning off the pump. The slope is found to be -1.383Γ_c.

It turns out that one of the conditions to observe the transient oscillations is to have the rise-time (defined as the time when the function rises from 10% of its value to 90%) be a few times faster than the decay rate of the excited state. In Fig. 3.13, we can clearly observe this fact. Simulations suggest that in order to be able to see the oscillations clearly, we need to ramp off the CF with a slope of 2.5Γ_c, which corresponds to around 11 ns! This, however, is not feasible with our AOM, as the rise-time of our 110 MHz AOM is about 100 times higher than what is required.

Effect of different parameters on transient EIT

We are interested in understanding which parameters influence the behavior of transient EIT. Thus, we study different values of Ω_c, Ω_b, γ, and Δ. In all of the following simulations, we assume an ideal device that can ramp on/off the CF on demand. It was reported in [21] that with access to a laser capable of producing higher Γ_c (i.e., more powerful), transient EIT could be observed. However, our simulations do not support this argument, as there is no significant difference between high and low Rabi frequencies in the context of what is reasonable for EIT, as can be seen in Fig. 3.14.

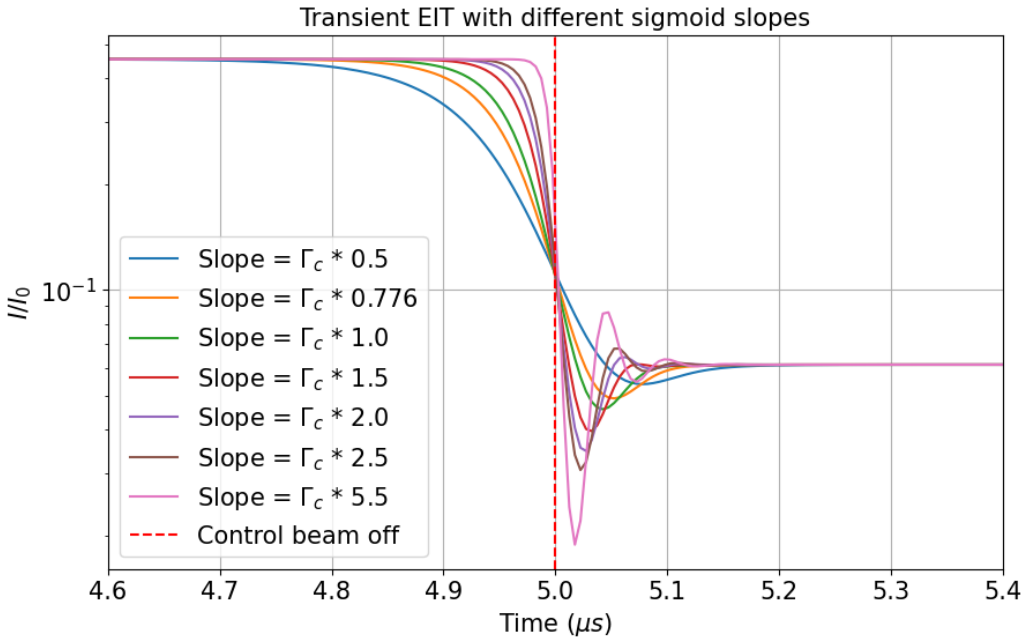

Figure 3.13: Effect of turn-off slope in observing the oscillations. Y-scale is logarithmic to capture all of the oscillations effectively.

Figure 3.14 illustrates the transient dynamics of the probe field's absorption after the pump field is turned off. As expected, the probe field exhibits increased absorption following the pump field's deactivation. Moreover, absorption is noticeably higher in a hot vapor cell compared to cold atoms, consistent with theoretical predictions. It is also evident that turning off the pump field with higher field strength significantly amplifies the probe field's absorption compared to lower pump field strengths. This behavior is observed consistently across the 4-level atomic system (Figure 3.14), the 3-level atomic system (Figure 3.16), and the 6-level atomic system (Figure 3.15). However, the 6-level atomic system exhibits the highest absorption among the three systems when the pump field is turned off.

The next parameter we study is Ω_b, which influences the frequency of oscillations when the pump field is turned on. As shown in Figure 3.18, increasing Ω_b leads to an increase in the frequency of oscillations until the system no longer satisfies the conditions for Electromagnetically Induced Transparency (EIT) or Coherent Population Trapping (CPT), resulting in the absence of transient EIT. This behavior is consistent with predictions from analytical equations. Higher oscillations and gain are observed when the system operates under CPT conditions, where the strengths of the probe and pump beams are equal. Additionally, Doppler broadening smoothly

dampens the oscillations, as expected. Figure 3.17 illustrates that after turning off the pump field in the 4-level system, the atomic ensemble begins to strongly absorb the probe field. Higher probe field strengths correspond to greater absorption after the pump field is turned off. This behavior is similarly observed in the 3-level system, as shown in Figure 3.19. However, an important observation is that the presence of additional atomic levels and Doppler broadening tends to smooth out the damping effect of the absorption.

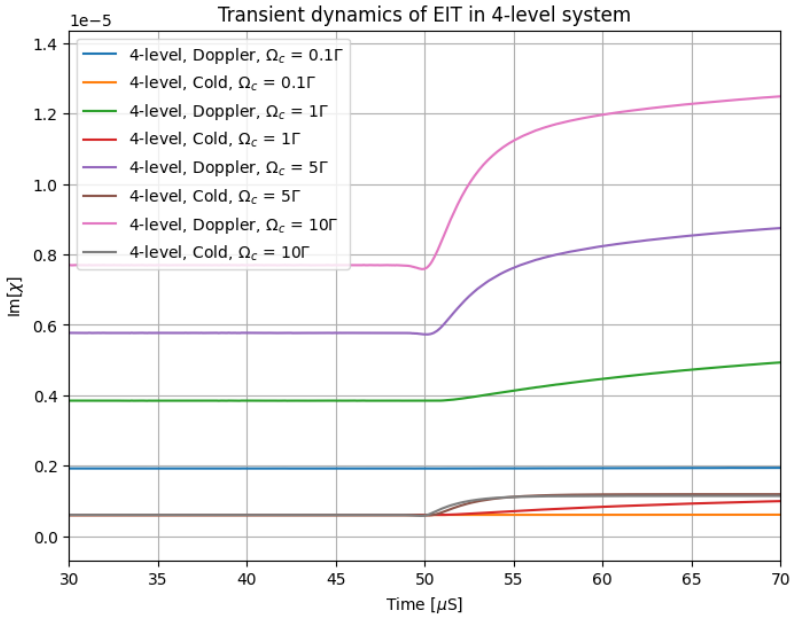

Figure 3.14: Changing Ω_c to observe the impact of it on 4-level transient EIT when the pump is turned off.

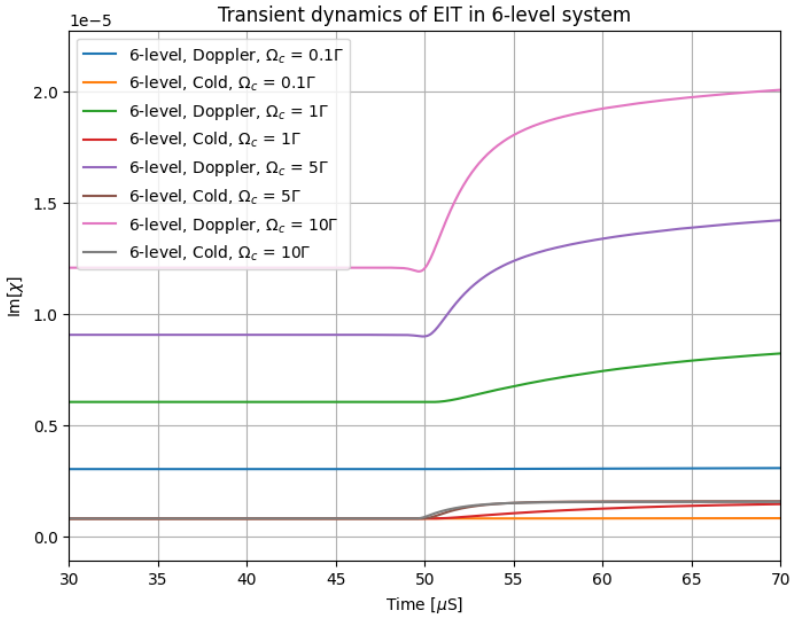

Figure 3.15: Changing Ω_c to observe the impact of it on 6-level transient EIT when the pump is turned off.

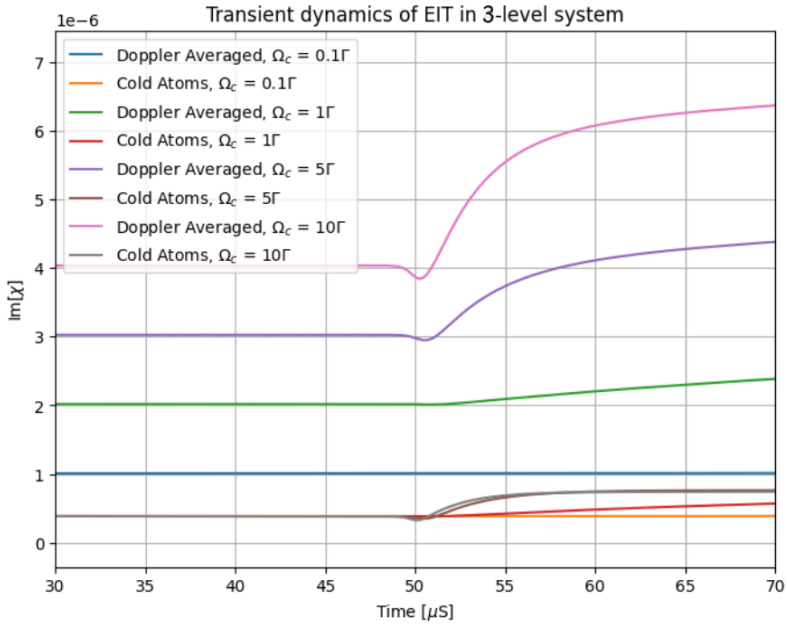

Figure 3.16: Changing Ω_c to observe the impact of it on 3-level transient EIT when the pump is turned off.

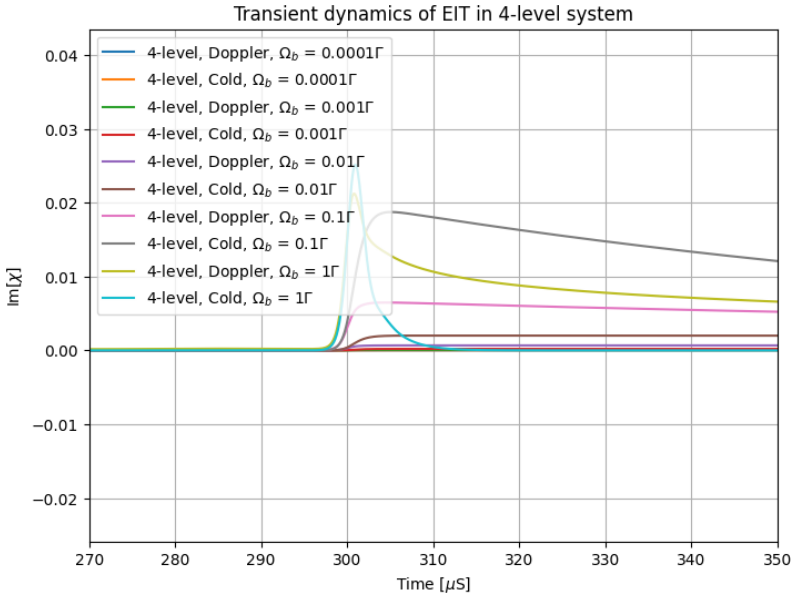

Figure 3.17: Changing Ω_b to observe the impact on transient EIT in the 4-level system when the pump is turned off. Data for cases where $\Omega_b < 0.001\Gamma$ overlap due to the scale used in this plot.

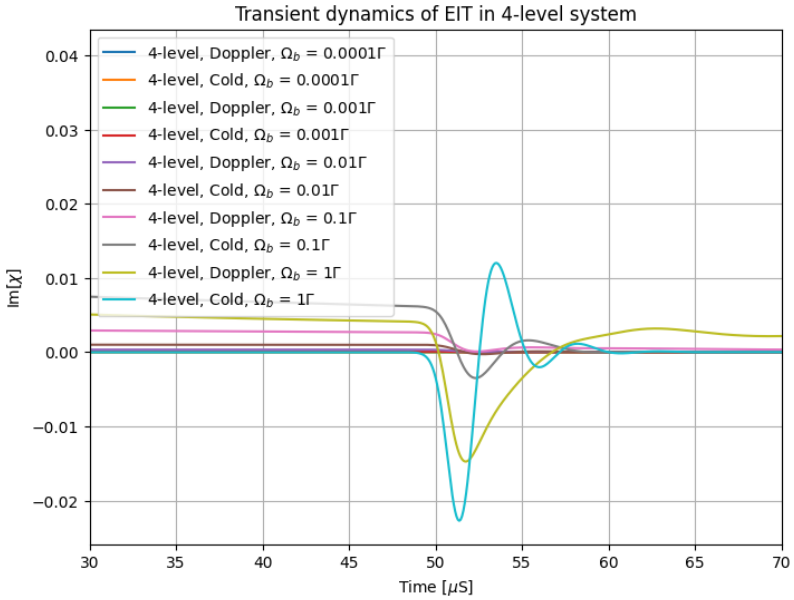

Figure 3.18: Changing Ω_b to observe its impact on transient EIT in the 4-level system when the pump is activated. Data for cases where $\Omega_b < 0.01\Gamma$ overlap due to the scale used in this plot.

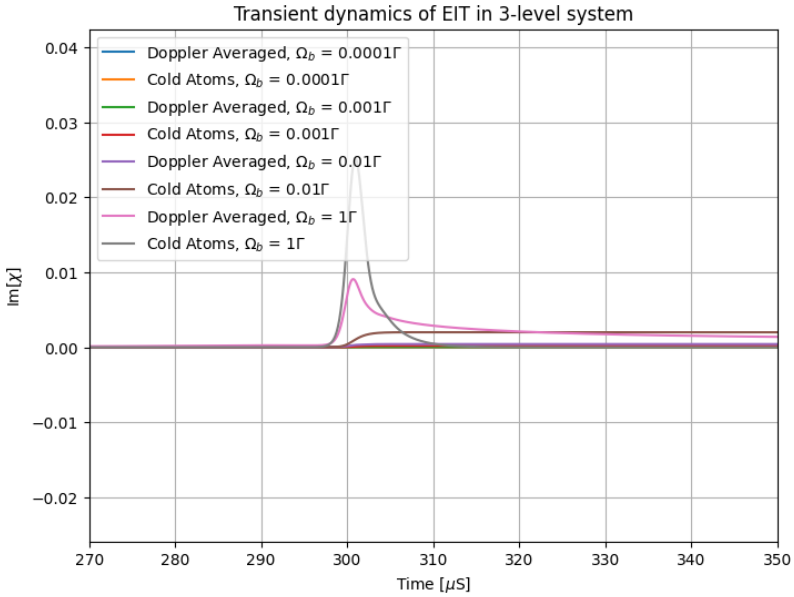

Figure 3.19: Changing Ω_b to observe the impact on transient EIT in the 3-level system when the pump is turned off. Data for cases where $\Omega_b < 0.01\Gamma$ overlap due to the scale used in this plot.

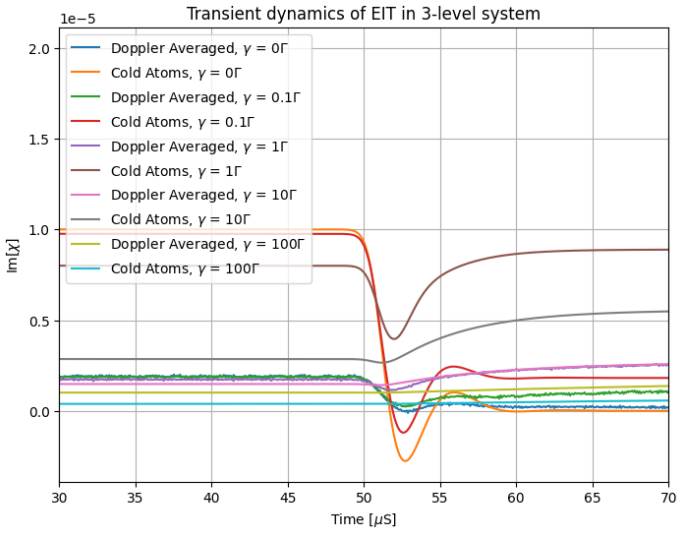

Figure 3.20: Changing γ to observe the impact of it on transient EIT when the pump is turned on.

The study of γ in the Λ system reveals its significant impact on damping transient oscillations. Figure 3.20 demonstrates that lower ground-state decoherence results in higher gain and reduced damping of oscillations when the pump field is turned

on. Under these conditions, the EIT effect is perfectly established, and the system eventually settles into a state of no absorption. Conversely, increasing ground-state decoherence hinders EIT by preventing maximum transparency, causing the system to settle at higher probe field absorption levels and eventually making it impossible to establish the EIT effect. Similar behavior is observed in the 4-level system (Figure 3.22) and the 6-level system (Figure 3.25), which aligns with theoretical expectations. Additionally, in the 3-level system, the transient gain vanishes as ground-state decoherence increases.

As the decay rate increases, interference between excitation pathways diminishes, degrading the quality of EIT. While it is theoretically possible to counteract this effect by significantly increasing the pump Rabi frequency ($\Omega_c \gg \gamma$), excessive pump power can induce side effects such as Four-Wave Mixing (FWM). Furthermore, when the pump field is turned off, increased ground-state decoherence leads to higher probe field absorption. This behavior is illustrated in Figures 3.21, 3.23, and 3.24. Moreover, systems with a greater number of atomic levels exhibit higher probe field absorption under these conditions.

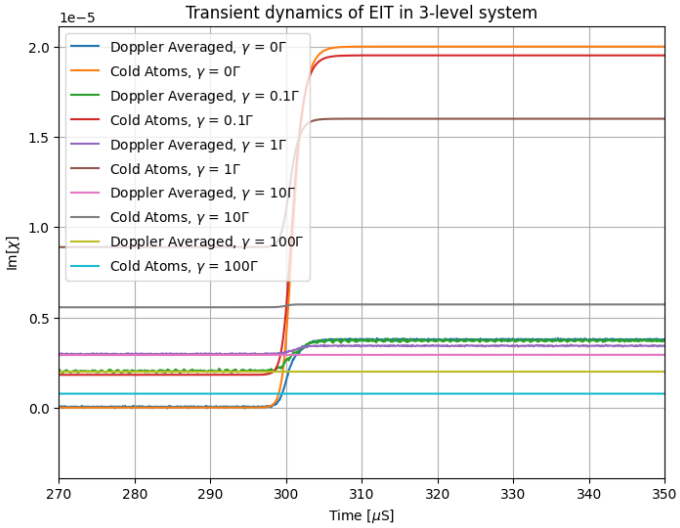

Figure 3.21: Changing γ to observe the impact of it on transient EIT when the pump is turned off.

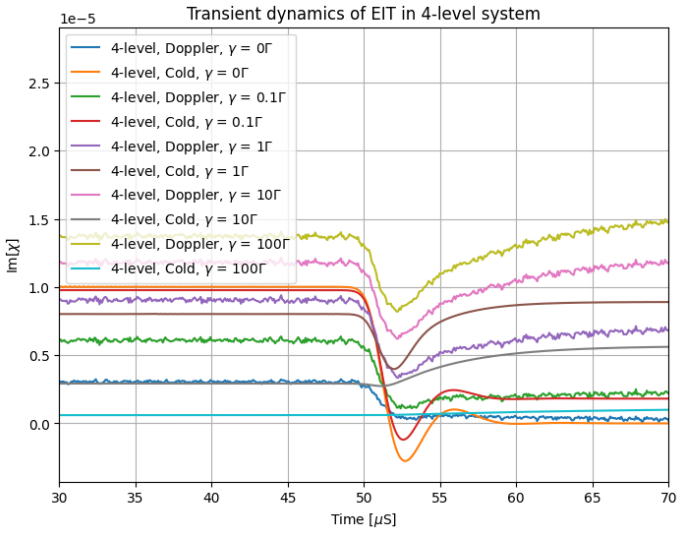

Figure 3.22: Changing γ to observe the impact of it on transient EIT in the 4-level system when the pump is turned on.

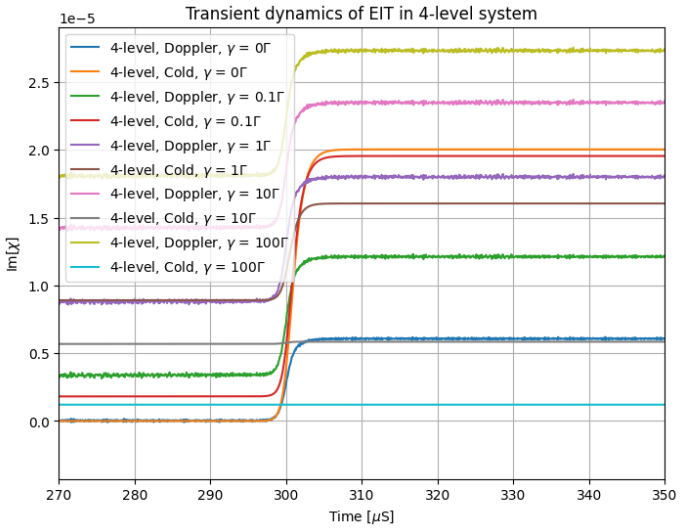

Figure 3.23: Changing γ to observe the impact of it on transient EIT when the pump is turned off.

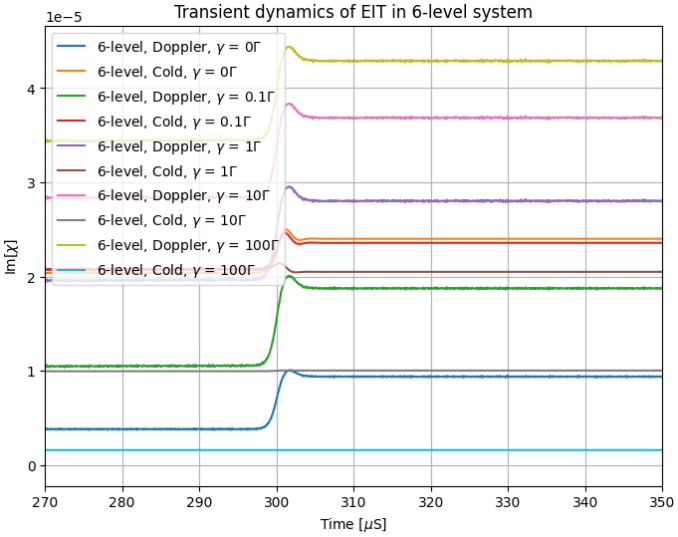

Figure 3.24: Changing γ to observe the impact of it on transient EIT in the 6-level system when the pump is turned off.

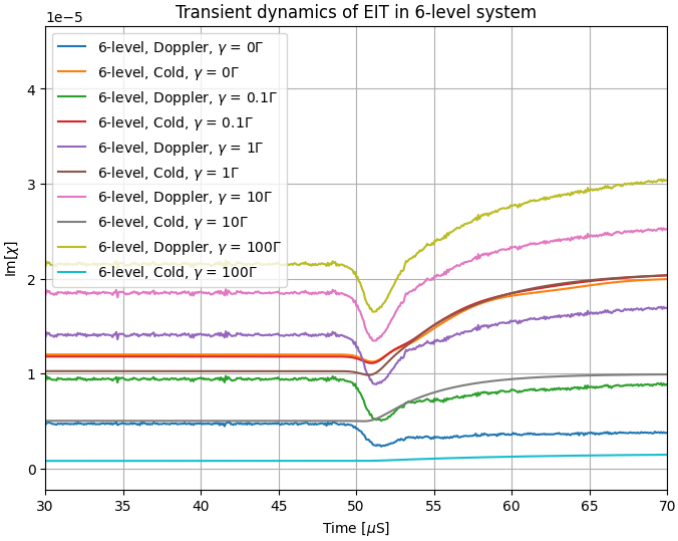

Figure 3.25: Changing γ to observe the impact of it on transient EIT in the 6-level system when the pump is turned on.

3.3 Further theoretical predictions

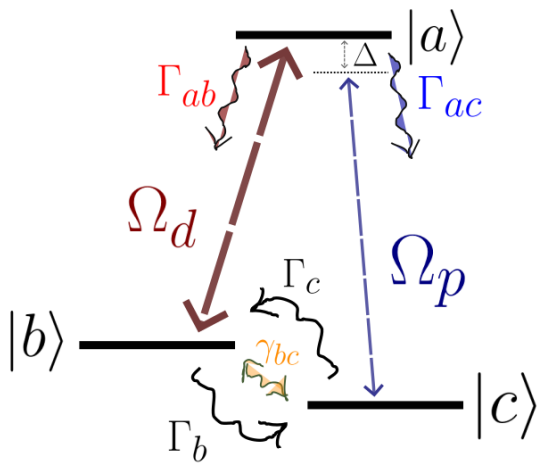

Figure 3.26: Schematic of the generic three-level system under consideration.

In this section, we employ Wolfram Mathematica to theoretically investigate a method for quantifying GSD in an AE through the absorption or transmission behavior of the PF. Additionally, we explore the N-type scheme and its potential application in developing an all-optical transistor. The system's dynamics are governed by the following rate equations:

$$
\begin{aligned}
0 &= i\Omega_d\rho_{ba} - i\Omega_d^*\rho_{ab} + i\Omega_p\rho_{ca} - i\Omega_p^*\rho_{ac} - 2(\Gamma_{ab}+\Gamma_{ac})\rho_{aa},\\
0 &= -i\Omega_d\rho_{ba} + i\Omega_d^*\rho_{ab} + 2\Gamma_{ab}\rho_{aa} - \Gamma_b\rho_{bb} + \Gamma_c(1-\rho_{aa}-\rho_{bb}),\\
0 &= -i\Omega_d(\rho_{aa}-\rho_{bb}) + i\Omega_p\rho_{cb} - (\Gamma_{ab}+\Gamma_{ac}+\frac{\Gamma_b}{2})\rho_{ab},\\
0 &= i\Omega_d^*(\rho_{aa}-\rho_{bb}) - i\Omega_p^*\rho_{bc} - (\Gamma_{ab}+\Gamma_{ac}+\frac{\Gamma_b}{2})\rho_{ba},\\
0 &= i\Omega_d\rho_{bc} - i\Omega_p(\rho_{aa}-(1-\rho_{aa}-\rho_{bb})) - \left(\Gamma_{ab}+\Gamma_{ac}+\frac{\Gamma_c}{2}+i\Delta\right)\rho_{ac},\\
0 &= -i\Omega_d^*\rho_{cb} + i\Omega_p^*(\rho_{aa}-(1-\rho_{aa}-\rho_{bb})) - \left(\Gamma_{ab}+\Gamma_{ac}+\frac{\Gamma_c}{2}-i\Delta\right)\rho_{ca},\\
0 &= i\Omega_d^*\rho_{ac} - i\Omega_p\rho_{ba} - \left(\gamma_{bc}+\frac{\Gamma_b+\Gamma_c}{2}+i\Delta\right)\rho_{bc},\\
0 &= -i\Omega_d\rho_{ca} + i\Omega_p^*\rho_{ab} - \left(\gamma_{bc}+\frac{\Gamma_b+\Gamma_c}{2}-i\Delta\right)\rho_{cb}.
\end{aligned}
\tag{3.5}
$$

We find that with different values for decoherence, we observe different characteristic absorption profiles for the PF while scanning its field strength.

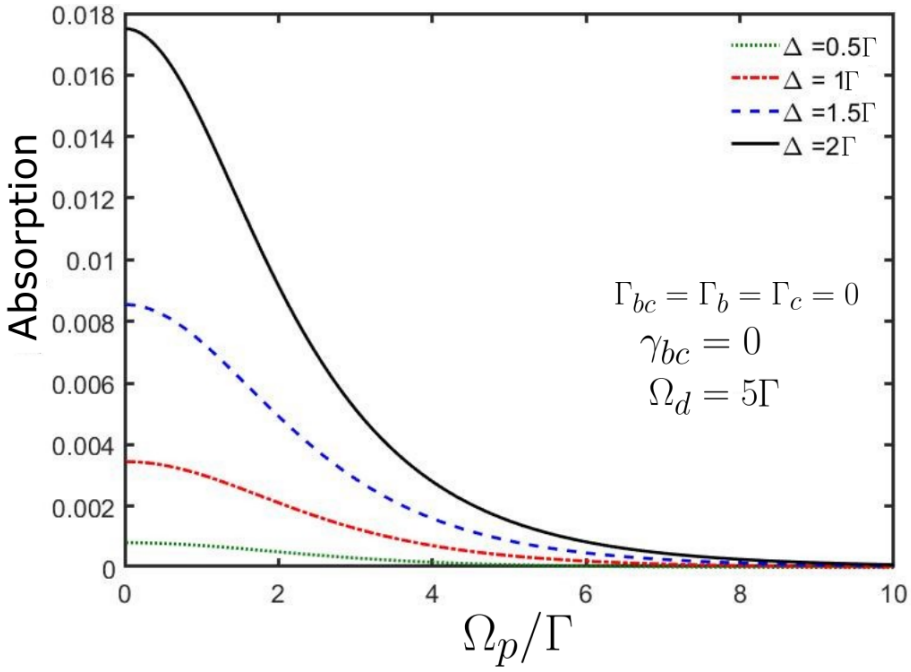

Figure 3.27: Effect of different detuning Δ on absorption of PF.

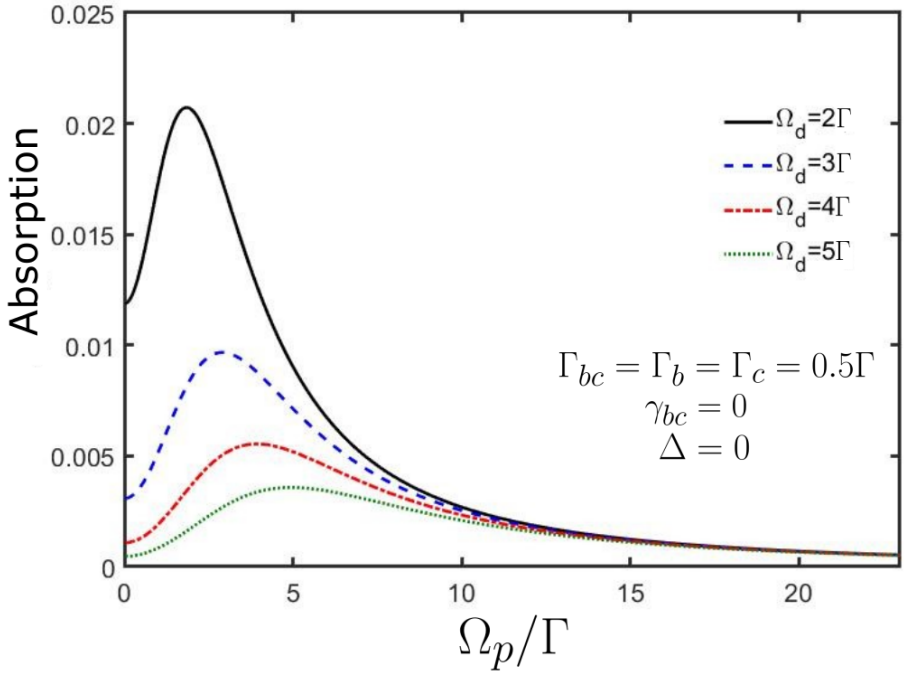

Figure 3.28: Effect of nonradiative decay (NRD) or population exchange while changing the strength of the CF and being on resonance.

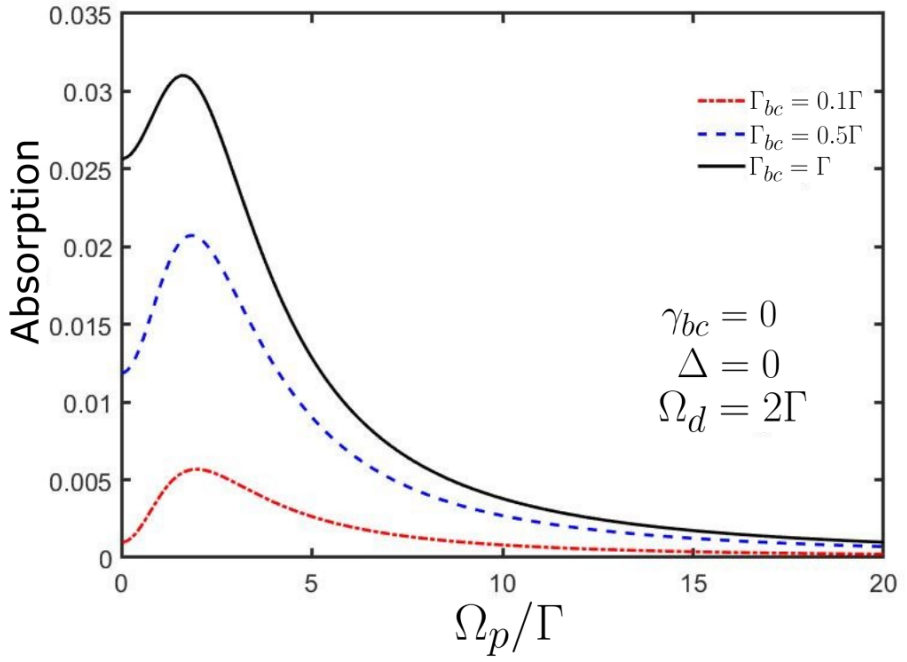

Figure 3.29: Effect of NRD on the absorption while the CF strength is set to the highest achieved characteristic absorption in the last simulation.

Considering we have a generic 3-level system as shown in Figure 3.26, we start by writing the rate equations as in equation 3.5, where Γ_{ab} and Γ_{ac} are the decay rates from the excited state. We define the PF as Ω_p and the CF as Ω_d. We consider the GSD and population exchange as γ_{bc}, and Γ_c, Γ_b, respectively. We begin by assuming there is no NRD and no decoherence, i.e., $\Gamma_b = \Gamma_c = \gamma_{bc} = 0$. For the rest of this study, we assume that the decay rates are equal: $\Gamma_{ac} = \Gamma_{ab} = \Gamma$.

By changing the detuning of the probe, we observe that the absorption decreases when the detuning is lowest, which aligns with expectations since we are in the EIT regime. This serves as a sanity check for the rest of the simulation. Now, we add the NRD effect while we are on resonance and observe that there is a characteristic peak in the absorption of the PF. For a lower strength of the CF, this absorption is higher, which makes sense since if the strength of the PF prevails over the strength of the CF, there is no longer transparency for the PF.

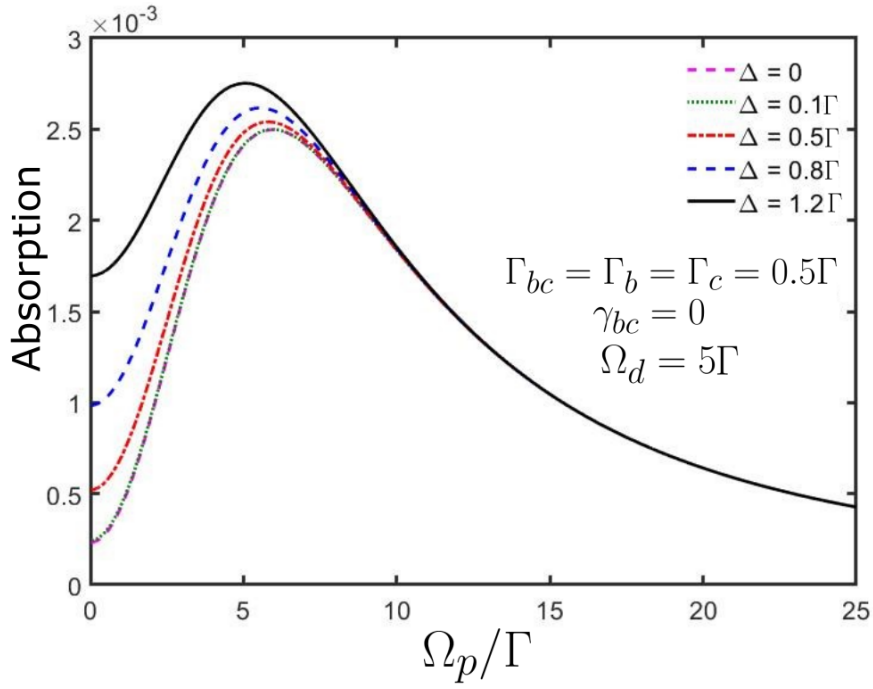

Figure 3.30: Effect of detuning on the absorption while setting the CF to a strong value and setting NRD to a reasonable moderate value of 0.5Γ.

Next, setting the strength of the CF to the value that gave us the highest characteristic absorption peak and changing the NRD reveals that with lower NRD, there is lower absorption. This is expected because NRD quantifies collisions between atoms.

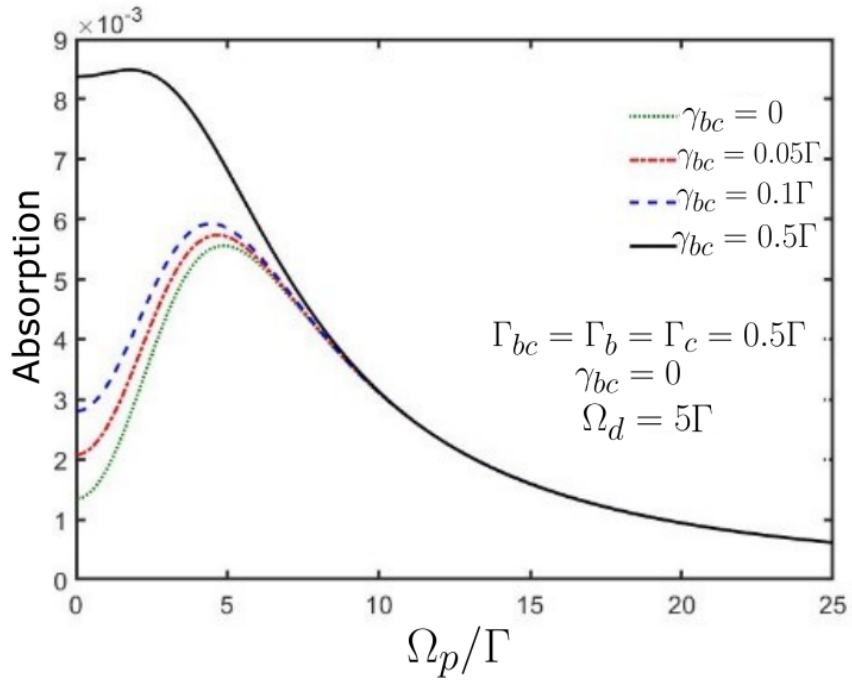

Figure 3.31: Effect of GSD on the characteristic absorption of the system while sweeping over the PF strength.

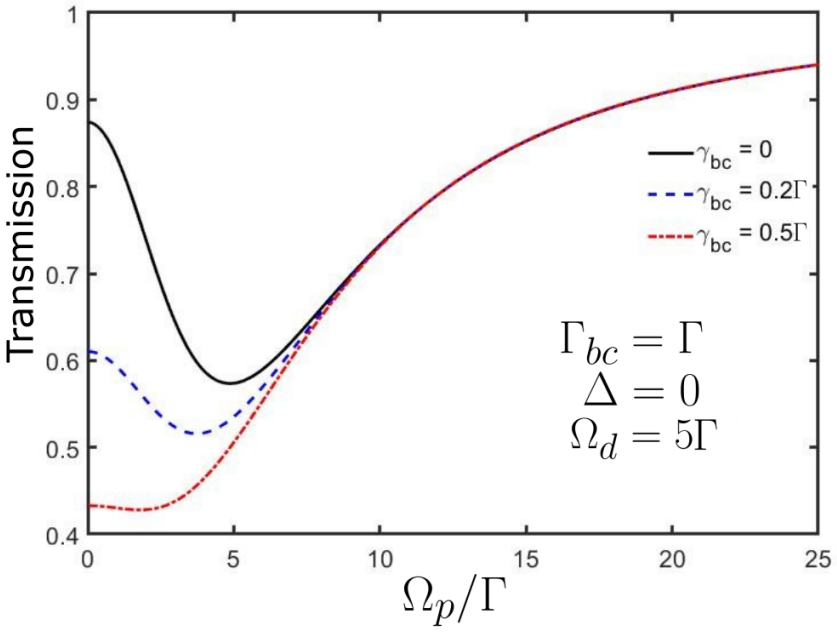

Figure 3.32: Effect of GSD on the transmission of the PF.

These collisions, if not elastic, can exchange the population, which leads to cor-

ruption of the EIT effect. Setting the NRD to a moderate value and the CF to a reasonably strong value, we change the detuning of the probe to further check the fact that if we are not on resonance, the absorption is higher compared to being on resonance. Note that being detuned has some tolerance, as can be seen in Figure 3.30, where both plots for $\Delta = 0$ and $\Delta = 0.1\Gamma$ are similar in terms of characteristic absorption.

Adding the GSD to the system shows that with higher decoherence values, we observe more absorption peaks while sweeping over the PF strength. This makes sense due to the dephasing of the AE that has undergone CPT. For a complementary result to Figure 3.31, in Figure 3.32 we show the transmission of the PF with different decoherence values of the GS. This, again, agrees with the intuition that with lower decoherence, more transmission should be expected.

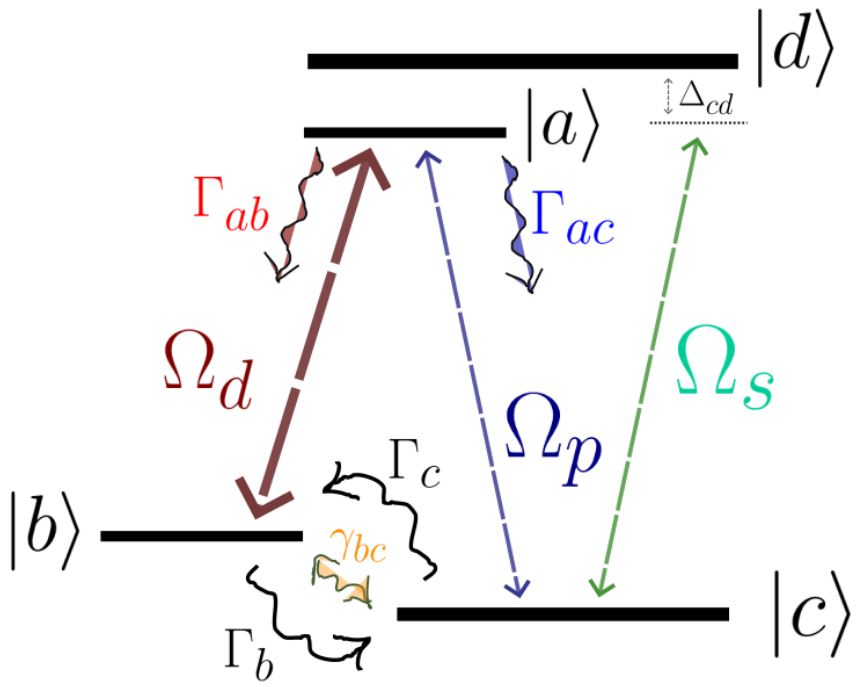

Figure 3.33: Atomic structure for all-optical transistor in N-type scheme.

Experimentally, an AOM or Electro-Optic Modulator (EOM) can be employed to amplitude-modulate the pump power and observe the SS absorption profiles obtained here. Moving forward, one can explore the transient behavior of these absorption profiles as the pump power is scanned, enabling us to benchmark the time required to measure GSD using this method.

Additionally, these characteristic absorption curves and peak absorption points

could be leveraged to optically limit light transmission at higher pump power levels. By introducing a third optical field as Ω_s to couple one of the GSs to a second excited state, creating an N-type scheme as it can be seen in figure 3.33, the ACSS could be utilized to dynamically adjust the absorption peak. This adjustment could effectively function as an all-optical transistor, actively controlling pump power to protect optical sensors by allowing transmission only at lower intensities. Adding a cavity to this configuration could also facilitate a Rydberg blockade, where only a SP passes through—a valuable feature for highly sensitive optical detectors like Superconducting Nanowire SP Detectors (SNSPDs), particularly in QKD applications, where it helps protect sensors from damage. Particularly, this could be useful as a countermeasure against blinding attack [54, 55, 56] for SP detectors in QKD.

Chapter 4

Experimental Methods

Since this study is considered to be more experimental than theoretical or purely simulation-based, we must discuss the essential tools required to investigate the physical effects in question. The majority of the time was spent building, designing, and optimizing these tools over the past two years. Although I am summarizing the work with a few sentences, in practice, it takes much more effort than it may seem.

4.1 Stable External Cavity Diode Lasers

The outcome of any QO or quantum photonics study is highly dependent on the quality of the light source used. The desirable laser must have a wide free-spectral range while being collimated and single-mode (though in some applications, multi-mode lasers may be used). The phase stability, or laser linewidth, is another crucial figure of merit for the quality of the light source. Achieving a perfect laser often requires significant financial resources, and given limited funding, we opted to build our own ECDL rather than purchasing off-the-shelf commercial tunable lasers from companies like Toptica, MogLab, or Santec.

To build everything from scratch, one must first understand the fundamental principles behind how these devices work. We asked ourselves, "What are the essential components needed to construct a laser from scratch?" The answer lies in understanding the operational principles and control mechanisms of lasers.

Solid-state diode lasers are made using PN-junction semiconductors, and laser diodes are abundant for the wavelength range we work with. However, these diodes need further configuration to ensure they provide all the required functionalities of a

laser. Semiconductor diode lasers typically have a relatively wide gain profile, on the order of 1 THz, and their center frequency is sensitive to temperature and injected current. These diode lasers are constructed to form a Fabry-Perot cavity with the front facet of the semiconductor.

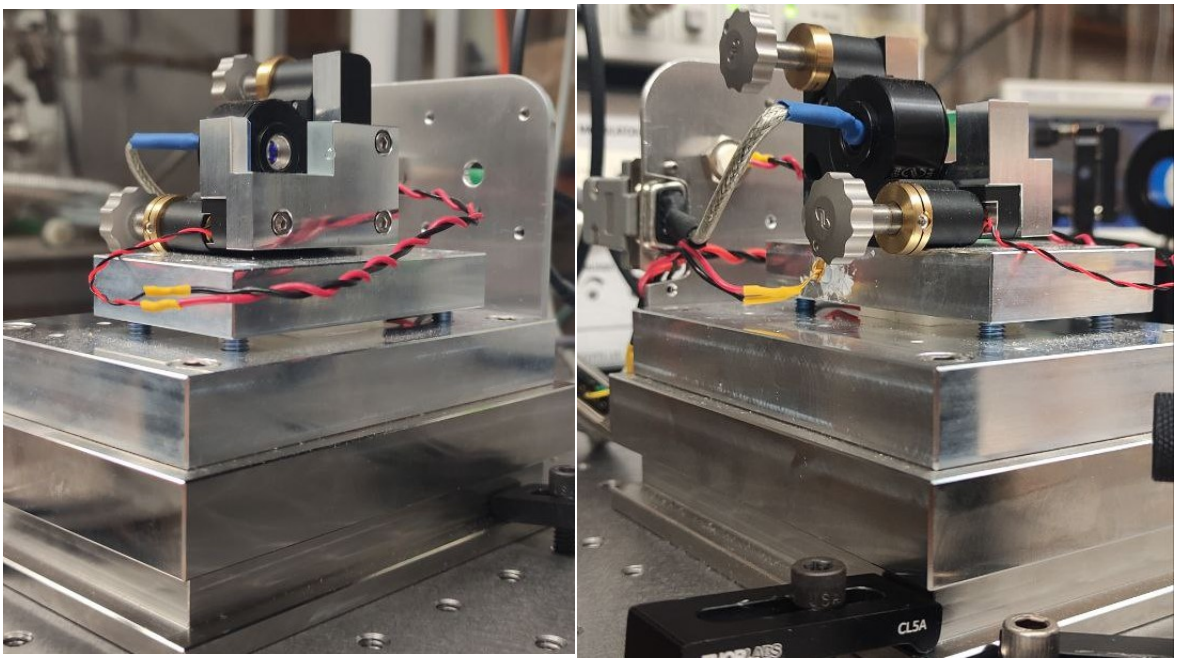

(a) (b)

Figure 4.1: Front and back view of one of our ECDLs.

Essentially, this cavity generates frequency combs, each of which represents different spectral modes with short linewidths on the order of tens of MHz. Unfortunately, this is not acceptable for the experiments we aim to conduct. Therefore, we use an external cavity to select a deterministic single-mode and reduce the linewidth by two orders of magnitude.

To form the external cavity, we use a blazed diffraction grating where the first order of diffraction couples back into the laser diode, and the zeroth order is reflected to a mirror and out-couples from the cavity. The cavity can be fine-tuned by adjusting knobs on the plate that connect the mirror and grating to align the Feedback (FB) light into the laser and adjust the frequency. This process can be done manually or with a piezoelectric transducer. The latter offers a range of several GHz at a BW of several kHz, which is helpful when scanning the laser fast enough to observe full transition manifolds on the scope within a few μs.

Often (if not every time) when starting experiments with these types of ECDLs, manual frequency adjustments are required to ensure there are no mode hops and the laser output remains single-mode. Additionally, controlling the laser output frequency can be fine-tuned by regulating the temperature to a resolution of 0.1°C using a Peltier thermoelectric cooler. Using a temperature sensor and a FB loop to maintain a desirable value is one method to stabilize the diode laser's frequency. Another way to change the frequency output of the laser is by adjusting the injected current, which has a higher BW impact on the frequency (up to 1 MHz) compared to other methods. Once all the controllable parameters are well understood, one can purchase the required equipment at a reasonable price and begin assembling the laser based on the design. The design is inspired by [57], where the Littrow reflection method is used to adjust the lasing frequency. Please refer to C for more information on how to align and tune these type of diode lasers.

Since we built multiple lasers (five in total) from scratch, a sense of emotional attachment developed, leading us to name them. This allowed us to easily reference specific lasers during group meetings. Notable laser names in this work include Chuck, Toppy, Jimmy, and Charles. Some of these lasers met their end (fried due to various reasons), and we honored their service. They explored the horizons of dark and bright states of AEs and now rest in peace on the rest-shelf of the UVAMO lab.

4.2 Phase-stability for Pump and Probe

There are a few ways to achieve the 6.8 GHz frequency separation between pump and probe frequencies to obtain EIT in a Λ-scheme using the D_1 transition line. One approach is to use two separate lasers, where the relative phase must be locked via an Optical Phase Locked Loop (OPLL) [58]. Initially, we attempted this method but faced significant technical challenges in locking the lasers due to noise creeping into our FB electrical signals from unknown sources, which we humorously referred to as "quantum worms."

Another method involves using the injection locking technique, where a master laser with low linewidth and high phase stability injects a portion of its light into a slave laser. The slave laser then inherits the properties of the master laser and locks its phase to that of the master. We briefly explored this technique, but it remains an unfinished avenue of research.

Alternatively, a third method utilizes an EOM to create sidebands. In this ap-

proach, both frequencies are generated from the same laser, and the relative phase between the pump and probe frequencies is much more stable compared to other techniques. In this technique, if the EOM is driven by a sine wave, sidebands are generated as a result of modulating the carrier frequency with the sine wave. The amplitude and frequency of the carrier signal remain unchanged after modulation, but the frequency and amplitude of the sidebands are dependent on the voltage and frequency of the sine wave input to the EOM. Assuming the light input to the EOM has a frequency of ω, the phase-modulated light output after the EOM can be expressed as

$$E_{out} = Ae^{i\omega t + i\beta \sin(\Omega t)}, \tag{4.1}$$

where β is the modulation depth and Ω is the frequency of the sinusoidal voltage applied to the EOM. Given that the amplitude of the input electrical signal is small, one can use a first-order expansion in the Taylor series and write

$$E_{out} = A\left(e^{i\omega t} + \frac{\beta}{2}\left(e^{i(\omega+\Omega)t} - e^{-i(\omega-\Omega)t}\right)\right). \tag{4.2}$$

From the above equation, we interpret that the effect of the electrical signal with relatively small amplitude β and frequency Ω results in the original carrier frequency with a slight reduction in intensity due to insertion loss. Additionally, two other frequencies or sidebands are generated: one at $\omega + \Omega$ and another at $\omega - \Omega$, with intensities proportional to $\beta/2$ multiplied by the initial intensity in the output. In reality, there are higher-order modulated frequencies, but they are small enough to be neglected.

To be more precise, one can use the Jacobi-Anger expansion to derive the amplitudes of higher-order sidebands:

$$Ae^{i\omega t + i\beta \sin(\Omega t)} = Ae^{i\omega t}\left(J_0(\beta) + \sum_{k=1}^{\infty} J_k(\beta)e^{ik\Omega t} + \sum_{k=1}^{\infty}(-1)^k J_k(\beta)e^{-ik\Omega t}\right). \tag{4.3}$$

4.3 Spectral filtering

The output of the EOM must be spectrally filtered so that the desired sideband is distinguished from the carrier frequency with a separation of 6.8GHz. Otherwise, one would observe a beat note between the sidebands and the carrier frequency on a spectrum analyzer connected to a fast photodetector. To achieve this, we use a cavity

called an etalon, which performs the spectral filtering for us.

The etalon consists of two parallel, flat, semi-transparent mirrors separated by a fixed distance. The input light undergoes multiple reflections, and during each bounce, the phase accumulated by the light is given by

$$2\pi \times 2n_{\text{silic}} D \cos(\theta)/\lambda, \tag{4.4}$$

where n_{silic} is the index of refraction, D is the thickness of the etalon, and θ is the angle of the beam inside the etalon. Based on the incident angle of the beam, the optical thickness of the etalon, and the wavelength, constructive and destructive interference occur. Only specific frequencies are allowed to pass through the etalon, while other frequencies undergo destructive interference and are suppressed. Thus, the transmission spectrum of an etalon consists of a series of peaks, separated by the Free Spectral Range (FSR), given by

$$\text{FSR} = \frac{1}{2n_{\text{silic}} D}. \tag{4.5}$$

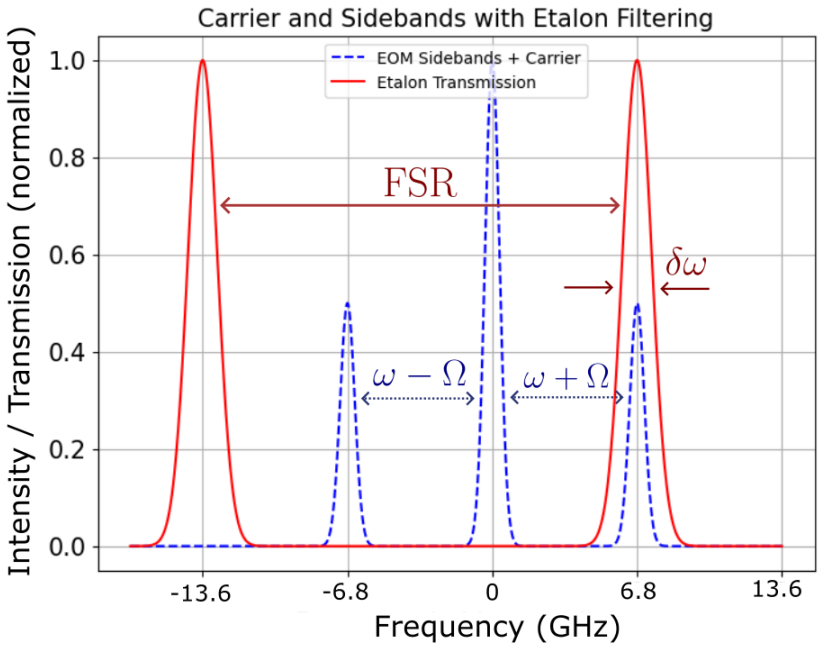

Figure 4.2: Spectral filtering of Etalon while suppressing unwanted frequencies.

The FSR is measured in cm^{-1} (wavenumber) in equation 4.5. It is important to note that the reflectivity of the mirrors does not affect the FSR directly. However,

higher reflectivity reduces the FWHM and increases the finesse of the cavity. Finesse (F) is defined as

$$\mathrm{F} = \frac{\mathrm{FSR}}{\mathrm{FWHM}}. \tag{4.6}$$

In our experiment, we use a temperature-tunable Fabry-Perot etalon. This etalon is made from solid fused silica with an FSR of 0.5/cm and a finesse of 30. It is coated with a dielectric coating designed for optical wavelengths ranging from 700nm to 850nm, with a thickness of 6.743mm for the 0.5/cm FSR and 3.371mm for the 1/cm FSR. Figure 4.2 provides an intuition on how the etalon achieves spectral filtering by selectively transmitting the desired frequencies while suppressing other unwanted frequencies generated by the EOM.

4.4 Acousto-optic modulator

For turning the light source on/off on demand with a reasonable rise time of approximately 120ns, one can use an optical modulator, either an EOM or an AOM. It is not feasible to directly turn the laser on/off using the laser controller due to the laser's transient response time, which is much higher than the required rise time. Therefore, an AOM with a BW of 120MHz is used to achieve the desired rise time.

When incident light impinges on the AOM crystal at the Bragg angle θ_B, a diffraction pattern occurs, where the diffraction orders at each angle θ are governed by the following relation:

$$2\Lambda \sin(\theta) = m\lambda, \tag{4.7}$$

where m is the order of diffraction, which can take integer values from $-n^{\mathrm{th}}$ to $+n^{\mathrm{th}}$ order (in practice, orders from -2 to +2 are considered). Here, Λ represents the wavelength of sound, and λ is the wavelength of light. Since the 0^{th} order travels in the same direction as the incident beam, we are mainly interested in the $\pm 1^{\mathrm{st}}$ and $\pm 2^{\mathrm{nd}}$ orders.

There is a correlation between the intensity of the sound and the intensity of the light, which can be exploited for modulating the intensity of light. By adjusting the voltage applied to the AOM, one can modulate the light intensity. Theoretically, the intensity of the 1^{st} order can vary anywhere between 0% and 80%. Furthermore, the AOM is capable of scanning the frequency of the laser based on photon-phonon scattering, where the incoming light source interacting with the crystal absorbs energy from the Radio Frequency (RF) pulse, resulting in an up/down frequency shift within

the order of the AOM's BW, $\omega \rightarrow \omega + Mf$. Here, the variable M ranges from $\pm 1^{\text{st}}, 2^{\text{nd}}$, up to the n^{th} diffraction order, and f represents the BW of the AOM. The energy and momentum relations for phonon-photon scattering are as follows:

$$\omega_n = \omega + \omega_{\text{phon}} k_n = k + k_{\text{phon}}, \tag{4.8}$$

where ω_n and k_n are the frequency and wavevector of the n^{th} diffracted light, respectively.

To avoid the formation of standing waves inside the crystal, which is undesirable, an absorber is placed on the opposite side of the RF input pulse to prevent this. The angle of the diffracted light has a relation with the frequency shift, and this can be described by Bragg's law:

$$\sin \theta_B = \frac{k_{\text{phon}}}{2k_n}. \tag{4.9}$$

Sometimes, the altered direction of the wavevector induced by Bragg scattering is undesired due to the alignment difficulties it causes. In situations where the optical fields are mode-matched, such as in EIT, and any deflection in the wavevector could impair the results, one can double-pass the beam through the AOM. As a result, the optical frequency shifts twice compared to a single-pass AOM.

A convenient setup involves placing the AOM at the focus of a lens, where any light exiting the lens from the AOM will be parallel to the unmodulated beam. The modulated light is then retro-reflected and focused back into the AOM using a mirror. In this configuration, the position of the mirror becomes somewhat arbitrary, but the orientation is fixed to be normal to all beams. However, double-passing the AOM may cause intensity modulation, which might not be desirable for certain experiments.

4.5 Oven

To conduct the experiment, we designed a temperature-tunable oven with a resolution down to 0.1 °C. Temperature control is crucial as it allows us to manage the number density of the AE, thereby adjusting the OD. The tunability of temperature ranges from 25 °C to 80 °C. The Rb atoms are contained within the oven in the form of natural abundance Rb vapor. The VC is 2.5 cm in length with a 1-inch diameter glass tube for optical access. While VCs are relatively inexpensive and easily accessible, atomic vapor ensembles suffer from DB and higher decoherence rates compared to

MOT clouds.

Designing a suitable oven requires considering several factors, including how to heat and control the temperature of the cell and how to enclose the system to prevent the MF from causing Zeeman shifts in the atomic energy levels. In the initial design, we did not prioritize magnetic shielding using μ-Metal (μM), which later became a bottleneck in the experiment. Eventually, we had to completely abandon the original oven case and use a cylindrical surplus magnetic shield from one of the labs, carefully placing the VC inside and heating it with a heat gun.

In any case, the heating element used in the oven was McMaster-Carr PN 6455N18, a 50W electrical bar heater designed for insertion into a 1/4 inch diameter hole. Ironically, the heater introduced an unwanted induced MF from its own wires, which was one of the main reasons we ultimately stopped using the oven. The induced MF caused Zeeman shifts in the atomic levels, degrading both the EIT depth and linewidth.

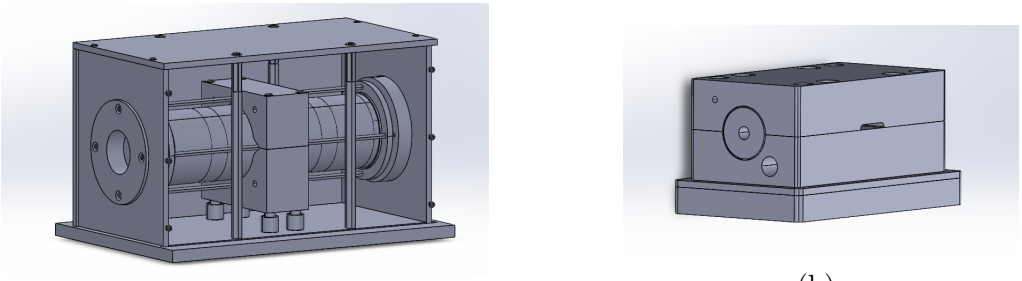

(a) (b)

Figure 4.3: Two versions of the oven designed with the help of Brendan Mackey and Chris Secord for the EIT experiment. The new version (a) with magnetic shielding. The old version (b) without magnetic shielding.

To stabilize the temperature within the oven, we used a Thorlabs ITC 102 controller along with a K-type thermocouple attached to the oven. The heating element, thermocouple, and Rb cell were kept in thermal contact with an aluminum cell casing that had a uniaxial hole for optical access. The primary purpose of the casing was to provide mechanical stability and maintain thermal contact for all the components. A secondary purpose was to increase thermal stability, which led to the intentional oversizing of the casing to increase the thermal mass of the system. Clearance was provided between the groove for the Rb cell and the casing to account for thermal expansion, and a compressible Teflon film was used to ensure constant contact. Additionally, a brass cold finger was employed to prevent Rb from condensing on the

optical surface of the cell. After experimenting with this version of the oven and failing to achieve the desired experimental results in EIT, we decided to redesign the oven. For the next version, we incorporated layers of μM shielding to surround the atomic cell inside the oven. This provided magnetic shielding while also allowing us to introduce solenoids for the dual purposes of demagnetization and applying a stable and uniform MF along the axis of laser propagation. The two design versions of the oven are illustrated in Fig. 4.3.

4.6 Photodetector

Detection of light played a pivotal role in every experimental result presented in this thesis. In our experiment, we dealt with classical coherent light sources with high photon fluxes, in the order of 10^{12} photons per second, where standard Si PDs are typically employed. Si PDs function via the photovoltaic effect, where the energy from incident light excites electrons across the small energy gap between the valence and conduction bands, generating an electrical signal proportional to the light intensity. Most of the detectors used in this thesis are homemade with the help of Nick Braam, which allowed us to easily modify them to achieve the desired BW and gain. This customization was beneficial for experiments that required either high gain or high BW.

The minimum detectable light level in conventional detectors is constrained by electronic noise, specifically Johnson-Nyquist noise, inherent in any circuit due to thermal agitation of the electrons, regardless of the amount of voltage applied. Below this threshold, the signal becomes indistinguishable from the noise, resulting in a low signal-to-noise ratio. In general, to analyze light signals, two approaches are commonly used: time-domain detection, where the signal's amplitude is plotted as a function of time, and frequency-domain detection, where the amplitude of a specific frequency range is displayed.

Given the high frequencies of optical fields, around 10^{14}Hz, direct measurement of light frequencies with electronics is impossible. To overcome this, heterodyne detection can be employed, where the beat frequency spectrum is measured by mixing the optical signal with a local oscillator, allowing the optical frequencies to be indirectly observed. We used this technique for a sanity check on the EOM and AOM to ensure that the generated frequencies were consistent with our expectations.

Although we have not entered the realm of SP detection in this thesis, I would

like to briefly mention some techniques used to detect SPs, as I had the opportunity to work with them during my internship at QTi. For experiments conducted in the SP regime, where individual photons are the primary unit of measurement, standard Si detectors fall short in sensitivity. Instead, highly sensitive devices such as SNSPDs or avalanche photodiodes (APDs) are employed. These detectors operate in different ways but share the goal of detecting extremely faint light levels with high precision.

SNSPDs work by transitioning from a superconducting to a resistive state when they absorb a photon, resulting in a measurable pulse. APDs, on the other hand, rely on the avalanche multiplication process, where a SP generates an electron-hole pair, which is subsequently amplified into a detectable current pulse. Two key figures of merit for these detectors are time jitter and dead time. Ideally, both should be minimized in experiments such as QKD or light storage multiplexing in rare-earth ion-doped crystals.

4.7 Electrical Circuits

Nearly every electronics board used in our lab was designed and assembled in-house. This approach provided flexibility for modifications and improvements, which would have been much more challenging with off-the-shelf devices. On the downside, it also meant that nothing worked perfectly on the first try, and repeated iterations were necessary to achieve fully functional devices. Given the significant amount of time dedicated to this task, I would like to discuss a few key electronic circuits developed in our lab that were crucial for our experiments.

4.7.1 Laser Piezo Driver

In external cavity diode lasers, one critical degree of freedom is the ability to control and alter the angle of the diffraction grating to achieve lasing at the desired wavelength. This is accomplished by adjusting the angle of the diffraction grating, which is mounted on piezoelectric actuators. These actuators contain special crystals that deform in response to applied voltage. By precisely controlling the voltage, we can adjust the length of the crystal and thus the angle of the diffraction grating. The voltages required for this process can be as high as 100 volts. Initially, we attempted to build a voltage amplifier circuit to supply the necessary voltage, but this introduced unwanted noise into the laser frequency. To mitigate this issue, we opted for

a commercial surplus voltage amplifier from our electronic shop, which provided a more stable frequency output.

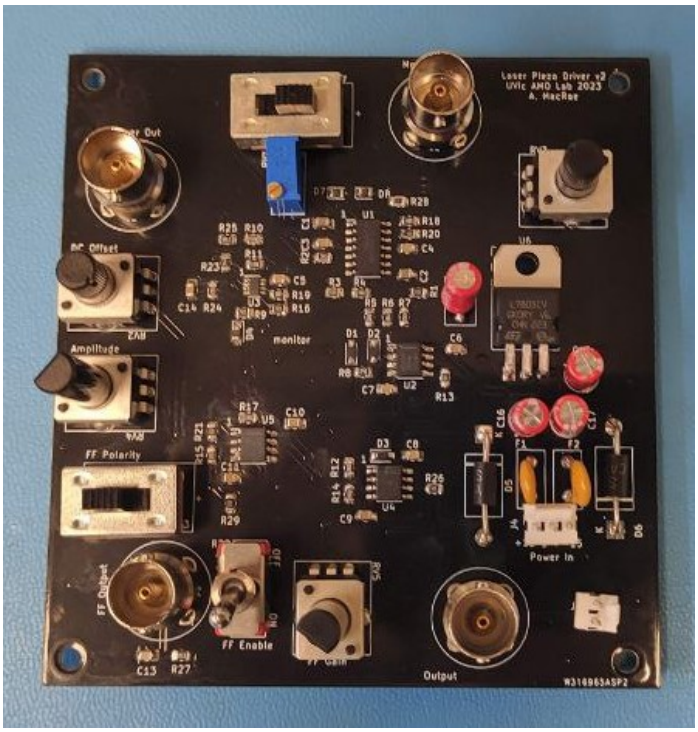

Figure 4.4: Laser Piezo Driver board designed with the help of Andrew MacRae.

The piezoelectric driver and ramp generator we eventually designed is based on a cost-effective high-voltage Operational Amplifier (op-amp). The circuit board comprises several important sections:

1. **Ramp Generator:** Generates a symmetric ±10V ramp with adjustable amplitude and frequency, controlled by resistors, capacitors, and the input voltage to the LM2902 Op-Amp.

2. **DC Offset Control:** This is a critical feature in QO experiments, especially when fine-tuning the system to stay on resonance.

3. **Low-pass Filter (LPF):** We used a 30Hz LPF to eliminate high-frequency noise, ensuring cleaner operation of the laser.

4. **Additional Features:** These include trigger output, modulation input, and Feedforward (FF) capabilities. The FF function, with variable gain, is essential for achieving a high mode hop free tuning range.

While the FF capability is beneficial, it can also introduce noise when locking lasers using an OPLL. Thus, in some cases, fine balancing of the gain of FF is required to minimize noise while maintaining Mode-Hop Free Range (MHFR).

With all that said, our custom piezoelectric driver is a cost-effective alternative to commercial drivers, allowing us to save funds for purchasing more crucial equipment. However, we also aimed to outperform commercial products in terms of noise performance, which is especially important for precision experiments in QO.

4.7.2 Laser Protection Circuit

Commercial devices often come with a hefty price tag, largely due to the extensive effort engineers invest in minimizing noise and designing protection mechanisms to safeguard components from power supply malfunctions. One of the most common causes of damage in electronic devices is an electrical surge which is a sudden, transient rush of current, voltage, or power through the circuit. Given that we built our lasers from the ground up, it was rather obvious to devise a protection system to prevent the lasers from being destroyed by these electrical surges.

The laser protection circuit we designed is a small circuit board consisting of several forward 1N4148 diodes, a few 1N5711 diodes, and a combination of resistors and capacitors arranged as a LPF. This configuration acts as a surge absorber, designed to mitigate detrimental electrical transients. The circuit is installed between the laser current supply and the laser diode, intentionally placed as close to the diode laser as possible. This proximity ensures maximum protection against voltage spikes and surges, preserving the integrity and longevity of the laser diode.

4.7.3 Dichroic Atomic Vapour Laser Lock Board

Achieving frequency stability in a diode laser is not only essential but a key element in various QO experiments. However, stability is a vague concept unless referenced against a known standard. Then, the question arises: what should be considered as the reference? The best candidate that fulfills all the requirements is the Rb atoms themselves! In this case, Rb atoms allow us to lock the laser to an error signal generated by atoms moving inside a VC, distributed according to the MBD.

One practical application of this stabilization technique is in MOTs, where a stable laser frequency is crucial for achieving high OD and optimal trapping conditions. The DAVLL method enables frequency stabilization by converting the absorption signal

of light passing through a VC into a FB signal [59]. This FB signal is used to lock the laser to a desired resonance frequency.

DAVLL works by detecting the difference between right- and left-circularly polarized light after it passes through the Zeeman-shifted atomic VC. The polarization difference is proportional to the voltage correction required to adjust the laser frequency to the desired value. A negative FB loop applies this correction, stabilizing the laser frequency to a specific HF transition in the Rb atoms.

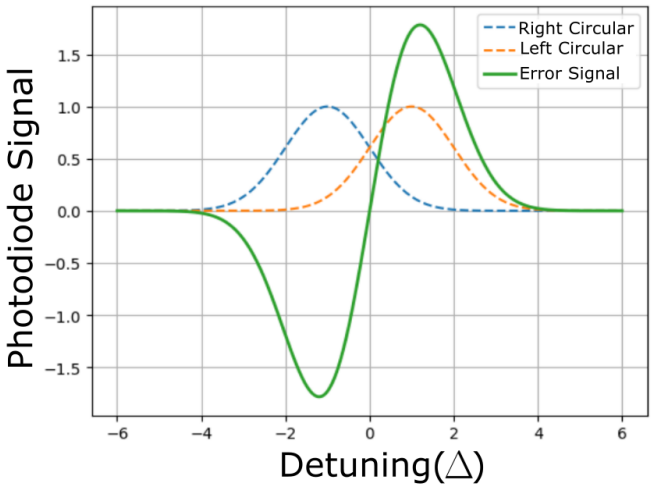

Figure 4.5: DAVLL error signal generated from subtracting the signals of right- and left-circularly polarized light.

The error signal in DAVLL is generated by subtracting the signals of right- and left-circularly polarized light as it can be seen in figure 4.5, which are shifted due to the applied MF in the atomic VC. These two polarization components are separated using a polarizing beam splitter (PBS) after the cell. The zero-crossing point of this error signal marks the region where the laser can be locked using a Proportional-Integral-Derivative (PID) controller. This zero-crossing can be shifted using a $\lambda/4$ plate before the cell, allowing adjustments up to roughly 200 MHz.

Since the core of any DAVLL board is the PID controller, it is crucial to understand the fundamentals of control theory. In a closed-loop control system, the ”process variable” is the parameter we wish to stabilize. The set point is the desired value of the process variable, and the error signal is the difference between the set point and the actual process variable.

In our experiment, the process variable is the difference in the left- and right-circularly polarized light absorbed by the Rb vapor, while the set point is one of the

Rb transition line frequencies. The goal is to drive this difference to zero, indicating that the laser frequency is balanced between the magnetic sub-levels of that transition. The actuator in this system is the piezoelectric element in the external cavity diode laser, which controls the laser's frequency.

To maintain a stable lock, the error signal must be properly regulated by the PID controller, preventing the laser from drifting away from the desired frequency. If the FB signal is not filtered well, the DAVLL board can act as a "double agent," causing more harm than benefiting the system. The PID controller consists of three main components:

1. **Proportional (P):** The proportional component responds to the difference between the process variable and the set point (the error term). The proportional gain controls the output response relative to the error. If the gain is too low, the response will be insufficient, but if it is too high, the system may oscillate and fail to stabilize at the set point.

2. **Integral (I):** The integral component accumulates the error over time. If the error persists, the integral term will continue to grow, driving the system toward the set point. However, if the integral gain is too high, the system may become saturated, leading to overshooting and instability.

3. **Derivative (D):** The derivative component responds to the rate of change of the error. It dampens the system's reaction to rapid changes in the error signal, making the system more stable. However, the derivative term is highly sensitive to noise, and if not carefully tuned, it can destabilize noisy systems.

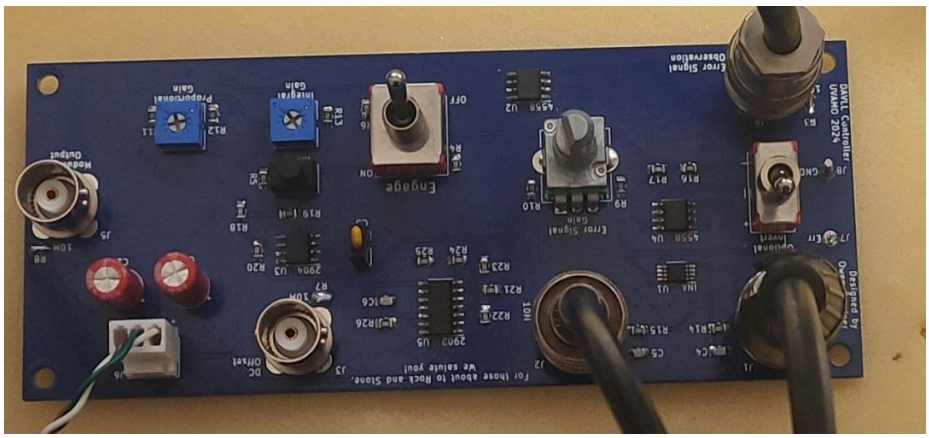

Figure 4.6: DAVLL board designed and soldered with the help of Owen Sandner

For our DAVLL board, which uses LM741 op-amps, these components work together to fine-tune the laser frequency. The proportional gain must be carefully adjusted to balance responsiveness with stability, while the integral and derivative terms ensure that the system reaches and maintains the desired set point without oscillation or excessive noise sensitivity. We change the gain of each PID parameter using potentiometers connected to each op-amp controlling the output of each PID parameter.

Chapter 5

Experimental results on transient EIT

It is worth noting that the experimental study is still an ongoing project. We are anticipating a publication as an outcome of this work.

Initially, when we discussed the demonstration of transient EIT, the effect of MF perturbations and the rising time of the pump turn-off were unappreciated. As we progressed, conducting the experiment without proper magnetic shielding and using a chopper wheel to turn off the CF yielded no meaningful data. Due to the low budget for the lab, we devised innovative ideas to magnetically shield the cell, but the quality of this shielding remained questionable. A surplus cylindrical-shaped μM was used for shielding, but it was unclear when it was last demagnetized, making it unrealistic to expect exceptional performance. Nevertheless, we obtained some preliminary results that provide proof of principle.

However, several questions still require careful consideration. For example, how can we discriminate between the effects of optical pumping and transient EIT? How can we experimentally minimize the effects of environment-induced decoherence? What is the exact nature of the transient EIT? Is it caused by optical pumping, as described by Scully et al. [28] [page 229, fig 7.5], or is it due to the oscillation of atomic population between the dark and bright states, as described in [60]? Furthermore, some controversial results from the literature do not align with each other or with our simulation results. One notable example is the impact of Γ_c in achieving transient gain, as argued in [21], where it is suggested that high enough RBF can result in transient gain. Though, in [60] it has been shown that excessive intensity

(RBF) impairs the transient oscillations, and as a result, no transient gain could be expected. On the other hand, our simulations show that the transient EIT does not meaningfully change with the strength of the RBF. Therefore, a more in-depth study is needed to fully understand the dynamics of EIT.

With that said, in this chapter, transient oscillations of EIT in a hot atomic Rb VC are investigated experimentally, where the CF is turned off non-adiabatically and the absorption of the PF is observed with respect to time. The goal is to determine the GSD by observing the damping rate of the transient oscillation. The decay rate of these oscillations provides a window to quantifying the dephasing of the EIT atomic system. The experiment was conducted in both HF and Zeeman configurations, which will be detailed in the following sections.

5.1 Hyperfine EIT

The transient EIT effect studied in this work is illustrated in figure 2.1, operating on the D_1 transition line of ^{87}Rb. The CF is right-circularly polarized and couples the $F = 2 \rightarrow F' = 1$ transition. The PF is left-circularly polarized and couples the $F = 1 \rightarrow F' = 1$ transition. These particular transitions were chosen to reduce cross-talk between ^{87}Rb and ^{85}Rb in the naturally abundant VC. It is worth noting that other transitions have been explored, and the best result has been observed with this particular transition in terms of the depth and linewidth of EIT.

5.1.1 Experimental Setup

The experimental setup is displayed in figure 5.1. The experiments presented in this thesis were performed using a 2.5 cm atomic cell containing natural abundance Rb gas without any buffer gas. The cell's temperature was controlled and adjusted within a range of 25°C to 100°C (though it was not designed for temperatures exceeding 75°C. Operating at higher temperatures caused some cosmetic imprints from Teflon on the surface of the cell, but these did not affect performance). The fields were produced by a self-made ECDL and EOM, accompanied by an etalon to isolate the desired frequency, separated from the carrier frequency by 6.834 GHz.

A small portion of the light ($\sim$ 1 mW) was split for optical diagnostics, including saturation-absorption spectroscopy ($\sim$ 900 μW) and interferometry ($\sim$ 100 μW). Spectroscopy was used to identify the desired transition and fine-tune the ECDL.

A Fabry-Perot interferometer ensured that the laser was operating in single-mode throughout the experiment.

The majority of the laser power ($\sim$ 20 mW) was directed towards generating the PF through the EOM. While this might seem generous for the PF, after accounting for losses and efficiencies—such as insertion loss, the relatively small amplitude of the sideband, and the etalon's efficiency—it is reasonable to end up with only a few hundred micro-Watts of OP for the PF.

Additionally, a significant portion of light ($\sim$ 10 mW) was used for the pump power, where it generated the first-order Bragg scattered light via an AOM, which switched the optical field on and off. To maximize AOM efficiency, we carefully mode-matched the light by adjusting the optical beam waist using a telescope technique and beam-walking into the AOM. As a result, the light after the AOM was shifted by 110 MHz in frequency. To observe the EIT feature, it is essential to consider the frequency shift introduced by the AOM and compensate for it using a DC offset to detune the field while locking onto the resonance. After passing through the AOM, the CF ($\sim$ 3 mW) and the PF ($\sim$ 200 μW) after the etalon are combined using a PBS and directed towards the VC. The beams are spatially mode-matched and then passed through a quarter-wave plate, converting their linear polarization to circular polarization.

Since the CF is horizontally polarized, it becomes right-circularly polarized after passing through the quarter-wave plate. Similarly, the vertically polarized PF is converted to left-circularly polarized light. We employed separate half-wave plates for the pump and PFs before their respective PBS' to allow for fine control of the power for each field, particularly for the PF.

Given that the beam diameter was reduced to achieve higher coupling efficiency, we employed another telescope to expand the beam waist, ensuring a narrow EIT linewidth. Research has shown that high-quality EIT (with a narrow linewidth and minimal GSD) is achieved when the CF covers the entire AE in the VC [24]. Therefore, the beam diameter for both the pump and PFs was increased to $\sim$ 2 mm.

After passing through the atomic medium, another quarter-wave plate, accompanied by a PBS, was used to separate the pump and PFs by converting them back to linear polarization. The PF was then directed to the detector, while the CF was blocked by a beam blocker.

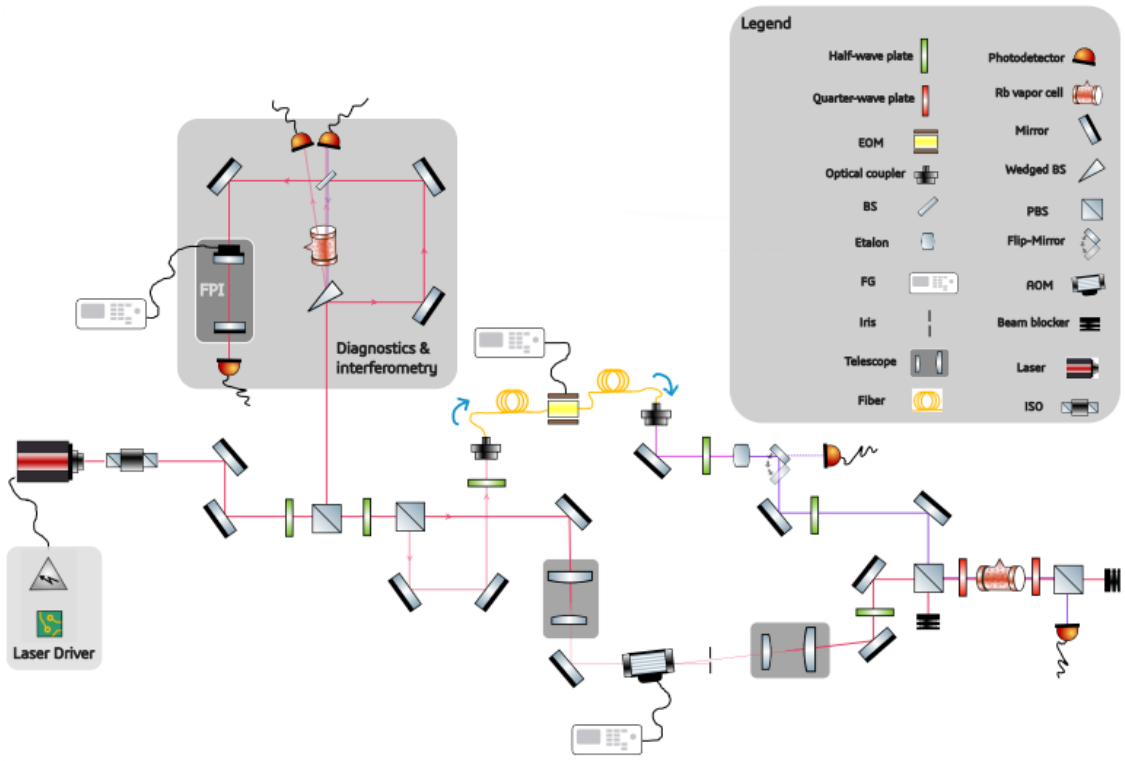

Figure 5.1: Experimental setup used to realize transient EIT.

5.1.2 Experimental Study of Transient EIT

A significant portion of time for this study was dedicated to designing and building the necessary equipment. Only experimental physicists can fully appreciate the effort and challenges involved in building devices from scratch and making them work, especially when operating under tight budget constraints. Creativity is essential to keep the research moving forward despite these limitations. Below, I will describe what is required experimentally to observe transient oscillations in EIT.

Magnetic Field Shielding using μ-Metal

To observe transient effects of EIT, it is crucial to reduce environment-induced decoherence in the atomic VC. One of the primary environmental effects is the ambient MF from the Earth and nearby equipment, which breaks the degeneracy of atomic energy levels and decreases the coherence time of the trapped atomic population in the GS. To mitigate this, the VC must be enclosed with solenoid coils inside a

cylindrical μM shield to provide protection from Earth's MF, particularly from fields perpendicular to the cylindrical axis.

Unfortunately, we had not anticipated the need for μM shielding early on, and acquiring the necessary shields from MuShield Inc. would have required a lead time of six months. Additionally, it would have taken three more months for our machine shop to implement the magnetic shielding into the newly designed oven. By that time, I would be nearing the end of my second year of my master's program, with my defense approaching soon. As a result, it was not feasible to design and construct a new oven with proper magnetic shielding within the available timeline.

In light of these constraints, we sought alternative ways to move the experiment forward. We were able to find some strips of μM from neighboring labs and stitched them together to create a makeshift shield box to cover the VC. To heat the cell, we used a heat gun alongside a thermistor to monitor the temperature and avoid overheating or cracking the VC. While the cell was not precisely temperature-controlled, the temperature drift over a few milliseconds was minimal, within 0.1°C, which was sufficient for the time scale of our experiments. Figure 5.2 shows our crude magnetic shield box.

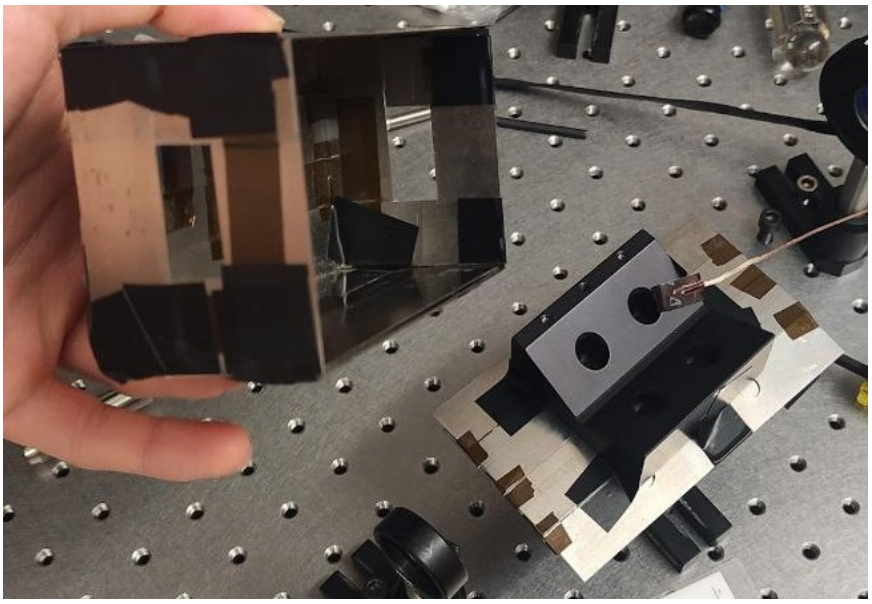

Figure 5.2: Crude magnetic shield box made from stitched strips of μM, used to cover the VC.

The result, however, was not ideal. When a magnet was brought near the cell covered by the magnetic shield, it was evident that the EIT linewidth widened, indi-

cating that the shielding was not fully functional. Another issue with this shield was that, once magnetized, there was no convenient way to demagnetize it. As a solution, we periodically removed the shielding and used a home-made solenoid to demagnetize it.

In the search for better magnetic shielding, we eventually found a surplus cylindrical magnetic shield from one of the undergraduate nuclear labs. We placed the VC inside this cylindrical shield and once again heated the cell using a heat gun to conduct the experiment. The outcome was significantly better than previous attempts, and this was reflected in the EIT linewidth, which narrowed to around 70kHz. Figure 5.3 shows this cylindrical magnetic shield with the VC placed inside.

(a)

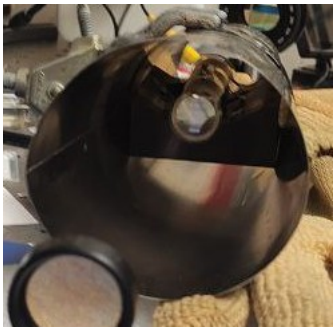

(b)

Figure 5.3: Surplus cylindrical μM shield containing the VC.

Figure 5.4 shows the EIT linewidth obtained using this improved magnetic shielding setup.

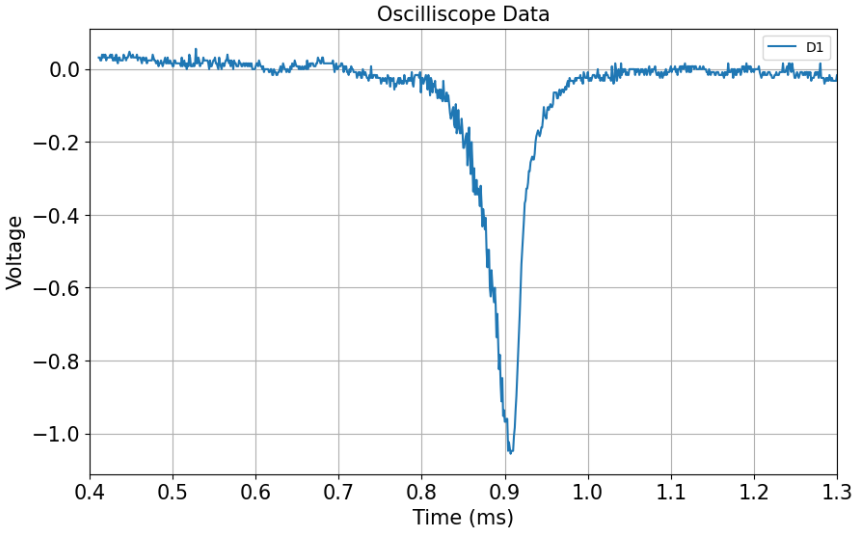

Figure 5.4: Experimental EIT width obtained from shielding the VC using a surplus cylindrical μM tube.

The EIT linewidth using a cubic magnetic shield made out of strip μMs, with an additional magnet placed near the cell to further cancel out the MF, is shown in figure 5.5. The linewidth is 0.75 MHz, which is ten orders of magnitude wider than the result obtained with the cylindrical μM shield. The conversion factor from the time domain to the frequency domain, after calibrating the scope to saturated absorption spectroscopy and the FSR of the Fabry-Perot interferometer, is given by the FWHM in the time domain multiplied by $\frac{8}{5\times10^{-3}}$. This yields the FWHM in the frequency domain.

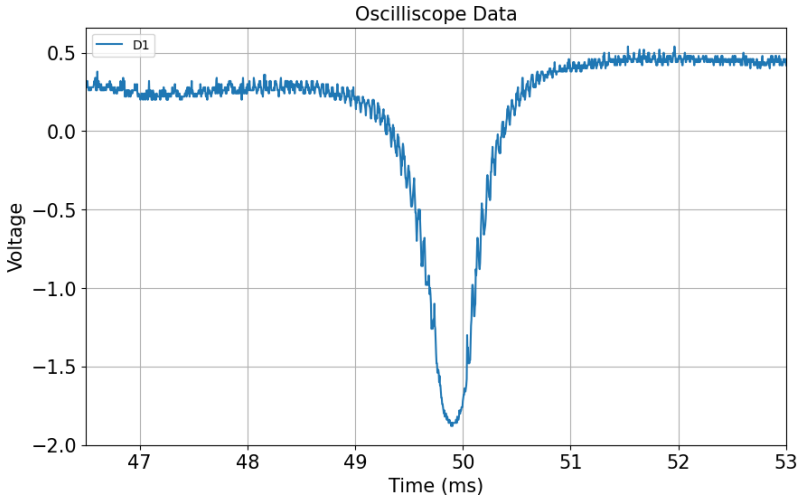

Figure 5.5: Experimental EIT width obtained without proper magnetic shielding.

In summary, ideally, spherical geometry for magnetic shielding is required to attenuate transverse fields to less than 10^{-6} Gauss. However, in real experiments, cylindrical shields with nested layers also work (since light needs to couple in and out of the cell, making spherical shields impractical). The μM alloy should have a minimum permeability of 80k. Additionally, each layer of the magnetic shield should be equipped with solenoid coils around it for degaussing. Typically, around 10A of AC is required to saturate the μM and remove the imprinted orientation of magnetic moments during degaussing.

The heater must be strategically placed inside the oven so that eddy currents or any induced MFs from the heater do not affect the experiment. As a result, the heating rods must be placed outside the first shielding cylinder since the AC applied to them generates a small MF that also needs to be shielded. These modifications were considered in the design of the latest version of the oven, but unfortunately, we are still waiting for them to be machined by the machine shop.

Optical field turn-off mechanism

The first step in exploring the transient effects of EIT is to switch off the CF relatively fast compared to the natural linewidth, ideally $\geq 0.5 \times \Gamma_c$, based on the simulations carried out. In our experiment, we explored both methods of creating a coherent superposition of the atomic GSs using two-photon resonant Raman fields, CPT, and EIT, and then non-adiabatically turning off the CF. The AOM in our setup was responsible for switching off the field via destructive phonon-photon interaction. However, how fast is fast enough? This question requires some attention.

Our AOM can turn off the light in approximately 20 ns, which corresponds to around $1.38\Gamma_c$ (since 20 ns is equivalent to 5×10^7 Hz, dividing this by $2\pi \times 5.75$ MHz gives us this result). However, after propagation into the VC, the ALI increases this rise time by a factor of 10, as atoms cannot immediately respond to changes in OP. The observable effect on the PF absorption after turning off the CF is modulation due to the GS coherence oscillating between dark and bright states.

Buffer gas and paraffin wall

One of the primary decoherence mechanisms in AEs is dephasing, which occurs due to collisions among atoms (atom-atom interactions) and between atoms and the cell walls. To mitigate this effect, it is common to introduce an inert buffer gas, such

as neon, into the cell. The buffer gas reduces the frequency of collisions between Rb atoms, thereby increasing the relaxation time and minimizing dephasing. As a result, the decoherence of the GS is significantly reduced. A detailed study on this phenomenon is presented in [61], where the authors demonstrate that increasing the buffer gas pressure leads to a decrease in the linewidth of the EIT feature, thereby reducing GSD. They also show that as the pressure increases, the linewidth narrows further. However, one must consider the caveat of pressure broadening, which can occur if the buffer gas pressure becomes too high. This can counteract the benefits of reducing dephasing by broadening the spectral linewidth.

In addition to using buffer gases, antirelaxation coatings, such as paraffin, offer another effective method for reducing dephasing in AEs. These coatings are applied to the inner walls of the VC to mitigate the dephasing caused by atom-wall collisions, which can otherwise randomize the quantum states of the atoms and lead to rapid decoherence. The paraffin coating allows atoms to bounce off the walls without losing their spin coherence, significantly extending the coherence time of the GS. In fact, with paraffin-coated cells, atoms can undergo tens of thousands of collisions before their quantum state is disrupted. The antirelaxation coatings work by ensuring that collisions with the walls are elastic, preserving both the velocity distribution and spin polarization of the atoms. This is crucial for experiments that rely on the precise control of atomic states, such as QM, magnetometry, and EIT experiments. As noted in [62], such coatings can dramatically increase the GS coherence time, enhancing the overall performance of these systems. Despite their advantages, antirelaxation coatings like paraffin also have limitations. They are sensitive to temperature and may degrade at higher temperatures by outgassing, which can reduce their effectiveness. Additionally, while they minimize atom-wall interactions, residual effects can still occur, particularly under high-pressure conditions or when stray EMFs are present.

In a nutshell, both buffer gases and antirelaxation coatings provide effective means to overcome dephasing in AEs. By carefully managing these factors, one can achieve longer coherence times and significantly improve the performance of QSs. With all of those lessons learnt from the dephasing of atoms inside the VC, we ordered a new cell that has 10 Torr neon buffer gas with paraffin coating on the side walls.

Four-Wave Mixing

Another mechanism for decreasing the coherence and broadening the EIT linewidth is FWM. At high temperatures and with a strong CF, in HF structures, it is possible to have photons generated in the form of noise caused by spontaneous FWM [63]. FWM can also contribute to line broadening in VC EIT systems, but not significantly for Zeeman EIT with a WP field, which is unable to drive the four-wave-mixing cycling transition. However, in coated-cell EIT systems using HF EIT, a strong CF is sufficient to observe such effects [62].

EIT linewidth measurement

One important figure of merit for EIT is its FWHM, which depends on the strength of the pump RBF. It has been shown that the FWHM of EIT is linearly dependent on the power of the CF [35]:

$$\mathrm{FWHM} = 2\gamma_{bc} + \frac{4|\Omega_c|^2}{2\mathrm{W}_d + \Gamma}, \tag{5.1}$$

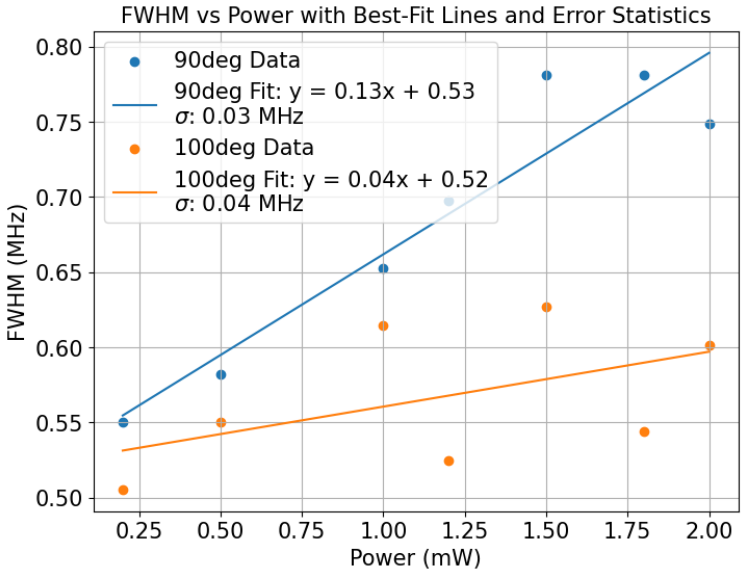

Figure 5.6: EIT linewidth dependency on the power of CF while shielding it with μM.

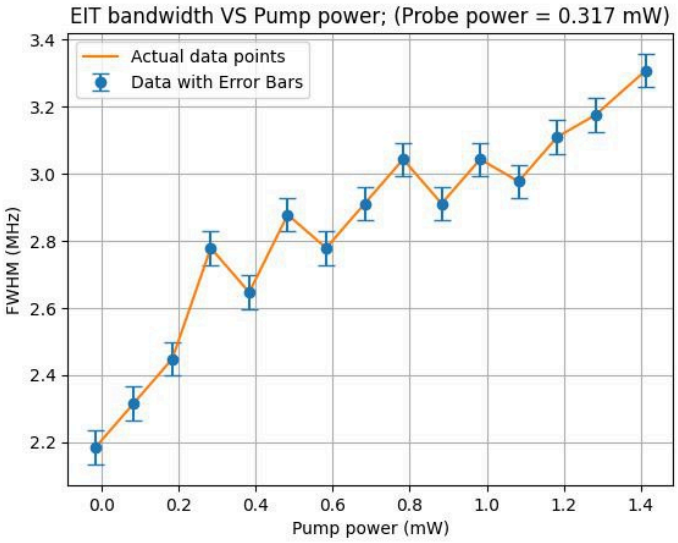

Figure 5.7: EIT linewidth dependency on the power of CF while not shielding it with μM.

where $|\Omega_c|^2$ is proportional to the intensity of the control beam, and thus proportional to its OP. The term $2W_d$ accounts for Doppler contributions to the EIT width. To observe the dependency of the EIT linewidth on pump power, we conducted measurements of the EIT linewidth by varying the power of the CF at two different temperatures. Figures 5.6 and 5.7 show the relative dependency of the EIT FWHM on the CF power. In our experiment, we captured the EIT features in the time domain and converted them into the frequency domain. We first fitted a Gaussian function to all the EIT data captured from the scope. Then, by calibrating the time domain with Rb line transitions on the scope, we transferred the time data to the frequency domain.

Experimental transient EIT

To observe transient oscillations of the PF, we sought to obtain the narrowest possible EIT linewidth, so that the modulated absorption of the PF could be clearly observed. Under CPT conditions, it has been shown that transient oscillations can be described by [60, 20]:

$$\alpha = Ae^{-\gamma_t t} + B\cos(\Delta_R t + \phi)e^{-R_{TC}t}, \tag{5.2}$$

where α is the absorption coefficient. The first term in the equation describes the spontaneous decay of atomic populations outside the Λ-scheme, with a decay rate of

γ_t. The second term accounts for transient coherence oscillations, with a decay rate of R_{TC}, which can be shown to depend on $\gamma_{bc} + \Omega^2/\Gamma$. To obtain the decoherence of the GS, γ_{bc}, one can gradually reduce the CF power and measure the decay rate of the transient oscillations. Ultimately, by extrapolating $\Omega \to 0$, the γ_{bc} can be obtained. As is evident in equation 5.2, the second term has a sinusoidal dependency on Δ_R, which accounts for the non-adiabatic detuning in the frequency of the CF.

Using cylindrical magnetic shielding and a heat gun, after obtaining the minimum linewidth of EIT, we abruptly turned off the CF and observed the resulting oscillations. Figure 5.8 shows the underdamped oscillations that we experimentally observed in our setup.

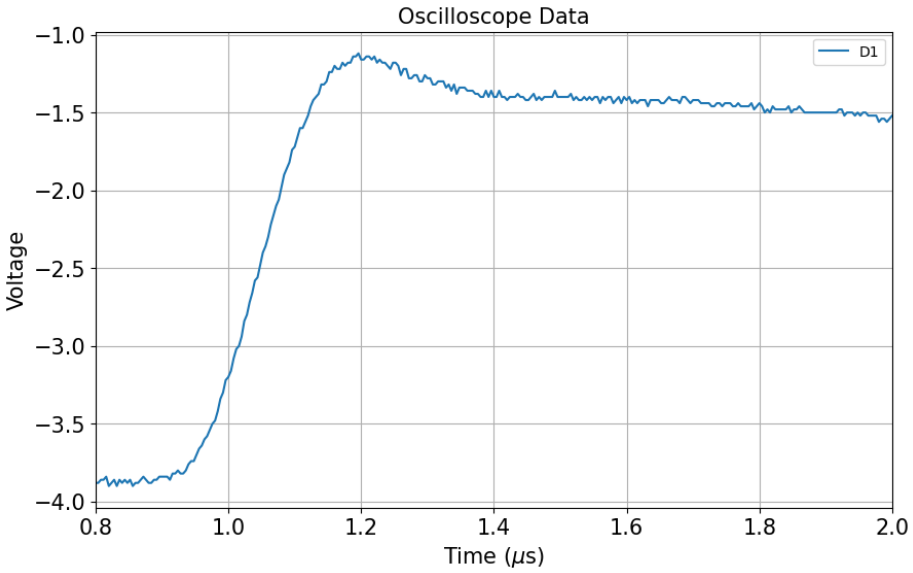

Figure 5.8: Underdamped oscillation of transient EIT when turning off the CF.

One of the reasons we could not observe clear oscillations in the absorbed field—indicative of interference between the dark and bright states—may be the lack of proper magnetic shielding. Even a small stray MF can significantly increase the decoherence in the GS coherence of the Λ-scheme.

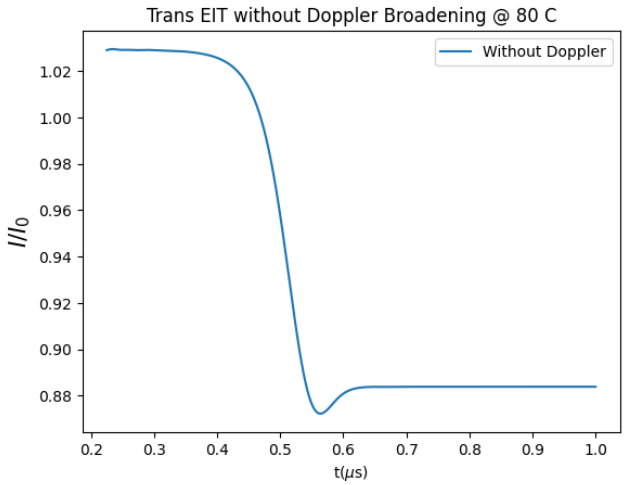

Figure 5.9: Simulated underdamped oscillation of transient EIT.

After all, it is not surprising that EIT is one of the most sensitive magnetometers [64]. Based on our simulation results, γ_{bc} in our experiment is estimated to be on the order of $2.5 \times 2\pi$ MHz. The simulation result with this value for the decoherence of the GS is shown in Figure 5.9.

Chapter 6

Unexpected pivot - Construction of Magneto-Optical Trap

Our motivation behind pursuing the construction of a MOT is twofold. First, we aim to create a less noisy AE compared to thermal vapor, and second, the MOT offers no upper bound on achievable OD, which makes it a particularly interesting system for studying various quantum phenomena, such as QM and the generation of quantum light.

Halfway through my study (at the beginning of the second year), we began discussing potential challenges in observing meaningful results for transient EIT (and the control-phase gate, which was originally my first project). Both projects had a common issue: DB had a significantly detrimental effect on the desired behavior. With that in mind, we began to consider alternative methods for conducting the experiments. Naively, one might think of stopping the atoms' motion to reduce Doppler shifts. From a technical standpoint, trapping the atoms and creating a cloud of Rb atoms using a MOT seemed like a promising solution.

To move forward, we faced two options. The first was to purchase a commercial MOT and focus solely on the experiments. However, this was not feasible due to insufficient funds. Additionally, we would need to purchase other equipment such as EOM, AOM, diode lasers, etalons, drivers, and more. The second option was to look for surplus vacuum gear from the Triumph Lab at UVic and borrow equipment from nearby labs to assemble a functional MOT from scratch. Moreover, we had to acquire all the technical skills required for building an UHV system since none of our group members had experience with UHVs before. While I had some experience

with the simulation of CAs, this was a completely different challenge in a real-world experiment.

To be fair, our timeline was highly unrealistic given all the unknowns and the limited time remaining for my study at that point (approximately 8 months of "somewhat" uninterrupted research, plus 4 months of a mandatory internship in a quantum company as part of my NSERC CREATE program). Not to mention, I still had courses to take and workshops to participate in, also part of my NSERC CREATE program. Despite these constraints, we achieved a major goal: constructing three MOTs from scratch and observing fluorescence. We built three MOTs, not just because we could and our neighbors were generous enough to bestow upon us their invaluable resources! Rather, it was due to necessity. The first MOT ran out of Rb getters (burnt out), the second was wrecked due to a breakage in the vacuum chamber, and the third (and hopefully final) version is still functioning. In the following section, I will explain the theory behind atom trapping using a MOT, then provide the technical details of building a MOT from scratch. Finally, I will recount the setbacks we experienced with the MOT breakages in our lab and how we quickly adapted and moved forward (adopting the lean-startup mindset from the book "The Lean Startup" by Eric Ries; highly recommended).

6.0.1 A brief theory of MOT

To understand the operation of a MOT, some basic principles of ALI and how this interaction leads to trapping atoms with light are covered in this section. This theory will not be comprehensive by any means, so please refer to [65] for more details.

For simplicity, we consider a basic two-level system. In this system, assuming the atoms have zero velocity, they scatter light at a rate Γ_{scat} given by the following:

$$\Gamma_{scat} = \frac{\Gamma}{2}\left(\frac{2(\Omega/\Gamma)^2}{1 + 2(\Omega/\Gamma)^2 + (2\Delta/\Gamma)^2}\right), \tag{6.1}$$

where Γ is the natural linewidth of the transition, Ω is the RBF, and Δ is the one-photon detuning of the laser frequency from the atomic resonance frequency ω_0. Since photons carry momentum $\hbar k$, the average radiation pressure force on the atoms over many scattering events is described as:

$$F = \hbar k \Gamma_{scat}. \tag{6.2}$$

Now, considering atoms are moving with velocity v, the frequency of the laser will differ from that observed in the stationary lab frame. If we work in the frame of a moving atom, this detuning to first order is given by:

$$\Delta' = \Delta - k \cdot v, \tag{6.3}$$

where Δ' is the observed detuning in the moving frame, Δ is the detuning in the stationary frame, k is the wavevector of the laser, and v is the velocity of the atom.

The Doppler effect can actually help us cool down the atoms. Assume an atom is moving in one dimension in the presence of two counter-propagating laser beams with equal frequencies. The net radiation pressure on the atom from these two beams is:

$$F = F_1 + F_2 = \hbar k \frac{\Omega^2}{\Gamma} \left(\frac{1}{1 + 2(\Omega/\Gamma)^2 + \left(\frac{2\Delta'}{\Gamma}\right)^2} - \frac{1}{1 + 2(\Omega/\Gamma)^2 + \left(\frac{2\Delta'}{\Gamma}\right)^2} \right). \tag{6.4}$$

If we expand this equation to first order in velocity, we obtain $F = -\beta v$, where $\beta > 0$ means the radiation pressure exerts a damping force on the atomic velocity. Atoms are subject to Doppler cooling along all three dimensions in a MOT.

Considering that the Rb getters spew atoms while being heated by an applied voltage, the velocity distribution of Rb atoms in the vacuum chamber can be described by the MBD:

$$P(v) \propto v^2 e^{-mv^2/(k_B T)}, \tag{6.5}$$

where k_B is the Boltzmann constant, T is the temperature of the atom in Kelvin, and v is the speed of the atoms. Given that the getters are heated to at least 150°C, most Rb atoms are moving too fast to be slowed down in the MOT. However, atoms in the low-velocity tail of the probability distribution can be captured.

Unsurprisingly, this low velocity is referred to as the *capture velocity* and can be estimated as:

$$v_c \simeq \sqrt{\frac{2F_{\max}D}{m}}, \tag{6.6}$$

where D is the diameter of the trapping optical beam, and $F_{\max}$ is the maximum radiation pressure. From equation 6.6, it is evident that the larger the beam diameter, the more velocity sub-classes can be captured.

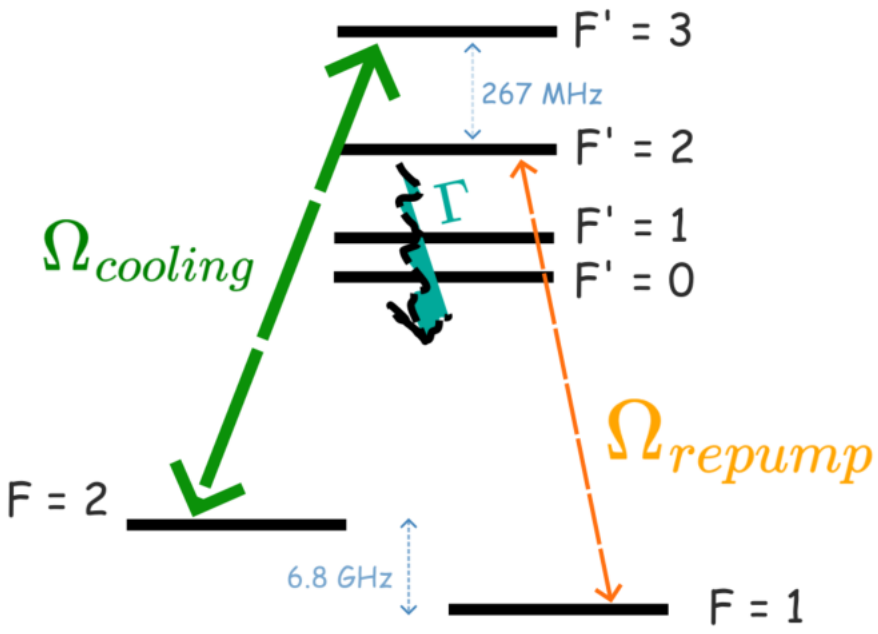

Figure 6.1: HF levels for the ^{87}Rb $5S_{1/2}$ GS (HF spin quantum number F) and $5P_{3/2}$ excited state (HF spin quantum number F') are shown. The relevant energy differences are displayed in frequency units. The transitions used for cooling and repump light are indicated.

In an ideal scenario, atoms could be cooled down to zero temperature. However, due to the damping force from Doppler cooling and force fluctuations, achieving absolute zero temperature is a real challenge. These force fluctuations arise from the random nature of absorption and spontaneous emission events, as well as from the random orientation of the emitted photons. These random fluctuations cause atoms to undergo a random walk in momentum space, where their momentum variance increases as follows:

$$\frac{d}{dt}(p^2) = A\Gamma_{\text{scat}}\hbar k, \tag{6.7}$$

where the prefactor A accounts for the force fluctuations and is on the order of unity. The effects of damping and momentum diffusion can be characterized by the Doppler temperature:

$$T_D = \frac{\langle p^2 \rangle}{2k_B m}. \tag{6.8}$$

This diffusion explains why optical molasses spreads outwards over time.

The transitions used for cooling and repumping atoms in ^{87}Rb are illustrated in

Fig. 6.1.

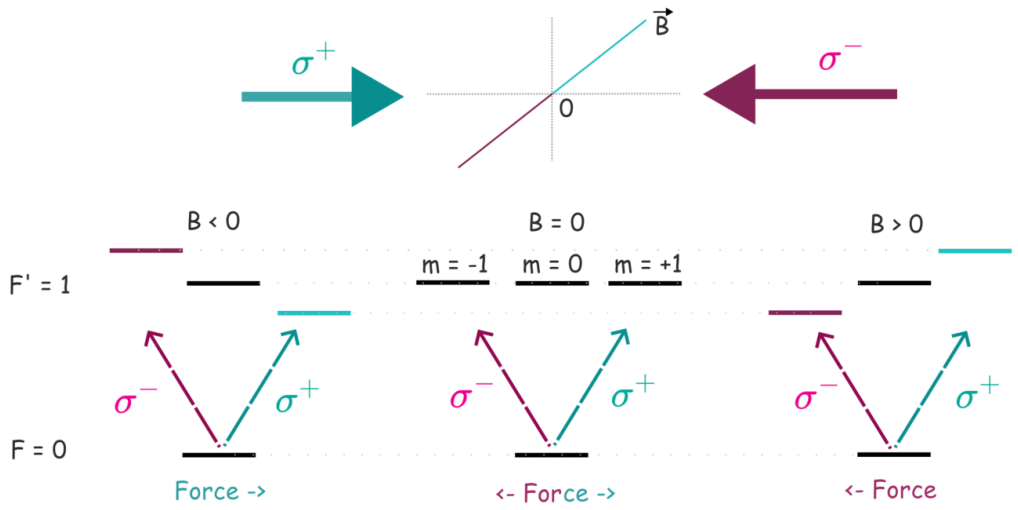

Figure 6.2: Illustrative one-dimensional representation of a MOT with a simple 2-level atom. The GS (in this case, F = 0) does not experience ZS. The excited state F' = 1 splits into three Zeeman sublevels $m = \pm 1$ and $m = 0$ in the presence of a MF. The atoms are subjected to a left-circularly polarized beam from the right and a right-circularly polarized beam from the left. The arrows represent the absorption of a detuned photon, following the selection rules imposed by the handedness of the polarization.

For laser cooling, we drive atoms from the $F = 2$ GS to the $F' = 3$ excited state of the D_2 line. To compensate for atoms decaying from excited states $F' = 2$ and $F' = 1$ to the $F = 1$ GS, we introduce another laser to repump atoms to the $F' = 2$ excited state. This ensures that they decay back to the $F = 2$ GS, where they can be further cooled by the cooling laser.

Each of the $F = 2$ and $F' = 3$ levels contains several magnetic sublevels, and the strengths of the transitions between them are related by the Clebsch-Gordan coefficients [29]. Circularly polarized light driving the $|\mathrm{F} = 2, \mathrm{m_F} = 2\rangle \rightarrow |\mathrm{F}' = 3, \mathrm{m_F} = 3\rangle$ transition has the strongest coupling, corresponding to the lowest saturation intensity.

As described in the theory chapter 2, in the presence of a MF, the sublevels of both the GS and the excited state are shifted by the linear Zeeman effect according to $\Delta E = g_F \mu_B m_F B$. These Zeeman shifts are important because they make the radiation pressure force in a MOT position-dependent, as the Zeeman shifts change the atomic resonance frequencies across space. To illustrate this, assume an atom moves in the direction where it experiences a positive MF, as depicted in Fig. 6.2.

This atom is more likely to undergo a transition corresponding to the absorption of a σ^- photon, as the right-circularly polarized beam is Doppler-shifted up in frequency. Conversely, atoms moving in the direction where they experience a negative MF will more likely absorb σ^+ photons. For stationary atoms, both right- and left-circularly polarized light are absorbed equally, causing them to remain in the zero-field region of the trap.

In our setup, we apply gradient MFs along all three dimensions by creating a spherical quadrupole field as follows:

$$\mathbf{B} = Bz\hat{z} - \frac{B}{2}(x\hat{x} + y\hat{y}). \tag{6.9}$$

Another cooling mechanism involved in the procedure, known as polarization-gradient cooling, leads to sub-Doppler cooling. This cooling mechanism is based on the Stark shift and optical pumping [65], where optical pumping consistently directs the atoms into an internal atomic state in which the AC Stark energy is minimized.

6.0.2 Construction of UHV system

To obtain a high-quality cloud of atoms in a MOT, it is necessary to operate UHV conditions, typically at or below 5×10^{-8} Torr. Maintaining such a vacuum requires careful consideration of outgassing, as even small amounts of contaminants can degrade the vacuum, particularly since many substances have boiling points below room temperature at these pressures. This section discusses the UHV system components and the methods employed to minimize outgassing.

Since there is no "one-size-fits-all" solution in vacuum technology, a single vacuum pump cannot span the pressure range from atmospheric pressure down to UHV. Therefore, a multi-stage pumping approach is employed, using a roughing pump, a turbomolecular pump (backed by a roughing pump), and an ion-pump. For effective sealing between components, 2.75-inch ConFlat flanges are used throughout the system. These types of flanges are connected with copper gaskets between them and fastened using bolts and nuts. The quality of the MOT depends on the quality of the gaskets used, as different gaskets handle specific temperatures, which should be considered during the Bakeout (BO) procedure.

The roughing pumps used in the system are Alcatel 2002BB rotary vane pumps, which work by trapping gas in rotating chambers and expelling it through an exhaust,

reducing the pressure from atmospheric levels down to 2.25×10^{-3} Torr. Following this, a Pfeiffer turbomolecular pump is used, managed by a TCP 120 controller. This pump relies on rapidly spinning rotors to eject particles from the vacuum System (VS). Operating at atmospheric pressure would be detrimental to the blades due to air density, so the turbomolecular pump requires the system pressure to be reduced to 10^{-3} mbar or lower before it can start, which is achieved by using a roughing pump to back the turbopump.

The third stage of pumping is handled by a VacIon 20 L/s StarCell ion getter pump [the name of the second ion-pump used in the second version of our MOT is not recalled], which is powered by a StarCell control unit. This pump ionizes residual gas particles using a titanium getter, enabling it to operate at pressures up to 10^{-5} Torr and reach UHV levels, with an ultimate pressure around 10^{-11} Torr.

Just as specific pumps are required for different pressure ranges, different vacuum gauges are used to measure pressures across the system. The first type of gauge used in the system is the Edwards Pirani gauge, which operates by measuring the thermal conductivity of the gas to estimate the pressure. This gauge is suitable for readings from atmospheric pressure down to 10^{-3} Torr. For lower pressures, we rely on an MKS Granville-Phillips 274 Bayard-Alpert ionization gauge, connected to a Granville Phillips 307 controller. This device ionizes gas molecules and determines the pressure based on the resulting ion current, with a measurement range from 10^{-1} to 10^{-10} Torr. Additionally, the ion-pump itself serves as a reliable gauge, as there is a one-to-one relationship between the current drawn by the ion-pump and the pressure of the vacuum chamber. For one of our ion-pumps (the one that was damaged), I created a plot to deduce the pressure of the vacuum chamber based on the voltage readout from the ion-pump's whiskers, as shown in Figure 6.3.

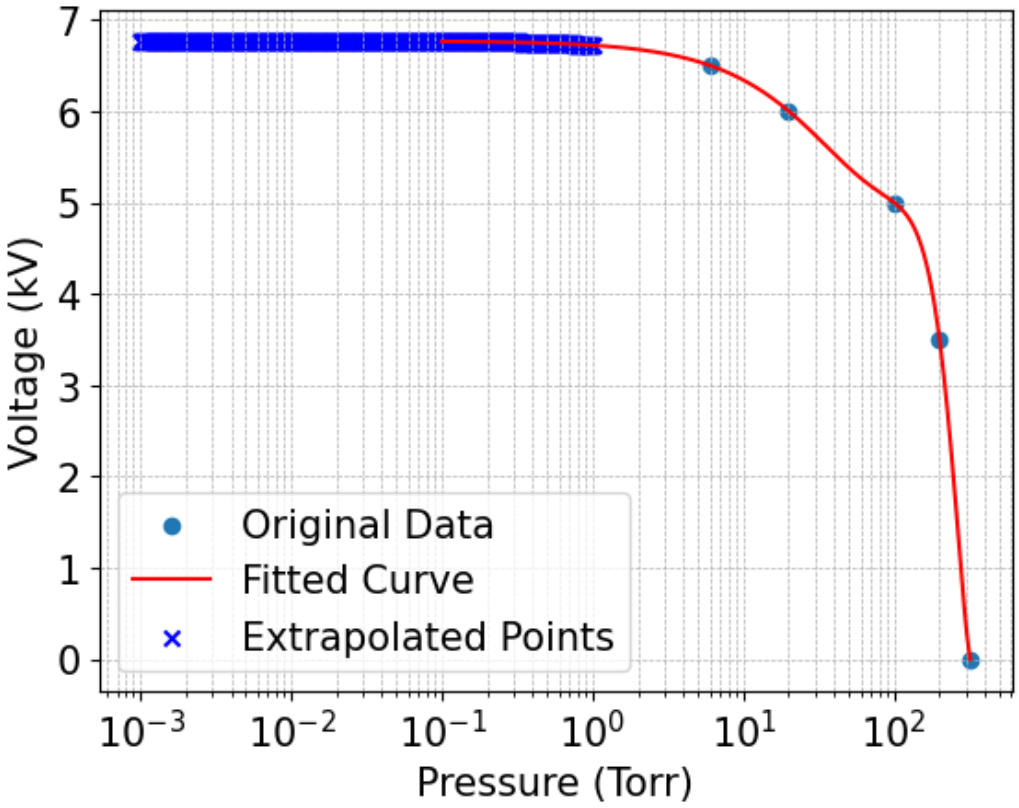

Figure 6.3: Deducing pressure of the vacuum chamber by voltage readout of the ion-pump.

In the MOT setup, glass components are essential for laser transmission. To meet this need, we utilize a 1.50-inch diameter, domed Pyrex 7740 glass-to-stainless steel adapter, sourced from Accu-Glass Products. This component can withstand a maximum temperature of 400°C and maintain a vacuum down to 10^{-10} Torr. The glass-to-metal seal has a thermal tolerance, allowing only 10°C per minute of temperature change before risking degradation.

Rb atoms are required in the system to form the atomic cloud in the MOT. These atoms are introduced via SAES Rb getters, which release Rb when heated between 550°C and 850°C. Heating is achieved by applying a minimum of 5.3A of current through the getter. The getters are attached to an electrical Feedthrough (FT) to allow installation into the vacuum chamber and to apply the necessary voltage.

For detailed information on the cleaning procedure and assembly of the MOT, refer to Appendix D.

6.0.3 Breakages!

During the course of this project, the VS had to be vented multiple times. Initially, only a single getter was installed (due to lack of experience and maybe ignorance!), which eventually burnt out, likely due to excessive current flow. This required breaking the vacuum to replace the damaged getter. To prevent similar issues in the future, we decided to install two pairs of getters. By placing two getters in series, the overall resistance increases, reducing the risk of current overload. Additionally, the second pair provides redundancy, ensuring that the system remains functional if one pair fails.

The VS was breached again following the BO process when the bellows connecting the MOT chamber to the roughing system unintentionally fell down, causing the glass tube to shatter. Subsequently, the sudden loss of vacuum damaged the ion-pump. Although it was a true disaster, we took the opportunity to upgrade the system based on the lessons learned. We purchased a new glass tube that is rectangular instead of circular since the round glass tube may have contributed to other problems. The circular shape acted as a thick lens with varying radii of curvature on the inner and outer surfaces, likely introducing distortions in the trapping beams and causing uneven trapping power. A rectangular glass tube reduces optical distortion and improves system performance.

Additionally, we borrowed a bigger and stronger ion-pump from a nearby lab, which allowed us to achieve a vacuum pressure in the MOT system of 3×10^{-9} Torr after the final BO. This was quite remarkable and a first of its kind at UVic!

Chapter 7

Conclusion

In conclusion, this thesis advances the understanding of EIT in VCs, addressing critical aspects for its application in emerging quantum technologies. While previous studies have focused on idealized three-level systems, real-world laboratory conditions—particularly in Rb AEs with complex level structures and DB—pose unique challenges that demand further investigation. Through comprehensive numerical simulations, we explored how DB, deviations from a simple Lambda configuration, ground-state dephasing, and population exchange influence transient EIT response. This approach highlighted the nuanced interplay between ground-state coherence and transparency depth, offering valuable insights for setting up realistic EIT systems. Additionally, the experimental setup designed and constructed as part of this work allowed us to obtain preliminary results on transient EIT in laboratory conditions, with findings that complement theoretical predictions and underscore the importance of practical considerations in decoherence and population dynamics.

The construction of a MOT further enabled the controlled cooling of Rb atoms, providing a pathway to study EIT in cold AEs with minimized Doppler effects. This experimental apparatus, assembled from the ground up with custom-built electronics, mechanical parts, and an UHV environment, underscores the practical challenges and solutions involved in achieving stable and precise quantum optical experiments.

By bridging theory with hands-on experimentation, this thesis not only clarifies the dependencies and sensitivities of EIT in realistic conditions but also lays the groundwork for more complex studies, including QM implementations in cold atomic clouds. Future research can leverage these findings to enhance the robustness and scalability of EIT-based technologies, potentially leading to breakthroughs in high-throughput quantum information processing and precision measurement applications.

Bibliography

[1] Michael A. Nielsen and Isaac L. Chuang. *Quantum Computation and Quantum Information*. Cambridge University Press, 2010.

[2] Ashley Montanaro. Quantum algorithms: an overview. *npj Quantum Information*, 2:1–8, 2016.

[3] Richard P. Feynman. Quantum mechanical computers. *Foundations of Physics*, 16(6):507–532, 1986.

[4] Rami Barends, Julian Kelly, Anthony Megrant, Andrzej Veitia, Daniel Sank, Evan Jeffrey, Ted C. White, Josh Mutus, Austin G. Fowler, Brooks Campbell, et al. Superconducting quantum circuits at the surface code threshold for fault tolerance. *Nature*, 508(7497):500–503, 2014.

[5] Joseph A. Schreier, Andrew A. Houck, Jens Koch, David I. Schuster, Bradley R. Johnson, Jerry M. Chow, Jay M. Gambetta, J. Majer, Luigi Frunzio, Michel H. Devoret, et al. Suppressing charge noise decoherence in superconducting charge qubits. *Physical Review B*, 77(18):180502, 2008.

[6] J. Eli Bourassa, Rafael N. Alexander, Michael Vasmer, Ashlesha Patil, Ilan Tzitrin, Takaya Matsuura, Daiqin Su, Ben Q. Baragiola, Saikat Guha, Guillaume Dauphinais, et al. Blueprint for a scalable photonic fault-tolerant quantum computer. *Quantum*, 5:392, 2021.

[7] Stephanie Simmons. Scalable fault-tolerant quantum technologies with silicon color centers. *PRX Quantum*, 5(1):010102, 2024.

[8] Jan Balewski, Milan Kornjaca, Katherine Klymko, Siva Darbha, Mark R. Hirsbrunner, Pedro Lopes, Fangli Liu, and Daan Camps. Engineering quantum states with neutral atoms. *arXiv preprint arXiv:2404.04411*, 2024.

[9] Hoi-Kwong Lo, Marcos Curty, and Bing Qi. Measurement-device-independent quantum key distribution. *Physical Review Letters*, 108(13):130503, 2012.

[10] Vittorio Giovannetti, Seth Lloyd, and Lorenzo Maccone. Quantum metrology. *Physical Review Letters*, 96(1):010401, 2006.

[11] Nicholas Peters, Joseph Altepeter, Evan Jeffrey, David Branning, and Paul Kwiat. Precise creation, characterization, and manipulation of single optical qubits. *arXiv preprint quant-ph/0502177*, 2005.

[12] David P. DiVincenzo. The physical implementation of quantum computation. *Fortschritte der Physik: Progress of Physics*, 48(9-11):771–783, 2000.

[13] Rico Gutzler, Manish Garg, Christian R. Ast, Klaus Kuhnke, and Klaus Kern. Light–matter interaction at atomic scales. *Nature Reviews Physics*, 3(6):441–453, 2021.

[14] K.-J. Boller, A. Imamoğlu, and Stephen E. Harris. Observation of electromagnetically induced transparency. *Physical Review Letters*, 66(20):2593, 1991.

[15] Ofer Firstenberg, Charles S. Adams, and Sebastian Hofferberth. Nonlinear quantum optics mediated by rydberg interactions. *Journal of Physics B: Atomic, Molecular and Optical Physics*, 49(15):152003, 2016.

[16] Yang Wang, Alexander N. Craddock, Rourke Sekelsky, Mael Flament, and Mehdi Namazi. Field-deployable quantum memory for quantum networking. *Physical Review Applied*, 18(4):044058, 2022.

[17] David H. Meyer, Christopher O'Brien, Donald P. Fahey, Kevin C. Cox, and Paul D. Kunz. Optimal atomic quantum sensing using electromagnetically-induced-transparency readout. *Physical Review A*, 104(4):043103, 2021.

[18] Lene Vestergaard Hau, Stephen E. Harris, Zachary Dutton, and Cyrus H. Behroozi. Light speed reduction to 17 metres per second in an ultracold atomic gas. *Nature*, 397(6720):594–598, 1999.

[19] Muhammad Amin, Rashad Ramzan, and Omar Siddiqui. Slow wave applications of electromagnetically induced transparency in microstrip resonator. *Scientific Reports*, 8(1):2357, 2018.

[20] Zheng-Feng Hu, Chun-Guang Du, Jian-Liao Deng, and Yu-Zhu Wang. Transient responses of transparency in a far-off resonant atomic system. *Chinese Physics B*, 23(5):054204, 2014.

[21] H. X. Chen, A. V. Durrant, J. P. Marangos, and J. A. Vaccaro. Observation of transient electromagnetically induced transparency in a rubidium λ system. *Physical Review A*, 58(2):1545, 1998.

[22] P. Valente, H. Failache, and A. Lezama. Comparative study of the transient evolution of hanle electromagnetically induced transparency and absorption resonances. *Physical Review A*, 65(2):023814, 2002.

[23] A. Mair, J. Hager, D. F. Phillips, R. L. Walsworth, and M. D. Lukin. Phase coherence and control of stored photonic information. *Physical Review A*, 65(3):031802, 2002.

[24] Ran Finkelstein, Samir Bali, Ofer Firstenberg, and Irina Novikova. A practical guide to electromagnetically induced transparency in atomic vapor. *New Journal of Physics*, 25(3):035001, 2023.

[25] Michael Fleischhauer, Atac Imamoglu, and Jonathan P. Marangos. Electromagnetically induced transparency: Optics in coherent media. *Reviews of Modern Physics*, 77(2):633–673, 2005.

[26] Michael Fleischhauer and Mikhail D. Lukin. Dark-state polaritons in electromagnetically induced transparency. *Physical Review Letters*, 84(22):5094, 2000.

[27] Claude Cohen-Tannoudji, Jacques Dupont-Roc, and Gilbert Grynberg. *Atom-photon interactions: basic processes and applications*. John Wiley & Sons, 1998.

[28] Marlan O. Scully and M. Suhail Zubairy. *Quantum Optics*. Cambridge University Press, 1997.

[29] Paul Siddons, Charles S. Adams, Chang Ge, and Ifan G. Hughes. Absolute absorption on rubidium d lines: comparison between theory and experiment. *Journal of Physics B: Atomic, Molecular and Optical Physics*, 41(15):155004, 2008.

[30] Daniel A. Steck. Rubidium 87 d line data. `http://steck.us/alkalidata`, 2001. Accessed: 2024-10-31.

[31] Valerio Lucarini, Jarkko J Saarinen, Kai-Erik Peiponen, and Erik M Vartiainen. *Kramers-Kronig relations in optical materials research*, volume 110. Springer Science & Business Media, 2005.

[32] Herch Moyses Nussenzveig. Causality and dispersion relations for fixed momentum transfer. *Physica*, 26(4):209–229, 1960.

[33] John S Toll. Causality and the dispersion relation: logical foundations. *Physical Review*, 104(6):1760, 1956.

[34] Rodney Loudon. *The Quantum Theory of Light*. OUP Oxford, 2000.

[35] E Figueroa, F Vewinger, J Appel, and A I Lvovsky. Decoherence of electromagnetically induced transparency in atomic vapor. *Optics Letters*, 31(17):2625–2627, 2006.

[36] M Gorris-Neveux, P Monnot, M Fichet, M Ducloy, R Barbé, and J C Keller. Doppler-free reflection spectroscopy of rubidium d1 line in optically dense vapour. *Optics Communications*, 134(1-6):85–90, 1997.

[37] Ofer Firstenberg, M Shuker, Rami Pugatch, D R Fredkin, Nir Davidson, and A Ron. Theory of thermal motion in electromagnetically induced transparency: Effects of diffusion, doppler broadening, and dicke and ramsey narrowing. *Physical Review A*, 77(4):043830, 2008.

[38] Anil K Patnaik, Paul S Hsu, Girish S Agarwal, George R Welch, and Marlan O Scully. Measurement of ground-state decoherence via interruption of coherent population trapping. *Physical Review A*, 75(2):023807, 2007.

[39] William Happer. Optical pumping. *Reviews of Modern Physics*, 44(2):169, 1972.

[40] Charles B Alcock, V P Itkin, and M K Horrigan. Vapour pressure equations for the metallic elements: 298–2500k. *Canadian Metallurgical Quarterly*, 23(3):309–313, 1984.

[41] Jun John Sakurai and Jim Napolitano. *Modern Quantum Mechanics*. Cambridge University Press, 2020.

[42] David J Griffiths and Darrell F Schroeter. *Introduction to Quantum Mechanics*. Cambridge University Press, 2018.

[43] OS Mishina, M Scherman, P Lombardi, J Ortalo, D Felinto, AS Sheremet, A Bramati, DV Kupriyanov, J Laurat, and E Giacobino. Electromagnetically induced transparency in an inhomogeneously broadened λ transition with multiple excited levels. *Physical Review A—Atomic, Molecular, and Optical Physics*, 83(5):053809, 2011.

[44] J Cviklinski, J Ortalo, J Laurat, A Bramati, M Pinard, and E Giacobino. Reversible quantum interface for tunable single-sideband modulation. *Physical Review Letters*, 101(13):133601, 2008.

[45] Shrabana Chakrabarti, Amitkiran Pradhan, Biswajit Ray, and Pradip N. Ghosh. Velocity selective optical pumping effects and electromagnetically induced transparency for d2 transitions in rubidium. *Journal of Physics B: Atomic, Molecular and Optical Physics*, 38(23):4321, 2005.

[46] AM Akulshin, S Barreiro, and A Lezama. Electromagnetically induced absorption and transparency due to resonant two-field excitation of quasidegenerate levels in rb vapor. *Physical Review A*, 57(4):2996, 1998.

[47] Ke Li, Lu Deng, and MG Payne. Realization of a single and closed λ-system in a room-temperature three-level coherently prepared resonant medium with narrow d1 hyperfine splittings. *Applied Physics Letters*, 95(22), 2009.

[48] Saesun Kim and Alberto M. Marino. Effect of closely-spaced excited states on electromagnetically induced transparency. *OSA Continuum*, 4(12):3184–3203, 2021.

[49] Alan Corney. *Atomic and Laser Spectroscopy*. Clarendon Press Oxford, 1978.

[50] M L Citron, H R Gray, C W Gabel, and C R Stroud Jr. Experimental study of power broadening in a two-level atom. *Physical Review A*, 16(4):1507, 1977.

[51] H. Schmidt and A. Imamoglu. Giant kerr nonlinearities obtained by electromagnetically induced transparency. *Optics Letters*, 21(23):1936–1938, 1996.

[52] J Robert Johansson, Paul D Nation, and Franco Nori. Qutip: An open-source python framework for the dynamics of open quantum systems. *Computer Physics Communications*, 183(8):1760–1772, 2012.

[53] Frans Eduard van Dorsselaer and G Nienhuis. Quantum trajectories. *Journal of Optics B: Quantum and Semiclassical Optics*, 2(4):R25, 2000.

[54] Vadim Makarov. Controlling passively quenched single photon detectors by bright light. *New Journal of Physics*, 11(6):065003, 2009.

[55] Lars Lydersen, Carlos Wiechers, Christoffer Wittmann, Dominique Elser, Johannes Skaar, and Vadim Makarov. Hacking commercial quantum cryptography systems by tailored bright illumination. *Nature Photonics*, 4(10):686–689, 2010.

[56] Ilja Gerhardt, Qin Liu, Antía Lamas-Linares, Johannes Skaar, Christian Kurtsiefer, and Vadim Makarov. Full-field implementation of a perfect eavesdropper on a quantum cryptography system. *Nature Communications*, 2(1):349, 2011.

[57] Leonardo Ricci, Matthias Weidemüller, Tilman Esslinger, Andreas Hemmerich, Claus Zimmermann, Vladan Vuletic, Wolfgang König, and Theodor W Hänsch. A compact grating-stabilized diode laser system for atomic physics. *Optics Communications*, 117(5-6):541–549, 1995.

[58] Jürgen Appel, Andrew MacRae, and Alexander I. Lvovsky. A versatile digital ghz phase lock for external cavity diode lasers. *Measurement Science and Technology*, 20(5):055302, 2009.

[59] Kristan L. Corwin, Zheng-Tian Lu, Carter F. Hand, Ryan J. Epstein, and Carl E. Wieman. Frequency-stabilized diode laser with the zeeman shift in an atomic vapor. *Applied Optics*, 37(15):3295–3298, 1998.

[60] Sung Jong Park, Hyuck Cho, Taeg Yong Kwon, and Ho Seong Lee. Transient coherence oscillation induced by a detuned raman field in a rubidium λ system. *Physical Review A*, 69(2):023806, 2004.

[61] Z. F. Hu, C. G. Du, and Y. Z. Wang. Buffer-gas-induced narrowing of electromagnetically induced transparent spectra for an open system. *Journal of Modern Optics*, 53(4):513–523, 2006.

[62] Mason Klein, M. Hohensee, D. F. Phillips, and R. L. Walsworth. Electromagnetically induced transparency in paraffin-coated vapor cells. *Physical Review A*, 83(1):013826, 2011.

[63] Jiao Geng, G. T. Campbell, Julien Bernu, D. B. Higginbottom, B. M. Sparkes, S. M. Assad, W. P. Zhang, N. P. Robins, Ping Koy Lam, and B. C. Buchler. Electromagnetically induced transparency and four-wave mixing in a cold atomic ensemble with large optical depth. *New Journal of Physics*, 16(11):113053, 2014.

[64] V. I. Yudin, A. V. Taichenachev, Y. O. Dudin, V. L. Velichansky, A. S. Zibrov, and S. A. Zibrov. Vector magnetometry based on electromagnetically induced transparency in linearly polarized light. *Physical Review A*, 82(3):033807, 2010.

[65] Harold J. Metcalf and Peter Van der Straten. *Laser Cooling and Trapping*. Springer Science & Business Media, 1999.

[66] David Maurice Brink and George Raymond Satchler. *Angular momentum*. Oxford University Press, 1994.

Appendix A

Derivation of the susceptibility for 3-level Λ system

In a three-level Λ system, when we couple a WP beam ($|\Omega_{31}|^2 \approx 0$) to $|1\rangle \longrightarrow |3\rangle$ and couple a strong beam to $|2\rangle \longrightarrow |3\rangle$, the perturbed H after the RWA can be written as:

$$H(t) = -\hbar/2 \begin{pmatrix} 0 & 0 & \Omega_{31}^* \\ 0 & 2\delta & \Omega_{32}^* \\ \Omega_{31} & \Omega_{32} & 2\Delta \end{pmatrix} \tag{A.1}$$

By evolving the DM over time using the perturbed H, one can write the optical Bloch equations as:

$$\begin{aligned} \dot{\hat{\rho}} &= -\frac{i}{\hbar}[\hat{H}, \hat{\rho}] + \hat{\mathcal{L}}(\hat{\rho}), \\ \dot{\rho}_{31} &= \frac{i}{2}[\Omega_{31}^*\rho_{11} - \Omega_{31}^*\rho_{33} + \Omega_{32}^*\rho_{21} + 2\Delta\rho_{31}] - \frac{\Gamma_1}{2}\rho_{31}, \\ \dot{\rho}_{21} &= \frac{i}{2}[\Omega_{32}\rho_{31} - \Omega_{31}^*\rho_{23} + 2\delta\rho_{12}] - \frac{\gamma}{2}\rho_{21}, \\ \dot{\rho}_{32} &= \frac{i}{2}[\Omega_{31}^*\rho_{12} + \Omega_{32}^*\rho_{22} - \Omega_{32}^*\rho_{33} + 2\Delta\rho_{32} - 2\delta\rho_{32}] - \frac{\Gamma_2}{2}\rho_{32}. \end{aligned} \tag{A.2}$$

We assume that $\Gamma_1 = \Gamma_2 = \Gamma$ for simplicity. To solve the coupled DEs, we assume that the majority of the atomic population exists in the GS such that $\rho_{11} = 1$, and $\rho_{22} = \rho_{33} = 0$. Under these assumptions, we solve for ρ_{32}:

$$\rho_{32} = \rho_{23}^* = \frac{-\frac{i}{2}\Omega_{31}^*\rho_{12}}{i(\Delta - \delta) - \Gamma/2} \tag{A.3}$$

Solving for ρ_{21} yields:

$$\rho_{21} = \frac{-\frac{i}{2}[\Omega_{32}\rho_{31} - \Omega_{31}^{*}\rho_{23}]}{i\delta - \gamma/2} \tag{A.4}$$

Substituting equation A.3 into the above expression leads to:

$$\rho_{21} = \frac{-\frac{i}{2}\Omega_{32}\rho_{31} + \frac{\frac{i}{2}|\Omega_{31}|^2\rho_{21}}{-i(\Delta-\delta)-\Gamma/2}}{i\delta - \gamma/2} \tag{A.5}$$

Leveraging the WP field simplifies the expression:

$$\rho_{21} = \rho_{12}^{*} = \frac{-\frac{i}{2}\Omega_{32}\rho_{31}}{i\delta - \gamma/2} \tag{A.6}$$

Solving for ρ_{31} gives:

$$\rho_{31} = \frac{-\frac{i}{2}[\Omega_{31}^{*} + \Omega_{32}^{*}\rho_{21}]}{i\Delta - \frac{\Gamma}{2}} \tag{A.7}$$

Substituting equation A.6 into this, we get:

$$\rho_{31} = \frac{-\frac{i}{2}[\Omega_{31}^{*} + \Omega_{32}^{*}(\frac{-\frac{i}{2}\Omega_{32}\rho_{31}}{i\delta-\gamma/2})]}{i\Delta - \frac{\Gamma}{2}} \tag{A.8}$$

Simplifying further:

$$\rho_{31} = \rho_{13}^{*} = \frac{-\frac{i}{2}\Omega_{31}^{*}(i\delta - \gamma/2)}{\frac{1}{4}|\Omega_{32}|^2 + (i\Delta - \frac{\Gamma}{2})(i\delta - \gamma/2)} \tag{A.9}$$

Finally, this leads to the susceptibility expression:

$$\chi(\Delta) = \frac{nD_{ij}^2}{\epsilon_0\hbar}\frac{i\gamma/2 + \delta}{1/2|\Omega_{32}|^2 + 2(i\Delta - \Gamma/2)(i\delta - \gamma/2)} \tag{A.10}$$

Appendix B

Deriving H for 6-level AE, D_2 line

The AE consists of six ESs $|n\rangle$, where n is an integer from 1 to 6, corresponding to EV energies $\hbar\omega_n$. The labeling of the states follows the order of increasing energy, where the lowest energy state is $|1\rangle$ and the highest is $|6\rangle$. We write the total H in the form $H_T = H_0 + H_I$, where H_0 describes the free atom without external fields, and H_I is the perturbation due to the applied EF. The H, H_0 and its eigenvectors account for all the interactions between the nucleus and the electron.

We begin by writing the unperturbed H (dropping the hat for simplicity) for the six-level system using eigenvectors and EVs:

$$H_0 = \left(\sum_n |n\rangle\langle n|\right) H \left(\sum_n |n\rangle\langle n|\right) = \begin{pmatrix} \hbar\omega_1 & 0 & 0 & 0 & 0 & 0 \\ 0 & \hbar\omega_2 & 0 & 0 & 0 & 0 \\ 0 & 0 & \hbar\omega_3 & 0 & 0 & 0 \\ 0 & 0 & 0 & \hbar\omega_4 & 0 & 0 \\ 0 & 0 & 0 & 0 & \hbar\omega_5 & 0 \\ 0 & 0 & 0 & 0 & 0 & \hbar\omega_6 \end{pmatrix} \quad \text{(B.1)}$$

To make this H resemble the D_2 line of ^{87}Rb, we define the ground levels as $|1\rangle$ corresponding to F = 1, and $|2\rangle$ corresponding to F = 2. The excited states are defined as follows: $|3\rangle$ for $F' = 0$, $|4\rangle$ for $F' = 1$, $|5\rangle$ for $F' = 2$, and $|6\rangle$ for $F' = 3$.

If we perturb the system with external EFs, we couple level $|1\rangle$ with a weak field $\mathbf{E_p}$ to level $|4\rangle$, and level $|2\rangle$ is coupled to $|4\rangle$ with a strong field $\mathbf{E_c}$. Other excited states can also experience interactions with these fields as long as the dipole transition is not forbidden. Intuitively, one might expect that the coupling field will relatively shift the excited states.

The interaction H H_I due to the applied fields can be written as:

$$H_I = -\mathbf{d} \cdot \mathbf{E}, \tag{B.2}$$

where $\mathbf{d}$ is the dipole moment operator, and $\mathbf{E}$ is the EF. For our case, this includes contributions from both the PF $\mathbf{E_p}$ and the CF $\mathbf{E_c}$.

By writing out the full form of H_I and solving the coupled system of equations, we can construct the full 6-level H that accounts for the energy shifts and couplings between the levels induced by the probe and CFs. Furthermore, the transitions $|1\rangle \longrightarrow |2\rangle$, $|1\rangle \longrightarrow |6\rangle$, and $|2\rangle \longrightarrow |3\rangle$ are dipole forbidden. The applied EF can be expressed as:

$$\mathbf{E} = \mathbf{E_p} \cos(\omega_p t - \mathbf{k_p} \cdot \mathbf{r}) + \mathbf{E_c} \cos(\omega_c t - \mathbf{k_c} \cdot \mathbf{r}), \tag{B.3}$$

where $\mathbf{k_p}$ and $\mathbf{k_c}$ are the wavevectors of the probe and CFs, respectively. Since the wavelength of the EF we are using is on the order of $\lambda \sim 10^{-7}$m, which is much longer compared to the Bohr radius $a_0 \sim 10^{-10}$m, we can approximate $\lambda \gg a_0$, allowing us to drop the spatial dependency of the EF. This is known as the dipole approximation, which is typically valid for visible light.

Using the trigonometric identity, we can expand the cosine function as follows:

$$\cos(\omega_p t - \mathbf{k_p} \cdot \mathbf{r}) = \cos(\omega_p t) \cos(\mathbf{k_p} \cdot \mathbf{r}) - \sin(\omega_p t) \sin(\mathbf{k_p} \cdot \mathbf{r}), \tag{B.4}$$

and given that $\lambda \gg a_0$, it follows that $1 \gg \mathbf{k_p} \cdot \mathbf{r}$. Therefore, $\cos(\mathbf{k_p} \cdot \mathbf{r}) \approx 1$ and $\sin(\mathbf{k_p} \cdot \mathbf{r}) \approx 0$. This approximation simplifies the EF to:

$$\mathbf{E} = \mathbf{E_p} \cos(\omega_p t) + \mathbf{E_c} \cos(\omega_c t). \tag{B.5}$$

The interaction H for this perturbation, which describes the energy associated with a dipole of charge e and separation vector $\widehat{\mathbf{r}}$ in the applied field $\mathbf{E}$, can be written as:

$$H_I = -e\mathbf{E} \cdot \widehat{\mathbf{r}}. \tag{B.6}$$

The dipole moment operator can be defined as $\mathcal{D} = e\hat{r}$, and its matrix elements in the eigenbasis of H_0 are given by $\mathcal{D}_{ij} = \mathcal{D}^*{}_{ji} = \langle i|\mathcal{D}|j\rangle$.

Using this formalism, the interaction H H_I can be constructed for the specific transitions between the ground and excited states in the six-level system. The presence of the strong CF $\mathbf{E_c}$ and the WP field $\mathbf{E_p}$ will induce coupling between the

states, leading to the characteristic features of EIT or other effects depending on the parameters of the fields. The perturbation now becomes

$$H_I = -\left(\sum_n |n\rangle\langle n|\right)\mathcal{D}\left(\sum_n |n\rangle\langle n|\right)E = -E\begin{pmatrix} \mathcal{D}_{11} & \mathcal{D}_{12} & \mathcal{D}_{13} & \mathcal{D}_{14} & \mathcal{D}_{15} & \mathcal{D}_{16} \\ \mathcal{D}_{21} & \mathcal{D}_{22} & \mathcal{D}_{23} & \mathcal{D}_{24} & \mathcal{D}_{25} & \mathcal{D}_{26} \\ \mathcal{D}_{31} & \mathcal{D}_{32} & \mathcal{D}_{33} & \mathcal{D}_{34} & \mathcal{D}_{35} & \mathcal{D}_{36} \\ \mathcal{D}_{41} & \mathcal{D}_{42} & \mathcal{D}_{43} & \mathcal{D}_{44} & \mathcal{D}_{45} & \mathcal{D}_{46} \\ \mathcal{D}_{51} & \mathcal{D}_{52} & \mathcal{D}_{53} & \mathcal{D}_{54} & \mathcal{D}_{55} & \mathcal{D}_{56} \\ \mathcal{D}_{61} & \mathcal{D}_{62} & \mathcal{D}_{63} & \mathcal{D}_{64} & \mathcal{D}_{65} & \mathcal{D}_{66} \end{pmatrix} \tag{B.7}$$

We assume dipole forbidden transitions are equal to zero. Additionally we assume diagonal elements are equal to zero. Meaning that the atoms have no permanent dipole moments, which is true for atoms with spherically symmetric wave functions. This assumption holds for a variety of atomic materials, including Rb. Thus, the perturbation H becomes

$$H_I = -E\begin{pmatrix} 0 & 0 & \mathcal{D}_{13} & \mathcal{D}_{14} & \mathcal{D}_{15} & 0 \\ 0 & 0 & 0 & \mathcal{D}_{24} & \mathcal{D}_{25} & \mathcal{D}_{26} \\ \mathcal{D}_{31} & 0 & 0 & 0 & 0 & 0 \\ \mathcal{D}_{41} & \mathcal{D}_{42} & 0 & 0 & 0 & 0 \\ \mathcal{D}_{51} & \mathcal{D}_{52} & 0 & 0 & 0 & 0 \\ 0 & \mathcal{D}_{62} & 0 & 0 & 0 & 0 \end{pmatrix} \tag{B.8}$$

Using the time evolution operator, we can transform H_0 into the interaction picture. Since the unperturbed H is diagonal, it can be written as

$$U(t) = e^{iH_0t/\hbar} = \begin{pmatrix} e^{i\omega_1 t} & 0 & 0 & 0 & 0 & 0 \\ 0 & e^{i\omega_2 t} & 0 & 0 & 0 & 0 \\ 0 & 0 & e^{i\omega_3 t} & 0 & 0 & 0 \\ 0 & 0 & 0 & e^{i\omega_4 t} & 0 & 0 \\ 0 & 0 & 0 & 0 & e^{i\omega_5 t} & 0 \\ 0 & 0 & 0 & 0 & 0 & e^{i\omega_6 t} \end{pmatrix} \tag{B.9}$$

Applying the transformation for the perturbed H $V = e^{iH_0t/\hbar}H_Ie^{-iH_0t/\hbar}$, we get

$$V = -E\begin{pmatrix} 0 & 0 & \mathcal{D}_{13}e^{i(\omega_1-\omega_3)t} & \mathcal{D}_{14}e^{i(\omega_1-\omega_4)t} & \mathcal{D}_{15}e^{i(\omega_1-\omega_5)t} & 0 \\ 0 & 0 & 0 & \mathcal{D}_{24}e^{i(\omega_2-\omega_4)t} & \mathcal{D}_{25}e^{i(\omega_2-\omega_5)t} & \mathcal{D}_{26}e^{i(\omega_2-\omega_6)t} \\ \mathcal{D}_{31}e^{i(\omega_1-\omega_3)t} & 0 & 0 & 0 & 0 & 0 \\ \mathcal{D}_{41}e^{i(\omega_4-\omega_1)t} & \mathcal{D}_{42}e^{i(\omega_4-\omega_2)t} & 0 & 0 & 0 & 0 \\ \mathcal{D}_{51}e^{i(\omega_5-\omega_1)t} & \mathcal{D}_{52}e^{i(\omega_5-\omega_2)t} & 0 & 0 & 0 & 0 \\ 0 & \mathcal{D}_{62}e^{i(\omega_6-\omega_2)t} & 0 & 0 & 0 & 0 \end{pmatrix} \tag{B.10}$$

Now we can substitute in the EF, and expand the cosines in terms of exponentials as following

$$\boldsymbol{E} = \boldsymbol{E_p}/2(e^{i\omega_pt} + e^{-i\omega_pt}) + \boldsymbol{E_c}/2(e^{i\omega_ct} + e^{-i\omega_ct}) \tag{B.11}$$

Sub class of the matrix elements of the interaction H, considering that the EF is along the dipole moment axis can be written as

$$\begin{aligned} V_{13} &= -\mathcal{D}_{13}[E_p/2(e^{i\omega_pt} + e^{-i\omega_pt}) + E_c/2(e^{i\omega_ct} + e^{-i\omega_ct})]e^{i(\omega_1-\omega_3)t}, \\ V_{14} &= -\mathcal{D}_{14}[E_p/2(e^{i\omega_pt} + e^{-i\omega_pt}) + E_c/2(e^{i\omega_ct} + e^{-i\omega_ct})]e^{i(\omega_1-\omega_4)t}, \\ V_{15} &= -\mathcal{D}_{15}[E_p/2(e^{i\omega_pt} + e^{-i\omega_pt}) + E_c/2(e^{i\omega_ct} + e^{-i\omega_ct})]e^{i(\omega_1-\omega_5)t}, \\ V_{24} &= -\mathcal{D}_{24}[E_p/2(e^{i\omega_pt} + e^{-i\omega_pt}) + E_c/2(e^{i\omega_ct} + e^{-i\omega_ct})]e^{i(\omega_2-\omega_4)t}, \end{aligned} \tag{B.12}$$

Other elements can be written in a similar way. For the rest of the derivation, we would like to discard the rapidly oscillating terms and consider the RWA. We are assuming that any quickly oscillating term will be averaged out on the time scale of observation. Note that, ω_p is near resonance with the $\omega_1 \longrightarrow \omega_3$ transition, so the difference $\omega_3 - \omega_1 - \omega_p$ will be small, and any exponentials with these terms will remain since they oscillate slowly. However, terms containing the sum $\omega_3 - \omega_1 + \omega_p$ will be large, and so these quickly oscillating terms can be dropped in the RWA. Similar reasoning is applied to all terms. Only one term of four in each matrix element survives. By applying the unitary transformation again, we can go back to shrödinger picture

$$H_I = -\frac{1}{2}\begin{pmatrix} 0 & 0 & \mathcal{D}_{13}E_pe^{i\omega_pt} & \mathcal{D}_{14}E_pe^{i\omega_pt} & \mathcal{D}_{15}E_pe^{i\omega_pt} & 0 \\ 0 & 0 & 0 & \mathcal{D}_{24}E_ce^{i\omega_ct} & \mathcal{D}_{25}E_ce^{i\omega_ct} & \mathcal{D}_{26}E_ce^{i\omega_ct} \\ \mathcal{D}_{31}E_pe^{-i\omega_pt} & 0 & 0 & 0 & 0 & 0 \\ \mathcal{D}_{41}E_pe^{-i\omega_pt} & \mathcal{D}_{42}E_ce^{-i\omega_ct} & 0 & 0 & 0 & 0 \\ \mathcal{D}_{51}E_pe^{-i\omega_pt} & \mathcal{D}_{52}E_ce^{-i\omega_ct} & 0 & 0 & 0 & 0 \\ 0 & \mathcal{D}_{62}E_ce^{-i\omega_ct} & 0 & 0 & 0 & 0 \end{pmatrix} \tag{B.13}$$

Since the dipole operator is complex, we can write it in terms of its magnitude and phase

$$\begin{aligned}\mathcal{D}_{13} = \mathcal{D}_{31} &= |\mathcal{D}|\sqrt{S_{13}}e^{i\phi_p} \\ \mathcal{D}_{24} = \mathcal{D}_{24} &= |\mathcal{D}|\sqrt{S_{24}}e^{i\phi_c}\end{aligned} \tag{B.14}$$

Where $S_{ff'}$ provides a measure of the relative strength of each of the $F \longrightarrow F'$ transitions and $|\mathcal{D}|$ is the general dipole moment for all of the transitions from $J \longrightarrow J'$, $|\langle J|er|J'\rangle|^2$. One can calculate the $S_{ff'}$ using Wigner 6-j symbol [66]

$$\begin{aligned}S_{FF'} &:= \sum_q (2F'+1)(2J+1) \begin{Bmatrix} J & J' & 1 \\ F' & F & I \end{Bmatrix}^2 |\langle F m_F \mid F'(m_F - q); 1q\rangle|^2 \\ &= (2F'+1)(2J+1) \begin{Bmatrix} J & J' & 1 \\ F' & F & I \end{Bmatrix}^2 .\end{aligned} \tag{B.15}$$

Here, q is an index labeling the component of r in the spherical basis. Independent of the particular GS sublevel chose, the $S_{FF'}$ obeys the sum rule

$$\sum_{F'} S_{FF'} = 1 \tag{B.16}$$

If one calculates the relative HF strength factor for ^{87}Rb transitions, the values could be find as following [30]

$D_2\left(5^2\ S_{1/2} \longrightarrow 5^2P_{3/2}\right)$ transition	S_{23}	7/10	S_{12}	5/12
	S_{22}	1/4	S_{11}	5/12
	S_{21}	1/20	S_{10}	1/6
$D_1\left(5^2\ S_{1/2} \longrightarrow 5^2P_{1/2}\right)$ transition	S_{22}	1/2	S_{12}	5/6
	S_{21}	1/2	S_{11}	1/6

Table B.1: Dipole strength for the D_2 and D_1 lines in Rb.

RBF for transitions $|1\rangle$ to $|3\rangle$ and $|2\rangle$ to $|4\rangle$ can be defined now as

$$\begin{aligned}\Omega_p &= \frac{E_p|\mathcal{D}|S_{13}}{\hbar} \\ \Omega_c &= \frac{E_c|\mathcal{D}|S_{24}}{\hbar}\end{aligned} \tag{B.17}$$

With the RBF and phase of the dipole operator separated, we can write the total H as

$$H_T = -\frac{\hbar}{2}\begin{pmatrix} 2\omega_1 & 0 & S_{13}\Omega_p e^{i\omega_p t}e^{i\phi_p} & S_{14}\Omega_p e^{i\omega_p t}e^{i\phi_p} & S_{15}\Omega_p e^{i\omega_p t}e^{i\phi_p} & 0 \\ 0 & 2\omega_2 & 0 & S_{24}\Omega_c e^{i\omega_c t}e^{i\phi_c} & S_{25}\Omega_c e^{i\omega_c t}e^{i\phi_c} & S_{26}\Omega_c e^{i\omega_c t}e^{i\phi_c} \\ S_{31}\Omega_p e^{-i\omega_p t}e^{-i\phi_p} & 0 & 2\omega_3 & 0 & 0 & 0 \\ S_{41}\Omega_p e^{-i\omega_p t}e^{-i\phi_p} & S_{42}\Omega_c e^{-i\omega_c t}e^{-i\phi_c} & 0 & 2\omega_4 & 0 & 0 \\ S_{51}\Omega_p e^{-i\omega_p t}e^{-i\phi_p} & S_{52}\Omega_c e^{-i\omega_c t}e^{-i\phi_c} & 0 & 0 & 2\omega_5 & 0 \\ 0 & S_{62}\Omega_c e^{-i\omega_c t}e^{-i\phi_c} & 0 & 0 & 0 & 2\omega_6 \end{pmatrix} \tag{B.18}$$

Next, we apply corotating frame approximation to get rid of the dipole moment phase and time dependence of the H. We define new basis as rotating basis and the transformation between basis can be carried out using $|\tilde{n}\rangle = \tilde{U}(t)|n\rangle$ with the unitary operator $\tilde{U}(t)$ given by

$$\tilde{U}(t) = \begin{pmatrix} e^{-i\omega_p t}e^{-i\phi_p t} & 0 & 0 & 0 & 0 & 0 \\ 0 & e^{-i\omega_c t}e^{-i\phi_c t} & 0 & 0 & 0 & 0 \\ 0 & 0 & 1 & 0 & 0 & 0 \\ 0 & 0 & 0 & 1 & 0 & 0 \\ 0 & 0 & 0 & 0 & 1 & 0 \\ 0 & 0 & 0 & 0 & 0 & 1 \end{pmatrix} \tag{B.19}$$

To get the new H based on the transformed basis, we can write the shrödinger equation

$$\begin{aligned} \tilde{H}_T|\tilde{n}\rangle &= i\hbar\frac{\partial}{\partial t}|\tilde{n}\rangle \\ &= i\hbar\frac{\partial}{\partial t}(\tilde{U}|n\rangle) \\ &= i\hbar\left(\frac{\partial\tilde{U}}{\partial t}|n\rangle + \tilde{U}\frac{\partial|n\rangle}{\partial t}\right) \\ &= i\hbar\left(\frac{\partial\tilde{U}}{\partial t}|n\rangle + \frac{-i}{\hbar}\tilde{U}H_T|n\rangle\right) \\ &= \left(i\hbar\frac{\partial\tilde{U}}{\partial t}\tilde{U}^\dagger + \tilde{U}H_T\tilde{U}^\dagger\right)\tilde{U}|n\rangle \\ \tilde{H}_T|\tilde{n}\rangle &= \left(i\hbar\frac{\partial\tilde{U}}{\partial t}\tilde{U}^\dagger + \tilde{U}H_T\tilde{U}^\dagger\right)|\tilde{n}\rangle. \end{aligned} \tag{B.20}$$

Eventually, we can see the benefit of the transformation when we write the H

$$H_T = -\frac{\hbar}{2}\begin{pmatrix} -2(\omega_1+\omega_p) & 0 & S_{13}\Omega_p & S_{14}\Omega_p & S_{15}\Omega_p & 0 \\ 0 & -2(\omega_2+\omega_c) & 0 & S_{24}\Omega_c & S_{25}\Omega_c & S_{26}\Omega_c \\ S_{31}\Omega_p & 0 & -2\omega_3 & 0 & 0 & 0 \\ S_{41}\Omega_p & S_{42}\Omega_c & 0 & -2\omega_4 & 0 & 0 \\ S_{51}\Omega_p & S_{52}\Omega_c & 0 & 0 & -2\omega_5 & 0 \\ 0 & S_{62}\Omega_c & 0 & 0 & 0 & -2\omega_6 \end{pmatrix} \tag{B.21}$$

Now, we will add $-2(\omega_1+\omega_p)\mathbf{1}$ to the H. With adding that identity to the matrix we will effectively be redefining our EVs by setting $\omega_n \longrightarrow \omega_n + B$ for some constant B. This has no physical effect, as the physically relevant terms are the differences between energy levels. With that, the H becomes

$$H_T = -\frac{\hbar}{2}\begin{pmatrix} 0 & 0 & S_{13}\Omega_p & S_{14}\Omega_p & S_{15}\Omega_p & 0 \\ 0 & 2(\Delta_p-\Delta_c) & 0 & S_{24}\Omega_c & S_{25}\Omega_c & S_{26}\Omega_c \\ S_{31}\Omega_p & 0 & 2\Delta_p & 0 & 0 & 0 \\ S_{41}\Omega_p & S_{42}\Omega_c & 0 & 2(\Delta_p+[\omega_4-\omega_3]) & 0 & 0 \\ S_{51}\Omega_p & S_{52}\Omega_c & 0 & 0 & 2(\Delta_p+[\omega_5-\omega_3]) & 0 \\ 0 & S_{62}\Omega_c & 0 & 0 & 0 & 2(\Delta_p+[\omega_6-\omega_3]) \end{pmatrix} \tag{B.22}$$

Where $\Delta_p = \omega_p - \omega_3 + \omega_1$ and $\Delta_c = \omega_c - \omega_3 + \omega_2$. Note that, having $\omega_{i+1} - \omega_i$ for $i \in [3,4,5]$ in our H enables us to quantify the energy splitting between the F′ levels. Although, we derived this for the specific D_2 line transition, the general approach is the same for other atomic systems with more than 3 levels.

Appendix C

Tuning Diode Lasers for Precision Spectroscopy

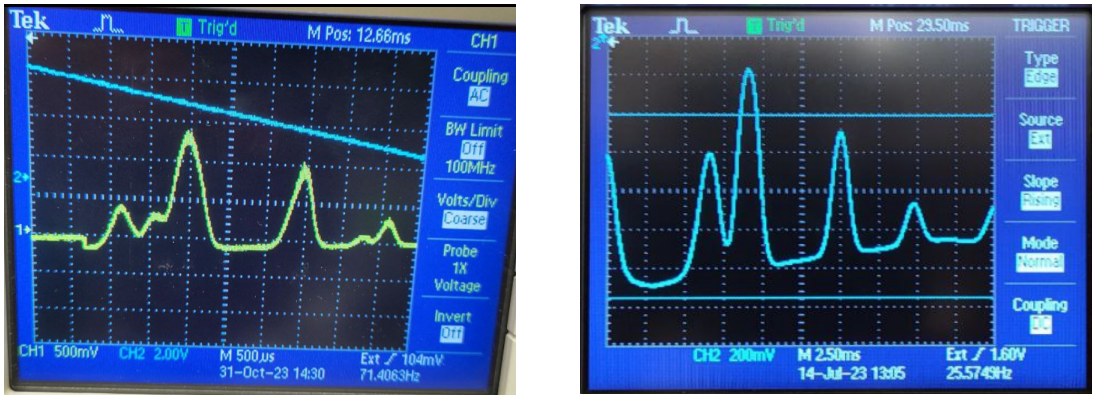

(a) (b)

Figure C.1: D_1 and D_2 transition of natural abundance Rb VC with a reasonable MHFR to observe the entire manifold.

Tuning diode lasers is a meticulous process that demands patience and considerable time investment. The goal is to achieve precise control over the laser's output wavelength and ensure it aligns with the specific requirements of the experiment, such as resonating with atomic transitions in Rb VCs.

The first step in tuning the diode laser is to *identify its lasing region.* This involves carefully adjusting the injection current supplied to the laser diode. The current should be increased gradually until it slightly exceeds the threshold necessary for lasing to occur. Operating just above this threshold helps maintain the stability of the laser and prevents damage that could be caused by excessive current. Since diode

lasers often emit in the IR spectrum, using an IR camera is essential. The camera allows for the visualization of "flashing points," which are moments when the laser begins to emit light at different modes. These flashing points correspond to various lasing regions and provide valuable information for mapping the laser's operational characteristics.

Once the lasing region is established, the next step is to *monitor the laser's wavelength and its interaction with Rb atoms simultaneously*. This is achieved by incorporating a Beam Splitter (BS) into the laser's optical path. The BS directs a portion of the laser beam towards a wavelength measurement device, such as a spectrometer or a wavemeter, while the remaining light continues through the Rb VC. As the laser light passes through the VC, it interacts with the Rb atoms, and when the laser's wavelength matches the atomic transitions of Rb, fluorescence occurs. Observing this fluorescence provides immediate FB on whether the laser is correctly tuned to the desired atomic transition.

Fine-tuning the laser involves adjusting various control knobs and parameters to ensure that the *MHFR* is appropriate for the experiment. The MHFR should be sufficient resolving specific spectral features without interference from adjacent modes. Adjustments may include tweaking the angle of the diffraction grating in the external cavity, modifying the cavity length, or fine-tuning the diode's temperature. Each of these adjustments affects the laser's output wavelength and mode structure. It is important to make these adjustments incrementally and methodically, as changes in one parameter can influence others.

Throughout the tuning process, maintaining stability is of utmost importance. Environmental factors such as temperature fluctuations and mechanical vibrations can cause mode hopping or drift in the laser's output. To minimize these effects, the laser setup should be isolated from vibrations, and temperature control mechanisms should be employed to keep the diode and external cavity at constant temperatures.

Here is a systematic approach for tuning ECDLs:

1. **Identify the Lasing Region**: Gradually increase the injection current just above the lasing threshold while using an IR camera to detect flashing points indicative of different lasing modes.

2. **Simultaneous Monitoring**: Use a BS to send part of the laser beam to a wavelength measurement device and the other part through an Rb VC to observe fluorescence, ensuring the laser wavelength aligns with the atomic transition.

3. **Fine-Tuning Adjustments**: Carefully adjust the diffraction grating angle, cavity length, and diode temperature to achieve the desired MHFR and optimize the laser's performance for the experiment.

4. **Maintain Stability**: Employ vibration isolation and temperature control to prevent environmental factors from affecting the laser's output.

By meticulously following these steps and making precise adjustments, the diode laser can be effectively tuned to meet the specific needs of the experiment. Patience and careful observation are key, as the interplay between different parameters requires a thoughtful and methodical approach to achieve optimal results.

Appendix D

Construction of MOT

We acquired a VS, which included both a turbopump and roughing pumps, on loan from another department. A diagram of the system configuration is shown in Fig. D.1.

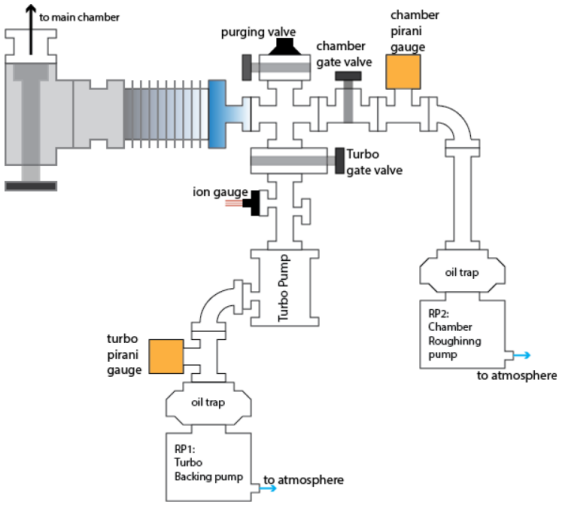

Figure D.1: VS setup used for the BO process

The roughing system is divided into four branches. The upper branch is equipped with a valve and nozzle, which can be used to introduce dry nitrogen into the system to break the vacuum. On the right, there is a gate valve, a Pirani gauge (referred to as the "chamber" Pirani gauge), and the roughing pump for the inlet. The bottom branch includes another gate valve leading to the turbopump, as well as an ion gauge. The turbopump's exhaust is connected to a second roughing pump and another Pirani gauge. Finally, the last branch is an open end, fitted with a bellows, which allows for

the connection of the MOT chamber. Since the roughing system was already deemed clean, no additional cleaning or BO was necessary.

The MOT chamber comprises a four-way cross, an electrical FT, an ion pump, a glass cell, and a gate valve as it is shown in Fig. D.2

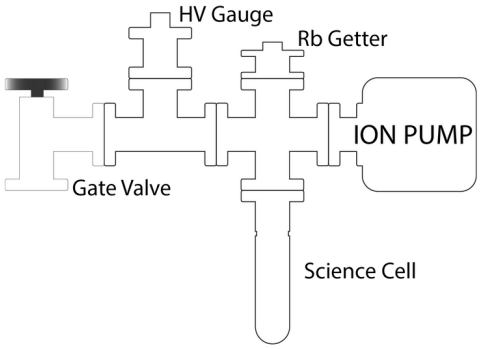

Figure D.2: Layout of the MOT system

A bellows is used to connect this chamber to the roughing system. A custom metal holder was fabricated to secure the MOT chamber to the optical table as it is shown in the Fig. D.3.

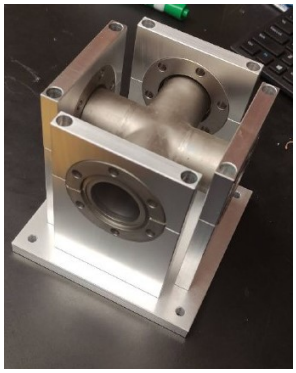

Figure D.3: Cross holder for the MOT designed and machined with the help of Chris Secord.

Figure D.4: Air drying the parts after cleaning them

Prior to assembly, all vacuum components were meticulously cleaned to remove any potential contaminants from machining or handling processes and placed in a clean environment to let be air dried as it is shown in Fig. D.4. Throughout the cleaning procedure, powder-free latex gloves were used. Ultrasonic cleaner were used to clean all of the parts as it is shown in Fig. D.5.

Figure D.5: Ultrasonic bathing parts to get rid of contaminations that are hard to get rid of in a conventional way.

. Furthermore, components were washed using unscented dish soap and water, followed by a hot tap water rinse. Next, the parts were rinsed with acetone, deionized water, ethanol, and a final rinse with deionized water. For instances where wiping was required, a Thorlabs cloth soaked in ethanol was used. After cleaning, the components were laid out to air dry, and a heat gun was used with caution to avoid overheating plastic or rubber components. Once fully dried, the openings of each component were wrapped in aluminum foil until assembly.

The Rb getters had to be attached to the FT before final assembly. Since getters are prone to oxidation, they must be stored in a desiccator for long-term storage but can be exposed to air for short periods without significant degradation. The getters were laser welded together at sharp angles in pairs, and then secured to the FT using Beryllium-Copper screws, nuts, and slotted screw adapters. Fixture for laser welding the getters were design, Beryllium-Copper screws were modified so that the getters could sit nicely on them. Fixture, modified screws and final FT containing getters are shown in Fig. D.6.

(a)

(b)

(c)

Figure D.6: FT containing modified screws and laser welded getters designed and built with the help of Chris Secord and Mark Lenkowski.

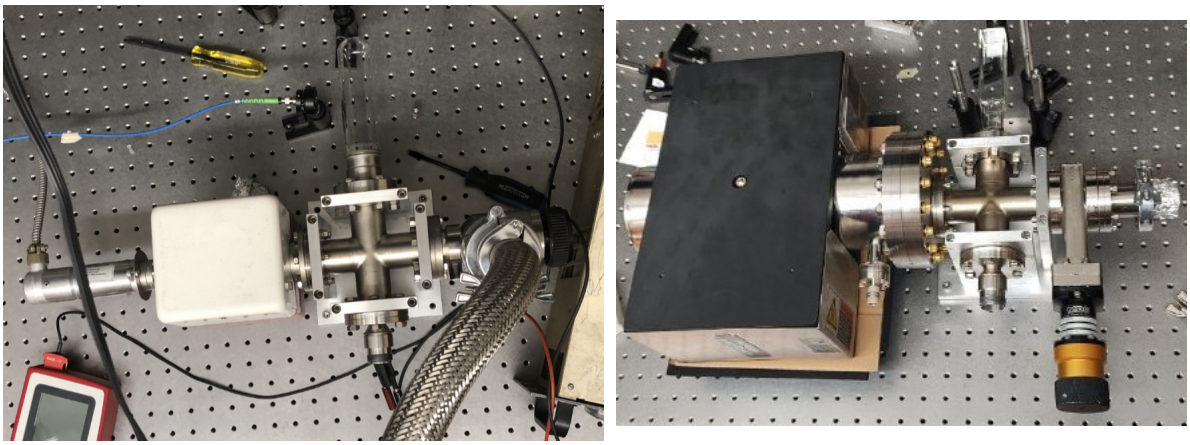

(a) (b)

Figure D.7: Two version of MOTs that we have assembled during the coarse of a few months. MOT version (a) got wrecked after the incident. MOT version (b) is still functioning (knock on wood!).

During the assembly of ConFlat flanged components, a copper gasket was inserted between the knife edges of the two ConFlats. The six through-holes were aligned, and powder-coated screws were inserted and hand-tightened with nuts. To ensure uniform compression of the gasket, the screws were tightened in a specific alternating star-shape pattern: top, bottom, top-right, bottom-left, bottom-right, and top-left. This tightening sequence was repeated until the flanges were nearly in contact. Each MOT cell component was assembled following this procedure, and our two version of MOTs assembled are shown in Fig D.7. The cleaning process alone is insufficient to remove all contaminants, especially water and hydrocarbons trapped in metal pores. These contaminants are removed by baking out the system, which involves heating the vacuum components to high temperatures while the vacuum pumps are operational. This process helps to vaporize the trapped contaminants and flush them out of the system. In order to BO the MOT, an electrical controller has been designed as shown in Fig. D.8

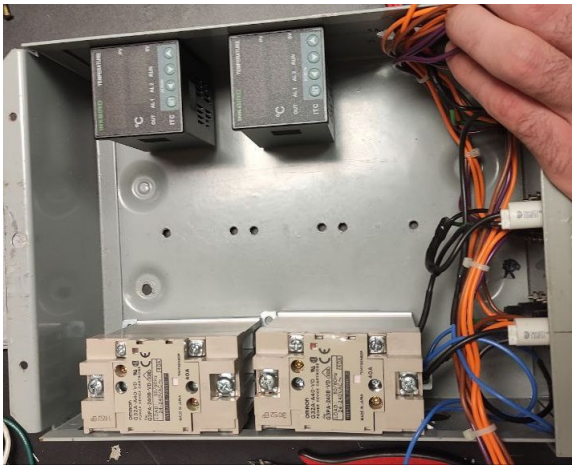

(a)

(b)

Figure D.8: BO controller designed and assembled with the help of Nick Braam for BO procedure

To begin the pump-down process, with all other valves closed, the inlet pump was turned on and its corresponding valve was opened. After three minutes of operation, the right branch of the roughing system and the bellows leading to the MOT chamber achieved a pressure of 3.4×10^{-2}Torr. The valve to the main MOT chamber was then opened, and the system was further pumped down to the same vacuum level. Once the pressure reached the 10^{-3}Torr range, the inlet pump was shut off and the chamber's gate valve was closed.

The backing pump was then activated to reduce the pressure behind the turbopump to 2×10^{-1}Torr. With the backing pump running and the system sufficiently evacuated, the turbopump was switched on, causing the pressure to drop further, as indicated by the upper Pirani gauge. To minimize wear on the ion pump, it was only activated once the turbopump had reached its lowest achievable pressure. After 90 minutes of operation, the turbopump reached a pressure of 2.9×10^{-6}Torr, at which point the ion pump was turned on. Initially, the pressure spiked to 3.6×10^{-6}Torr due to the ion pump releasing particles into the system, but it stabilized after 10 minutes. At this point, the BO process could commence.

For the BO, the MOT chamber was thermally isolated from the optical table by placing glass slides beneath the chamber's metal holder. Fiberglass heating tape was then wrapped around the metal components, including the CFFs, and connected to

a temperature controller. Thermocouples were strategically placed, one at the center of the four-way cross beneath the heating tape, another at the junction between the metal and glass components, and a third on the gate valve to monitor the temperature of the rubber o-ring. The MOT chamber was wrapped in aluminum foil to reduce radiative heat loss, and additional layers of foil and mesh were applied to minimize convective heat loss as it is shown in Fig. D.9.

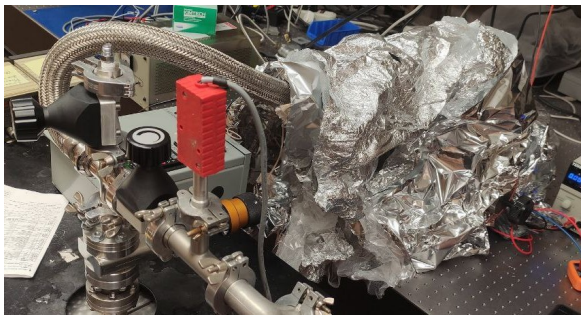

Figure D.9: Baking the MOT with aluminum foil and mesh wrapped on it

The temperature was gradually increased, starting at 40°C and rising in increments of no more than 10°C every 10 minutes. Once the thermal gradient across the glass-metal junction stabilized, the temperature increase rate was accelerated. The final temperature was set to 200°C, while the temperature at the glass cell stabilized at 113°C. As the temperature rose, the system pressure also increased until reaching 170°C. To remove any remaining contaminants from the getters, a 2A current was applied, causing the pressure to increase by approximately 10^{-6}Torr/s. The ion pump was deactivated during this process, and the getter current was gradually increased to 3A. The system was maintained in this state for a full day, and the final pressure reached 2.5×10^{-6} Torr after the ion pump was reactivated.

Since bellows are known to trap moisture, a second thermocouple and heating tape were applied to the bellows between the MOT chamber and the roughing system. The bellows were heated to 200°C, while the four-way cross was raised to 320°C, ensuring that the rubber O-ring's temperature remained below 120°C. After a two-day BO, the final pressure reached 7.8×10^{-7}Torr.

The system was then cooled down in 10°C increments every 10 minutes until room temperature was achieved. At this stage, the pressure had dropped to 9.0×10^{-8}Torr, and the gate valve to the MOT chamber was closed.

Appendix E

MOT coils configuration, Design, and Characterization

There are several approaches to generating the quadrupole MF required for a MOT. Generally, any pair of coaxial coils with opposing current directions can produce a suitable MF for a MOT. We designed rectangular coil and two version of circular coils along the duration of this project. The most common setup is the anti-Helmholtz configuration, which involves two circular coils of radius R, spaced by a distance equal to R. This arrangement generates a zero MF at the midpoint between the coils and produces a linear MF gradient along the z-axis, as well as radially in the x-y plane. Using rectangular coils instead of circular ones produces a zero MF at the geometric center, but also generates linear field gradients along the three central axes which is known to create an elongated MOT cloud, often referred to as a "cigar-shaped" MOT, which is favorable due to its higher OD along the cloud's long axis. In our setup, the first coil design consisted of rectangular coils measuring 6cm by 11cm, separated by a 6cm gap. These coil holders, designed in solidWorks and 3D printed using Polylactic acid (PLA), supported 25 windings of 17-gauge copper wire. To wind the coils, they were clamped onto a hand lathe and rotated while the wire was fed manually. For smaller or more fragile coil designs, the lathe's force might cause the 3D-printed material to break. To reinforce the coil holders, the PLA surface can be lightly brushed with acetone or exposed to acetone vapor, which creates a hardened finish that reduces the risk of breakage. We made a fixture to be able to wrap the coils. All three versions of magnetic coils designed for the MOT system can be seen in Fig. E.1.

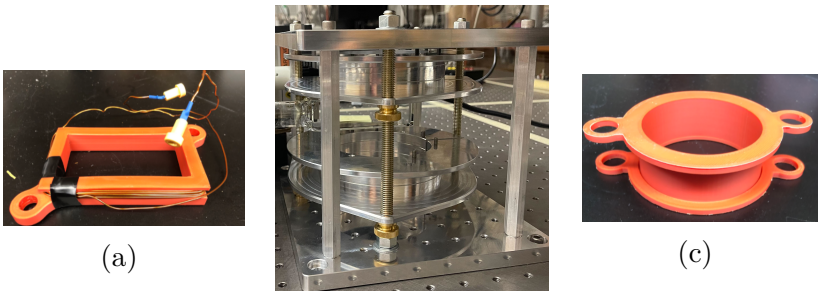

(a) (b) (c)

Figure E.1: Three version of coils designed for MOT with the help of Brendan Mackey and Chris Secord. The first version (a). The second version (c). The last version (b)

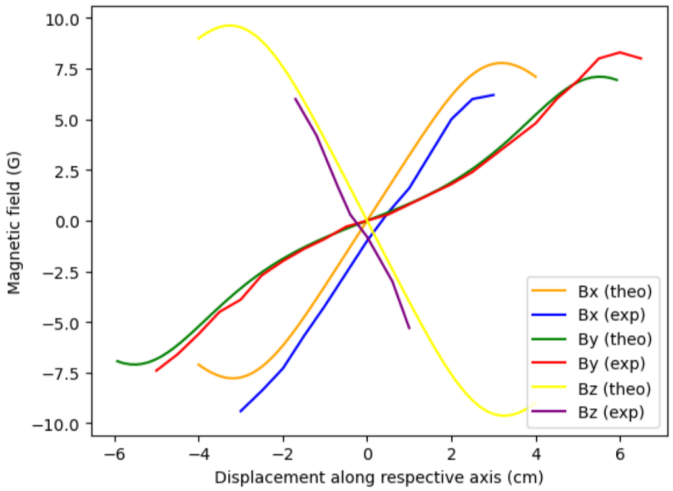

Figure E.2: The rectangular 25-turn anti-Helmholtz coil configuration, measuring 6cm $\times$ 6cm $\times$ 11cm and carrying a current of 3.09A, was simulated along the primary axes: x, y, and z. Additionally, the experimentally measured MFs along the same axes are superimposed for comparison

To achieve a functional MOT, we require MF gradients of at least 10G/cm. The MF gradients generated by the coils were measured incrementally along each axis using a Gaussmeter, and simulations were performed using Python to compare the measured and simulated fields. Coil simulations generally rely on finite current elements, which produce a MF given by:

$$\mathbf{B} = \mu_0/(4\pi r)(sin\theta_2 - sin\theta_1)(\mathbf{I} \times \hat{r}) \tag{E.1}$$

For rectangular coils, we applied the thin coil approximation, treating each coil as

a single wire loop with an effective current equal to the total coil current multiplied by the number of turns (25 in this case). In our simulations, the coils were approximated by just eight current elements. The results, both measured and simulated, are shown in Fig E.2. The gradient values along the x, y, and z axes were found to be fairly consistent between the simulations and the measurements. The simulated gradients were 3.13G/cm (x-axis), 0.85G/cm (y-axis), and 4.00G/cm (z-axis), while the measured values were 3.23G/cm, 0.81G/cm, and 4.03G/cm, respectively. Since the field gradients scale linearly with current, a current of approximately 9.6A would be required to achieve the desired gradient of 10G/cm along the x and z-axes. However, at this current level, the heat produced by the coils was sufficient to start melting the PLA material. That is one of the reasons why we moved to the third design that we used metal holders to avoid the melting from generated heat. Moreover, the gradient along the y-axis was notably weak, which, while desirable for creating a cigar-shaped MOT, could lead to a cloud that is too diffuse. To improve the design, we needed to either enhance the coil's heat dissipation capabilities or devise a new coil configuration that could generate the necessary MF with less current. Our second design used the anti-Helmholtz configuration with a separation of 1.25R, The coils had a radius of R=31.4 and were separated by 39 mm, just large enough to fit around the 1.5-inch diameter glass cell used in the MOT. Second version of magnetic coil were designed with 12 turns across and 4 turns outward, using 17-gauge magnet wire for a total of 48 windings. This design allowed for better heat dissipation by increasing the coil's exposed surface area. Simulations of this configuration showed that it provided a higher MF gradient compared to the smallest pair of anti-Helmholtz coils that could fit around the MOT cell (1.5in). Specifically, the 1.25R configuration produced a gradient of 12.4G/cm, compared to the 8.8G/cm gradient of the smaller anti-Helmholtz setup. The new design demonstrated the ability to generate gradients greater than 10G/cm without exceeding 3A of current, which is low enough to prevent the coils from overheating. This configuration, therefore, offered a more reliable and efficient solution for achieving the desired MF gradients in a MOT setup. For the third version of magnetic coils, we used 365 turns of magnetic wire of gate 16 with diameter of 1.3mm. This gives us a gradient of 15G/cm when we provide current of 3A.

Appendix F

QO Simulations with QuTiP

F.1 Introduction to QuTiP

The **QuTiP** is an open-source framework designed for simulating QSs. Its modular and Python-friendly structure allows researchers to efficiently model the dynamics of open QSs, QO, and superconducting circuits. QuTiP offers both time-dependent and SSS, enabling investigations of dissipation, quantum entanglement, coherence, and non-classical light. The framework is widely used in the QO community for studying systems such as CQED, spin ensembles, and EIT.

Here, we have a mini-tutorial on how to use QuTiP for modeling a three-level lambda system, an essential configuration for **EIT** and light storage. Additionally, we provide a concise overview on how QuTiP solvers can be applied to solve Schrödinger and master equations in QO simulations.

F.2 Solvers Overview

QuTiP offers several solvers to handle different quantum mechanical scenarios. Two common approaches for QO problems are:

- **Schrödinger Equation Solver:** Models the evolution of pure states.

$$i\hbar\frac{d}{dt}|\psi(t)\rangle = H(t)|\psi(t)\rangle$$

- **mesolver:** Handles systems interacting with an environment, accounting for

dissipation and decoherence.

$$\frac{d}{dt}\rho(t) = -\frac{i}{\hbar}[H(t), \rho(t)] + \sum_i \mathcal{D}[L_i]\rho(t)$$

Here, $\mathcal{D}[L_i]$ represents the Lindblad dissipation operator.

The solvers in QuTiP are easy to customize for different QSs. For example, `mesolve()` is typically used for master equations, while `sesolve()` applies to pure states.

F.3 Tutorial: Simulating a Three-Level Lambda System in QuTiP

Below is a step-by-step tutorial on how to set up and simulate a basic three-level system (lambda configuration) using QuTiP. This example focuses on simulating **EIT** with two excited states in the ^{87}Rb D_1 transition.

Step 1: Installation and Setup

Make sure QuTiP is installed. You can install it via:

```
pip install qutip
```

Step 2: Defining System Parameters

We start by defining the H, decay rates, and other relevant parameters for the lambda system.

```
import qutip as qt
import numpy as np

# System parameters
omega_p = 1.0  # PF RBF
omega_c = 5.0  # Coupling field RBF
delta_p = 0.0  # Probe detuning
delta_c = 0.0  # Coupling detuning
gamma = 0.5     # Decay rate from excited states
```

```
# Basis states: |1>, |2>, |3> (ground, excited, excited)
ground = qt.basis(3, 0)
excited_1 = qt.basis(3, 1)
excited_2 = qt.basis(3, 2)
```

Step 3: Constructing the H

The H for the lambda system consists of interaction terms for the probe and coupling fields:

```
H = delta_p * excited_1 * excited_1.dag() + delta_c * excited_2 * excited_2.dag()
    + omega_p * (ground * excited_1.dag() + excited_1 * ground.dag()) \
    + omega_c * (ground * excited_2.dag() + excited_2 * ground.dag())
```

Step 4: Setting Up Dissipation

We include Lindblad operators to account for spontaneous decay from the excited states:

```
L1 = np.sqrt(gamma) * ground * excited_1.dag()  # Decay |1> -> |3>
L2 = np.sqrt(gamma) * ground * excited_2.dag()  # Decay |2> -> |3>

collapse_ops = [L1, L2]
```

Step 5: Solving the Master Equation

We can now use the `mesolve()` function to simulate the system's evolution over time:

```
# Time array for simulation
times = np.linspace(0, 25, 1000)

# Initial state: all population in the GS
rho0 = ground * ground.dag()

# Solving the master equation
result = qt.mesolve(H, rho0, times, collapse_ops, [ground * ground.dag()])
```

Step 6: Visualizing the Results

We can plot the population in the GS over time to observe the EIT effect.

```
import matplotlib.pyplot as plt


plt.plot(times, np.real(result.expect[0]), label="GS population")
plt.xlabel("Time")
plt.ylabel("Population")
plt.title("EIT in a Lambda System")
plt.legend()
plt.show()
```

F.4 How the Solver Works

The solver implemented for QO simulations operates by numerically solving the time-dependent **Schrödinger equation** for pure states or the **master equation** for density matrices. The following is a high-level overview of how the solver works:

- **H Construction:** The H of the QS is defined as a sum of static and time-dependent components. This H represents the total energy of the system, including interactions between states and external fields.
- **Time Evolution:** For pure states, the solver uses:

$$i\hbar \frac{d}{dt}|\psi(t)\rangle = H(t)|\psi(t)\rangle$$

  For DMs (mixed states), the solver applies the master equation:

$$\frac{d}{dt}\rho(t) = -\frac{i}{\hbar}[H(t), \rho(t)] + \sum_i \mathcal{D}[L_i]\rho(t)$$

  The evolution is discretized over a time grid, where each step updates the state vector or DM.
- **Incorporating Dissipation:** Dissipative effects, such as spontaneous emission or decoherence, are modeled using Lindblad operators. Each operator L_i

defines a specific type of decay or loss in the system, and the solver applies the corresponding dissipation term:

$$\mathcal{D}[L_i]\rho = L_i \rho L_i^\dagger - \frac{1}{2}\left(L_i^\dagger L_i \rho + \rho L_i^\dagger L_i\right)$$

- **State Initialization:** The user initializes the system by providing an initial state, which can be a pure state $|\psi_0\rangle$ or a DM ρ_0. The solver evolves this state over a given time interval.
- **Observables and Expectation Values:** During the simulation, the solver can compute expectation values of observables, such as population in a particular state. These values are recorded at each time step to analyze the system's behavior.
- **Numerical Integration:** QuTiP's solvers use adaptive algorithms (such as `zvode` from the `SciPy` library) to integrate the equations of motion efficiently. These algorithms dynamically adjust step sizes to maintain accuracy and stability.
- **Result Output:** After the simulation completes, the solver returns the time-evolved state or DM, along with any computed expectation values. Users can visualize these results to gain insights into quantum dynamics.

This solver design ensures that both closed and open QSs can be simulated accurately. QuTiP abstracts much of the complexity, allowing users to focus on defining the physics of their problem while relying on the framework for efficient numerical integration.

F.5 Common Errors and How to Resolve Them

When working with QuTiP for QO simulations, users may encounter various errors, ranging from syntax issues to numerical instabilities. Below is a summary of common errors and practical ways to address them:

- **Dimension Mismatch Error:** This occurs when operators, states, or Hs have incompatible dimensions. For example, applying a 2×2 operator to a 3-dimensional state will result in a mismatch error.

  - **Solution:** Verify that all matrices, operators, and states have compatible dimensions. Use `qutip.tensor()` to properly combine systems if needed.

- **TypeError: 'NoneType' Object is Not Callable:** This error often occurs when functions, such as H coefficients, are improperly defined or not passed correctly.

  - **Solution:** Ensure that all time-dependent coefficients are properly defined as Python functions or arrays. Double-check their syntax and signature.

- **Sparse Matrix Warning or Memory Error:** QuTiP uses sparse matrices to handle large systems efficiently. However, for very large systems or dense matrices, users might encounter memory limitations.

  - **Solution:** Reduce the system size if possible, or use sparse matrix representations efficiently. Check the documentation for using `qutip.solver.Options` to fine-tune memory management.

- **Integration Failed (zvode error):** This happens when the numerical solver cannot find a stable solution, often due to stiff equations or large time steps.

  - **Solution:** Use smaller time steps or enable more accurate solver options by modifying the tolerance values via `qutip.solver.Options`. Example:

```
options = Options(atol=1e-8, rtol=1e-6)
```

- **KeyError or AttributeError:** These errors usually indicate a typo in function names, parameter names, or attributes. This can happen, for example, if the user calls an attribute that does not exist in the QuTiP version they are using.

  - **Solution:** Double-check the QuTiP documentation for the correct syntax. If working with time-dependent Hs, ensure proper function naming and parameterization.

- **Convergence Issues:** In some cases, especially with highly dissipative systems, the solver might struggle to converge to a stable solution.

  - **Solution:** Try different solvers (e.g., switching between `sesolve`, `mesolve`, or `mcsolve`) or adjust the system parameters to ensure that the problem is well-defined.

- **Import Errors or Missing Dependencies:** This error occurs when QuTiP or its dependencies are not properly installed.

  - **Solution:** Ensure that QuTiP and all necessary libraries are installed using:

    ```
    pip install qutip
    ```

    Also, ensure that the Python environment is correctly configured.

- **Singularity Error:** This error occurs when the numerical solver encounters a point during integration where the equations become singular (i.e., the system's dynamics lead to undefined or infinite values). It typically arises from improper initial conditions, ill-conditioned matrices, or physical parameters that cause divergence in the system's evolution.

  - **Potential Causes:**
    * The H or CO contain elements that lead to unbounded evolution, such as large energy gaps or unphysical parameter values.
    * A time-dependent H or coefficient function may introduce a discontinuity or diverge at specific times.
    * Initial state vectors may not be properly normalized, which can destabilize the simulation.
    * Numerical stiffness, especially in dissipative systems, can cause singularities if the solver struggles to resolve rapid changes in dynamics.
  - **Solution Strategies:**
    * **Check the H and CO:** Ensure all operators are physically valid and represent realistic QSs. Avoid extreme values that could cause rapid divergence.
    * **Use Regularization Techniques:** If matrices in the system are ill-conditioned, apply small perturbations or add regularization terms

to stabilize the computation. This is particularly useful for systems sensitive to small parameter changes.

* **Adjust Time Steps and Tolerances:** For stiff systems, use smaller time steps or increase the precision of the solver by setting tighter tolerances. For example:

```
options = Options(atol=1e-10, rtol=1e-8)
```

* **Smooth Time-Dependent Functions:** If the H or coefficients are time-dependent, ensure they are continuous and well-behaved throughout the simulation. Sudden jumps in time-dependent functions can introduce singularities.
* **Verify Initial Conditions:** Ensure that the initial state is properly normalized and consistent with the system's dynamics. For example, if simulating an open QS, the DM should be positive semidefinite with a trace of 1.
* **Switch to a Different Solver:** In cases where the default solver struggles, try using a different solver available in QuTiP (e.g., switching from `sesolve` to `mesolve`, or using `Options(method='adams')` to handle stiff systems).

- **Overflow Error in Exponential Function:** This error occurs when the value inside the exponential function becomes too large to be represented within the numerical limits of floating-point precision, resulting in an overflow. In Python, Numerical Python package (NumPy) raises this warning to indicate that the result of the `exp()` function is infinity (`inf`).

  – **Error Message:**

```
<ipython-input-44-41f98cbf7cbf>:155: RuntimeWarning:
overflow encountered in exp
  absorption = np.exp(-alpha * length)
```

  – **Potential Causes:**

  * The product $\alpha \times$ `length` becomes very large, causing the exponential value to exceed the numerical range Python can handle.

  - Incorrect parameter scaling (e.g., extremely large α or `length` values) in the physical model can trigger this issue.
  - Attempting to model extremely high absorption over long distances without normalization.

- **Solution Strategies:**
  - **Scale Input Parameters:** Ensure that the values of α and `length` are within a reasonable range. For example, if α is in the order of 10^{20}, consider adjusting the units or normalizing the parameters.
  - **Use `scipy.special.expit` for Stability:** If the large argument values are unavoidable, try using the `expit()` function from SciPy's special module, which computes a numerically stable sigmoid:

```
from scipy.special import expit
absorption = expit(-alpha * length)
```

  - **Set a Value Cap:** Introduce a threshold to limit the input values passed to `np.exp()`:

```
max_value = 700  # Avoid overflow (logarithmic scale cap)
argument = np.clip(-alpha * length, -max_value, max_value)
absorption = np.exp(argument)
```

  - **Use Logarithmic Representation:** If possible, compute the logarithm of the absorption function to avoid direct exponentiation:

```
log_absorption = -alpha * length
absorption = np.exp(log_absorption)  # Only if needed later
```

  - **Evaluate Physical Validity:** Check if the model parameters (e.g., absorption coefficient) are physically realistic. Large absorption coefficients may indicate an error in the model or parameterization.

F.6 General Approach to Debugging QuTiP and QS

Debugging QS can be challenging due to the complex nature of quantum dynamics. Below is a structured approach to identify, diagnose, and resolve errors systematically.

Step 1: Understand the Error Message Most Python-based solvers, including QuTiP, provide error messages with tracebacks. Carefully read the error message and identify:

- **Type of Error:** Is it a `ValueError`, `TypeError`, `IndexError`, or something else?
- **Location of the Error:** Traceback shows where the error occurred. Review the file name, function, and line number.
- **Common Quantum Errors:** Look for specific issues such as singularities, non-Hermitian operators, or dimensional mismatches.

Step 2: Simplify the Code If the error isn't obvious, simplify the problem by:

- Isolating the part of the code that triggers the error.
- Running minimal test cases to see if the issue persists.
- Commenting out sections of the code to focus on smaller components.

Step 3: Validate Input Parameters and Dimensions Many issues in quantum simulations arise from incorrect inputs:

- Ensure operators (H, CO) are properly defined and have matching dimensions.
- Verify that time-dependent functions are smooth and correctly parameterized.
- For density matrices, confirm they are Hermitian and have trace 1.

Step 4: Use Debugging Tools Python offers several tools to help you step through the code and inspect variables:

- **Built-in Debugger:** Use the `pdb` module to insert breakpoints:

  ```
  import pdb; pdb.set_trace()
  ```

  This allows you to pause execution and inspect variables line-by-line.

- **Interactive Python (IPython) Debugging:** Run your code in an IPython environment using:

  ```
  %debug
  ```

  after an error occurs to enter post-mortem debugging mode.

- **Print Statements:** Sometimes, inserting `print()` statements is the quickest way to understand the state of variables and parameters.

Step 5: Check for Common Pitfalls in Quantum Simulations

- **Singularity Errors:** Review the dynamics for any points where the evolution could diverge (e.g., division by zero).
- **Convergence Issues:** Ensure that time steps are appropriately small, and the solver is configured to handle stiff DEs.
- **Dimensional Mismatches:** Confirm that all operators, states, and matrices have compatible dimensions.

Appendix G

Running Code Locally vs. Google Colab

When simulating quantum optical systems, researchers often have the choice between running their code on a local machine or using cloud-based platforms such as Google Colab. Each approach has its advantages and disadvantages.

Local Machine

Running simulations on a local machine allows for greater control over the environment, as users can install specific software versions, manage dependencies, and tailor the system configuration to their needs. However, this approach can be limited by the available hardware resources, such as Central Processing Unit (CPU), RAM, and storage. For computationally intensive simulations, a local machine may experience performance bottlenecks, potentially leading to longer execution times.

Google Colab

Google Colab, on the other hand, provides a cloud-based environment that is particularly advantageous for running resource-intensive simulations. It offers free access to powerful Graphics Processing Units (GPUs) and Tensor Processing Units (TPUs), enabling faster computations compared to many local machines. Additionally, Google Colab allows for easy sharing of code and collaboration with others, as notebooks can be easily shared and edited online.

Throughout this thesis, all simulations were conducted using both Google Colab and local machine. Sometimes simultaneously to speed run a couple of different

simulations. Using Colab facilitated efficient computations and simplified the sharing of code with collaborators.

Appendix H

How to Reduce the Runtime in Numerical Calculations

In numerical simulations, optimizing runtime is crucial, especially for resource-intensive quantum simulations. The general principle is that the more pre-processing and simplifications you perform on your end, the less work the computer needs to do. This results in both faster calculations and more efficient memory management. Below are several strategies to help reduce runtime, along with an explanation of why these optimizations matter.

Parameter Normalization

One effective strategy is parameter normalization. By scaling all parameters relative to a dominant or characteristic parameter in the system (e.g., Natural linewidth, or the largest energy scale, or a common time constant), the computer can avoid handling excessively large or small floating-point numbers. This not only reduces the required precision but also decreases memory usage and speeds up calculations.

For instance, let's say you have variables that range across several orders of magnitude. If you normalize these variables relative to a dominant one, you bring them into a more manageable range. A normalized parameter often equals 1, which is computationally advantageous. A constant value of 1, stored as an integer, occupies only 32 bits, whereas floating-point numbers with many decimal places require up to 64 bits.

Efficient Memory Allocation

Memory allocation is another key aspect of runtime optimization. When large arrays are required for storing quantum states, operators, or time-evolution data, it helps to:

- Use `numpy.float32` instead of `numpy.float64` if double precision is not necessary.
- Pre-allocate memory whenever possible to avoid dynamic resizing during computations. For example, initializing an array with a known size is more efficient than incrementally expanding it in a loop.
- Exploit sparse matrix representations for large operators, such as Hs. Libraries like `scipy.sparse` allow you to store only the non-zero elements, significantly reducing memory usage and computation time.

Parallel Computing

Using parallel computing can significantly reduce runtime. Python libraries such as `multiprocessing`, `numba`, or `joblib` allow you to distribute the workload across multiple cores of a CPU or even across GPUs. On platforms like Google Colab, you can leverage available GPUs to accelerate your quantum simulations.

Optimizing Code Logic

The structure of your code has a direct impact on runtime. The following practices can help:

- **Avoid Redundant Calculations:** If a value is used multiple times, compute it once and store it in a variable, rather than recomputing it within a loop.
- **Vectorization:** Use vectorized operations with libraries like `numpy` instead of writing explicit loops. Vectorized operations are usually implemented in low-level languages like C, making them much faster than Python loops.
- **Use Symmetries:** Identify and exploit any symmetries in the system to reduce the size of matrices or the number of calculations. For example, if your H is Hermitian, you only need to compute half of its elements.

Using Efficient Algorithms

Different algorithms can have drastically different runtimes for the same problem. For example, using a Runge-Kutta solver with adaptive step sizes can be faster than using a fixed-step integrator for solving DEs in time evolution. In QuTiP, choosing solvers that match the nature of your system (e.g., sparse solvers for large sparse matrices) can optimize performance.

Batching and Caching Intermediate Results

If you are running repeated simulations with only slight changes to parameters, it is helpful to cache intermediate results. This prevents recalculating identical values multiple times. Similarly, batching multiple calculations together can reduce overhead, especially when communicating with external devices or APIs.

Leveraging Colab's Environment

Given that all simulations in this thesis were run on Google Colab, it is important to note that Colab offers several runtime accelerators (e.g., GPUs and TPUs) that can significantly enhance computational performance. To maximize efficiency on Colab:

- Use GPU or TPU runtimes when working with large-scale simulations.
- Store large datasets in Google Drive and access them directly, minimizing the need for frequent uploads and downloads.
- Monitor memory and CPU/GPU usage using Colab's built-in tools to ensure optimal resource utilization.

Appendix I

Using Git for Version Control and Cloning the Repository

All the codes used in this thesis are available on GitHub for reproducibility and further exploration. Follow the steps below to clone the repository and run the code either locally or on Google Colab.

Cloning the Repository

Make sure `git` is installed, then run the following command in your terminal:

```
git clone <repository-URL>
```

Navigate to the project folder:

```
cd your-repository
```

Running the Code Locally or on Google Colab

For local execution, install the dependencies using:

```
# (Optional) Create a virtual environment
python -m venv venv
source venv/bin/activate  # On Linux/macOS
venv\Scripts\activate  # On Windows

pip install -r requirements.txt
```

Then, run the scripts:

```
python your_script.py
```

To use Google Colab: 1. Open a notebook on `https://colab.research.google.com/`. 2. Clone the repository inside Colab:

```
!git clone <repository-URL>
%cd your-repository
!pip install -r requirements.txt
```

Troubleshooting Common Issues

- **Permission Errors:** Ensure the repository is public or you have the right access.
- **Dependency Issues:** Update pip using `pip install --upgrade pip` if package installations fail.
- **Colab Path Issues:** Use `%cd` to ensure the correct working directory.